ECR Microwave Plasma Processing Techniques and Effects of Deposition Parameters on Properties of MOS Systems

by

The-Tu Chau

A thesis

Submitted to the Faculty of Graduate Studies

in partial fulfillment of the requirements for the degree of

Doctor of Philosophy

Department of Electrical and Computer Engineering

University of Manitoba

Winnipeg, Manitoba

ISBN 0-612-13022-3

Canada

Name THE-TU CHAU

Dissertation Abstracts International is arranged by broad, general subject categories. Please select the one subject which most nearly describes the content of your dissertation. Enter the corresponding four-digit code in the spaces provided.

ECR MICROWAVE plasma, MOS system, Silicon dioxide film

SUBJECT TERM

0	7	9	4

SUBJECT CODE

U·M·I

Subject Categories

THE HUMANITIES AND SOCIAL SCIENCES

COMMUNICATIONS AND THE ARTS
Architecture 0729
Art History 0377
Cinema 0900
Dance 0378
Fine Arts 0357
Information Science 0723
Journalism 0391
Library Science 0399
Mass Communications 0708
Music 0413
Speech Communication 0459
Theater 0465

EDUCATION
General 0515
Administration 0514
Adult and Continuing 0516
Agricultural 0517
Art 0273
Bilingual and Multicultural 0282
Business 0688
Community College 0275
Curriculum and Instruction 0727
Early Childhood 0518
Elementary 0524
Finance 0277
Guidance and Counseling 0519
Health 0680
Higher 0745
History of 0520
Home Economics 0278
Industrial 0521
Language and Literature 0279
Mathematics 0280
Music 0522
Philosophy of 0998
Physical 0523
Psychology 0525
Reading 0535
Religious 0527
Sciences 0714
Secondary 0533
Social Sciences 0534
Sociology of 0340
Special 0529
Teacher Training 0530
Technology 0710
Tests and Measurements 0288
Vocational 0747

LANGUAGE, LITERATURE AND LINGUISTICS
Language
- General 0679
- Ancient 0289
- Linguistics 0290
- Modern 0291

Literature
- General 0401
- Classical 0294
- Comparative 0295
- Medieval 0297
- Modern 0298
- African 0316
- American 0591
- Asian 0305
- Canadian (English) 0352
- Canadian (French) 0355
- English 0593
- Germanic 0311
- Latin American 0312
- Middle Eastern 0315
- Romance 0313
- Slavic and East European 0314

PHILOSOPHY, RELIGION AND THEOLOGY
Philosophy 0422
Religion
- General 0318
- Biblical Studies 0321
- Clergy 0319
- History of 0320
- Philosophy of 0322

Theology 0469

SOCIAL SCIENCES
American Studies 0323
Anthropology
- Archaeology 0324
- Cultural 0326
- Physical 0327

Business Administration
- General 0310
- Accounting 0272
- Banking 0770
- Management 0454
- Marketing 0338

Canadian Studies 0385
Economics
- General 0501
- Agricultural 0503
- Commerce-Business 0505
- Finance 0508
- History 0509
- Labor 0510
- Theory 0511

Folklore 0358
Geography 0366
Gerontology 0351
History
- General 0578
- Ancient 0579
- Medieval 0581
- Modern 0582
- Black 0328
- African 0331
- Asia, Australia and Oceania 0332
- Canadian 0334
- European 0335
- Latin American 0336
- Middle Eastern 0333
- United States 0337

History of Science 0585
Law 0398
Political Science
- General 0615
- International Law and Relations 0616
- Public Administration 0617

Recreation 0814
Social Work 0452
Sociology
- General 0626
- Criminology and Penology 0627
- Demography 0938
- Ethnic and Racial Studies 0631
- Individual and Family Studies 0628
- Industrial and Labor Relations 0629
- Public and Social Welfare 0630
- Social Structure and Development 0700
- Theory and Methods 0344

Transportation 0709
Urban and Regional Planning 0999
Women's Studies 0453

THE SCIENCES AND ENGINEERING

BIOLOGICAL SCIENCES
Agriculture
- General 0473
- Agronomy 0285
- Animal Culture and Nutrition 0475
- Animal Pathology 0476
- Food Science and Technology 0359
- Forestry and Wildlife 0478
- Plant Culture 0479
- Plant Pathology 0480
- Plant Physiology 0817
- Range Management 0777
- Wood Technology 0746

Biology
- General 0306
- Anatomy 0287
- Biostatistics 0308
- Botany 0309
- Cell 0379
- Ecology 0329
- Entomology 0353
- Genetics 0369
- Limnology 0793
- Microbiology 0410
- Molecular 0307
- Neuroscience 0317
- Oceanography 0416
- Physiology 0433
- Radiation 0821
- Veterinary Science 0778
- Zoology 0472

Biophysics
- General 0786
- Medical 0760

EARTH SCIENCES
Biogeochemistry 0425
Geochemistry 0996
Geodesy 0370
Geology 0372
Geophysics 0373
Hydrology 0388
Mineralogy 0411
Paleobotany 0345
Paleoecology 0426
Paleontology 0418
Paleozoology 0985
Palynology 0427
Physical Geography 0368
Physical Oceanography 0415

HEALTH AND ENVIRONMENTAL SCIENCES
Environmental Sciences 0768
Health Sciences
- General 0566
- Audiology 0300
- Chemotherapy 0992
- Dentistry 0567
- Education 0350
- Hospital Management 0769
- Human Development 0758
- Immunology 0982
- Medicine and Surgery 0564
- Mental Health 0347
- Nursing 0569
- Nutrition 0570
- Obstetrics and Gynecology 0380
- Occupational Health and Therapy 0354
- Ophthalmology 0381
- Pathology 0571
- Pharmacology 0419
- Pharmacy 0572
- Physical Therapy 0382
- Public Health 0573
- Radiology 0574
- Recreation 0575
- Speech Pathology 0460
- Toxicology 0383

Home Economics 0386

PHYSICAL SCIENCES
Pure Sciences
Chemistry
- General 0485
- Agricultural 0749
- Analytical 0486
- Biochemistry 0487
- Inorganic 0488
- Nuclear 0738
- Organic 0490
- Pharmaceutical 0491
- Physical 0494
- Polymer 0495
- Radiation 0754

Mathematics 0405
Physics
- General 0605
- Acoustics 0986
- Astronomy and Astrophysics 0606
- Atmospheric Science 0608
- Atomic 0748
- Electronics and Electricity 0607
- Elementary Particles and High Energy 0798
- Fluid and Plasma 0759
- Molecular 0609
- Nuclear 0610
- Optics 0752
- Radiation 0756
- Solid State 0611

Statistics 0463

Applied Sciences
Applied Mechanics 0346
Computer Science 0984
Engineering
- General 0537
- Aerospace 0538
- Agricultural 0539
- Automotive 0540
- Biomedical 0541
- Chemical 0542
- Civil 0543
- Electronics and Electrical 0544
- Heat and Thermodynamics 0348
- Hydraulic 0545
- Industrial 0546
- Marine 0547
- Materials Science 0794
- Mechanical 0548
- Metallurgy 0743
- Mining 0551
- Nuclear 0552
- Packaging 0549
- Petroleum 0765
- Sanitary and Municipal 0554
- System Science 0790

Geotechnology 0428
Operations Research 0796
Plastics Technology 0795
Textile Technology 0994

PSYCHOLOGY
General 0621
Behavioral 0384
Clinical 0622
Developmental 0620
Experimental 0623
Industrial 0624
Personality 0625
Physiological 0989
Psychobiology 0349
Psychometrics 0632
Social 0451

ECR MICROWAVE PLASMA PROCESSING TECHNIQUES AND EFFECTS OF DEPOSITION PARAMETERS ON PROPERTIES OF MOS SYSTEMS

BY

THE-TU CHAU

A Thesis submitted to the Faculty of Graduate Studies of the University of Manitoba in partial fulfillment of the requirements of the degree of

DOCTOR OF PHILOSOPHY

I hereby declare that I am the sole author of this thesis.
I authorize the University of Manitoba to lend this thesis to other institutions or individuals for the purpose of scholarly research.

The-Tu Chau

I further authorize the University of Manitoba to reproduce this thesis by photocopying or by other means, in total or in part, at the request of other institution or individuals for the purpose of scholarly research.

The-Tu Chau

Abstract

An electron cyclotron resonance (ECR) microwave plasma processing system consisting of a plasma chamber and a processing chamber as well as a new apparatus called the "species selector and energy controller (SSEC)" is described in detail. Silicon dioxide (SiO_2) films fabricated using this system without and with the SSEC are used for various experiments to demonstrate that the SSEC can effectively suppress the damaging effects resulting from the bombardment on the substrates and the on-growing films by energetic particles and photons produced in the plasma during film deposition, as well as effectively reduce the upstream diffusion of the reactant gas from the processing chamber to the plasma chamber thus suppressing the formation of microdust particles due to the heterogeneous gas phase reaction. The growth for the films fabricated without the SSEC is due mainly to mass-limited reaction and that with the SSEC is due to surface rate-limited reaction. The electronic properties of the SiO_2 films fabricated with the SSEC at temperatures higher than 250 °C approach those of high-quality thermally grown silicon dioxides for a range of film thicknesses from 100 Å to 1000 Å under this investigation.

The current-voltage (I-V) characteristics follow closely the Fowler-Norheim (FN) relation implying that at least in this region the motion of the electrons is controlled by their interaction with the lattice rather than by their interaction with traps in the forbidden gap, and that the injected electrons may travel quite a distance before being effectively trapped. There is no evidence of electron impact ionization taking place prior to dielectric breakdown. After the onset of FN injection, the current density

in the leading filament could reach a value as high as 10 A/cm^2 at the breakdown field, which could therefore cause thermal instability in the filament. Dielectric breakdown may be initiated by thermal destruction and followed by impact ionization leading to a sharp increase in current at the breakdown field.

The effects of microwave plasma radiation on properties of metal oxide silicon (MOS) systems have also been studied. The effects are strongly dependent on the temperature during radiation, indicating that there are two processes taking place during radiation; one is the defect-creation and the other is the defect-annihilation. However, most of the radiation-induced defects and charges can be annealed out by a standard post metallization annealing (PMA) treatment.

Acknowledgments

I would like to express my sincere appreciation to my mentor, Dr. K. C. Kao for his guidance, patience, and support throughout this research work. I am also deeply indebted to my friends and colleagues, in particular S. R. Mejia and W. K. Chan for their technical assistance and valuable discussion. The financial support of the Natural Sciences and Engineering Research Council of Canada for this research is also gratefully acknowledged.

Contents

List of Figures

List of Tables

Table **Page**

1

Introduction

The basic device for very large scale integrated (VLSI) circuits is the metal oxide silicon field effect transistor (MOSFET), and the basic insulator material for this device is the silicon dioxide film. The conventional method for fabricating SiO_2 films is based on thermal oxidation of silicon, which involves a temperature of about 1000 °C. Such high temperature processing gives rise to severe temperature sensitive and diffusion related problems for microelectronic devices, and thus temperature or the process thermal budget is one of the major limiting factors for high density, high performance, and short channel MOS VLSI [1.1]. The process thermal budget is related to the maximum time at a given processing temperature that can be tolerated while retaining adequate control of dopant diffusion, particle contamination, thin film uniformity, and reproducibility for the grown or deposited layers. For the deposition of thin films the thermal budget can be reduced by the use of low temperature plasma processing. Among many techniques so far put forward for the deposition of thin films, the plasma enhanced chemical vapor deposition (PECVD) technique has been considered to be one of the most flexible for depositing or etching dielectric and semiconducting films of various compositions and properties. Because of its flexibility the plasma processing technique opens a new direction in the future for ultra large scale integrated (ULSI) circuit fabrication, for which a cluster of multi-processing chambers is integrated into a closed system [1.2, 1.3], to

minimize foreign particle contamination and to prevent harmful chemical waste from leaking out to the environment.

There are three different types of PECVD, systems available at present, namely, the direct PECVD [1.4], the remote PECVD [1.5], and the downstream PECVD [1.6]. For the direct PECVD the substrates are located in the region where activated species are produced for the reaction at the substrate surfaces to form thin solid films. Because of the direct exposure to the plasma, the ionic and electronic bombardment can be utilized to densify the bulk of the films, which is beneficial for some applications such as the fabrication of hydrogenated amorphous silicon films [1.7,1.8]. However, this technique has some drawbacks such as the micro-dust particles formed due to heterogeneous gas phase reaction, which tends to stick on the growing film surfaces causing an uneven or rough surface profile. Furthermore, the ionic bombardment would damage the substrates and the on-growing films during deposition. Plasma is also a source of energetic photon radiations such as soft-X ray and ultraviolet light. These radiations have been known to be harmful to the properties of electronic devices fabricated using silicon based materials [1.9-1.15]. For the remote PECVD, the substrates are placed close to the plasma region but are not in contact to the plasma itself. In this case an external energy source is used to produce a plasma containing activated species. These activated species are then allowed to react with the reactant gas, which is injected in front of the substrate surface. With this technique, the effects of ionic and electronic bombardment on the substrates and the on-growing films can be greatly reduced but the effects of photon radiation prevail. For the downstream PECVD, the substrates are located far away

from the plasma region where they do not see the plasma; so that, the growing films are not subjected to the bombardment of any energetic particles including photons. However, another drawback is that the activated species may lose a large portion of their energy during transportation to the substrate surface, which may cause a reduction in their reaction rate at the substrate surface. It should be noted that all the above processes are performed in an open channel where the reactant gas such as SiH_4 is free to diffuse upstream toward the plasma region.

The PECVD techniques which have been used in industry employ radio-frequency (rf) radiations for plasma excitation of a gas mixture. Microwave frequency radiations have also been used for plasma excitation in recent years. Microwave plasmas under ECR conditions have been used as ion sources [1.16, 1.17]. Subsequently, these ion sources have been further developed into plasma enhanced or activated chemical vapor deposition [1.4, 1.7] and plasma etching [1.18-1.20] systems based on the interaction of relatively energetic ions and activated species with the substrate surface.

In low temperature deposition of SiO_2 films using ECR microwave plasmas in the past seven years, it has been found that microdust particles are always formed during film deposition although silane is injected at a downstream position. As a result, the deposited films usually yield poor current-voltage (I-V) and capacitance-voltage (C-V) characteristics though some physical properties of the films are similar to those of thermally grown SiO_2 films. Trial and error experimental experiences have led to the conclusion that to deposit good quality thin SiO_2 films, three conditions must be met: i) the system must be able to prevent the back diffusion of

SiH_4 from entering the plasma region in order to reduce the heterogeneous gas phase reaction due to the discharge of SiH_4 to form microdust particles in the plasma chamber; ii) the system must be able to suppress all of the energetic particles from bombarding the substrates and the on-growing films in order to reduce damage on the substrate surfaces and defects in the bulk of the films; and iii) the system must be able to provide sufficient activated species for the chemical reaction taking place at the substrate surface in order to maintain a good reaction rate for film deposition.

In this thesis, new approach to meet these three conditions for the deposition of silicon dioxide films will be described. In chapter 3, It will be shown that with a proper control of the species generated in the plasma such as electrons, ions, and excited atoms, silicon dioxide films with high quality similar to thermally grown dioxide can be fabricated by the ECR microwave plasmas. Chapter 2 presents a brief review of literature related to the fabrication techniques and properties of silicon dioxide films. In chapter 4, the effects of deposition parameters on the properties of SiO_2/Si systems are discussed in some detail. A great deal of work reported in the past few years has dealt with the SiO_2 films with thicknesses of 300-500 Å. Film thicknesses below 500 Å may be used as gate oxide layers for MOS devices, while thicker films with thicknesses 500-1000 Å may be used as isolation layers for multi-level metalization in VLSI. One of the objectives in this investigation is to find out whether the dielectric behavior is film-thickness dependent in the thickness range potentially used for microelectronic applications, and if so, to study the electron-trap interaction through this thickness dependence. The results and discussion about this thickness dependence are given also in chapter 4. Since the

effects of microwave plasma radiation are important because in practice PECVD or etching of films may involve the exposure of devices to plasma even for a short period of time. A study of these effects has been carried out. Chapter 5 deals with this subject. The final conclusions of this research are given in chapter 6.

References for chapter 1

[1.1] R. B. Fair and G.A. Ruggles, "*Thermal Budget Issues for Deep Sub-micron ULSI*," Solid State Technol., **33(5)**, 107(1990).

[1.2] K. Achiwa and K. Shankar, "*Deposition and Cluster Tool Equipment Trends in Japan*," Solid State Technol., **33(7)**, 31(1990).

[1.3] K Shankar, "*Cluster Tools: a $2.2 Billion Market by 1994?*" Solid State Technol., **33(10)**, 43(1990).

[1.4] T. V. Herak, T. T. Chau, D. J. Thomson, S. R. Mejia, D. A. Buchanan, and K. C. Kao, "*Low Temperature Depostion of Silicon Dioxide Films from Electron Cyclotron Resonant Microwave Plasma*," J. Appl. Phys., **65**, 2457(1989).

[1.5] G. G. Foutain, R. A. Rudder, S. V. Hattangady, R. J. Markunas, and P. S. Lindorme, "*Low Interface State Density SiO_2 Deposited at 300 °C by Remote Plasma Enhanced Chemical Vapor Deposition on Reconstructed Si Surface,*" J. Appl. Phys., **63**, 4744(1988).

[1.6] B. Robinson, T. N. Nguyen, and M. Copel, in "*Deposition and Gowth Limits for Microelectronics*", edited by G. W. Rubloff, American Insitute of Physics, serries 4, Anaheim, CA. 1987, pp. 112-123.

[1.7] T. V. Herak, T. T. Chau, S.R. Mejia, P. K. Shufflebotham, J. J. Schellenberg, H. C. Card, K. C. Kao, and R. D. McLeod, "*Effects of Substrate Bias on Structure and Properties of a-Si:H Films*

Deposited by ECR Microwave Plasma," J. Non. Cryst. Solids, **77&78**, 227(1987).

[1.8] B. Drevillon, J. Huc, and N. Boussarssar, "*Ion Bombardment Effect on the Growth of a-Si:H Films Deposited from a Pure Silane Plasma*," J. Non. Cryst. Solids, **59&60**, 735(1983).

[1.9] H. P. W. Hey, B. G. Sluijk, anf D. G. Hemmes, "*Ion Bombardment: A Determining Factor in Plasma CVD*," Solid State Technol., **33**(4), 139(1990).

[1.10] L. M. Ephrath and D. J. DiMaria, "*Review on RIE Induced Radiation Damage in Silicon Dioxide*," Solid State Technol., **24**(4), 182(1981).

[1.11] K. H. Ryden, H. Norstrom, C. Nender, and S. Berg, "*Oxide Breakdown due to Charge Accumulation During Plasma Etching*," J. Electrochem. Soc., **134**, 31131987).

[1.12] J. Bos and M. Hendriks, " *Plasma Induced Oxide Fixed Charged*," J. Appl. Phys., **66**, 1244(1989),

[1.13] J. Kassabov, E. Atanassova, D. Dimittrov, and E. Goranova, "*Electrical Properties of Si-SiO_2 Structures Treated in Helium Plasma*," Microelec. J., **18**, 5(1987)

[1.14] N. B. Zhitenev, "*Chemical Potential Shift in Si(100) MOS-Structure Induced by Submillimeter Radiation*," Solid State Comm., **71**, 351(1989).

[1.15] S. Samukawa, "*Damage Caused by Stored Charge During ECR Plasma Etching*," Jpn. J. Appl. Phys., **29**, 980(1990).

[1.16] N. Sakudo, K. Tokiguchi, H. Koike, and I. Kanomata, "*Microwave Ion Source*," Rev. Sci. Instrum., **48**, pp. 762(1977).

[1.17] Y. Okamoto and H. Tamagawa, "*Production of Large Area High Current Ion Beams*," Rev. Sci. Instrum., **43**, 1193(1972).

[1.18] K. Suzuki, S. Okudaira, S. Nishimatsu, K. Usami, and I. Kanomata, "*Microwave Plasma Etching of Si with CF_4 and SF_6 Gas*," J. Electrochem. Soc., **129**, 2764(1982).

[1.19] S. Matsuo and M. Kiuchi, "*Low Temperature Chemical Vapor Deposition Method Utilizing an Electron Cyclotron Resonance Plasma*," Jpn.J. of Appl. Phys., **21**, L4(1982).

[1.20] S. R. Mejia, T. T. Chau, R. D. McLeod, H. C. Card, and K. C. Kao, "*ECR Microwave Plasma Etching*," Can. J. Phys., **65**, 856(1987).

2

Review of Literature Related to Fabrication Techniques and Properties of Silicon Dioxide Films

In general, two common techniques for the synthesis of silicon dioxide (SiO_2) films in the microelectronic industry are the thermal oxidation and the chemical vapor deposition (CVD). The thermal oxidation process is well established, but under certain conditions it is limited by the process thermal budget. The CVD processes, especially the plasma enhanced CVD (PECVD) processes, provide a much lower process thermal budget. However, the PECVD processes are still not fully developed and understood. The following is a brief review of the PECVD processes presently available and the properties of SiO_2 and SiO_2-Si systems.

2.1 Plasma enhanced chemical vapor deposition

The film deposition processes involve three major steps: (i) the creation of a flux of condensable species (neutral or excited atoms or molecules and ions), (ii) the transportation of these species to the substrate, and (iii) the growth of a film on the substrate surface. The most important step of these is the creation of the condensable species. In the plasma enhanced chemical vapor deposition (PECVD), the condensable species are created from a plasma that is formed due to electrical discharge of a gas or a gas mixture at low gas pressures. In principle, the PECVD techniques can be classified into two main categories: (1) the direct PECVD in which

the reactant gases are subjected to direct current (dc), radio frequency (rf) or microwave plasma excitation, and the substrates are directly exposed to the plasma [2.1, 2.2], and (2) the indirect PECVD in which plasma excitation is selective, and the substrates are positioned outside the plasma region [2.3-2.4]. In the following sections, the fabrication of SiO_2 films using these techniques will be described.

2.1.1. The direct PECVD techniques

In the direct PECVD, the gases (SiH_4 and N_2O or O_2) are mixed in a vacuum chamber and the plasma is formed by electric discharge of this gas mixture using dc, rf, or microwave excitation. The chemical reaction in the direct PECVD is often expressed as [2.5]:

$$[A(gas) + B(gas)]^* \xrightarrow[\text{Plasma}]{\text{Sub. Temp.}} C(solid) + D(gas) \qquad (2.1)$$

where A and B are the gas reactants, the star (*) indicates the gas mixture of A and B excited by electric discharge; C is the deposited solid film; and D is the gas phase byproduct. The location of the substrates is normally close to an electrode, and the substrate sometimes functions itself as an electrode in the case of dc plasma or direct capacitive coupled rf plasma. For the inductive coupled rf plasma or microwave plasma, a substrate holder is normally used to hold the substrates, which is then placed inside or behind the plasma volume. The dc, rf, and microwave plasma processing systems used for the direct PECVD are now briefly described as follows.

A. The direct current (dc) plasma system

When a dc potential (>1 KV) is applied between two electrodes in a

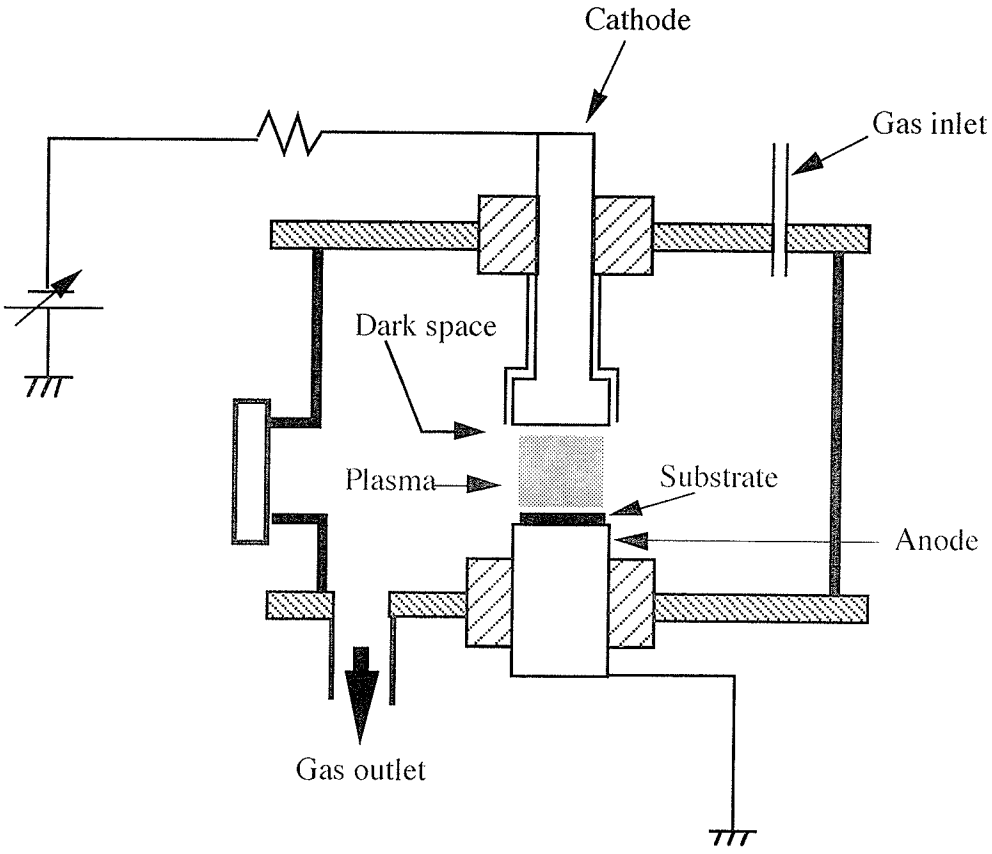

Figure 2.1. Schematic diagram of a dc plasma CVD system (after Suzuki et al [2.7]).

gas or a gas mixture at low pressures, most of the space between the two electrodes is filled with a bright glow known as the glow discharge. Adjacent to the cathode is a comparatively dark sheath known as the dark space. There is a similar sheath at the anode, but it is too thin to be clearly seen [2.6]. A typical dc PECVD system is schematically shown in Fig. 2.1 [2.7]. The separation between the anode and the cathode is about 3 cm. The gases are fed through the gas inlet on the top of the plasma chamber on one side, and the discharge gases are pumped out of the chamber through the gas outlet at the bottom of the chamber in the opposite side. Typical operating pressures are between 2 to 200 torr [2.7]. The dc plasma system can be used for deposition and etching of films. However, the dc plasma

system is not an ideal system for PECVD of SiO_2 films because of the continuous bombardment on the substrates and the on-growing films by the high energy particles under a dc field, which would cause a serious damage on the SiO_2 films and the SiO_2-Si interfaces.

B. The radio frequency (rf) plasma system

A plasma can be excited by a radio frequency power source. If the rf power input to a gas or a gas mixture is carried out by a coil, the method is often referred to as the "inductive coupled" [2.8]. If the rf power input to a gas or a gas mixture is carried out by the electrically biased electrodes, the method is referred to as the "direct capacitive coupled." The direct capacitive coupled (DCC) rf plasma has a high degree of flexibility for controlling the film deposition over a large area. A typical radial flow DCC rf plasma system is shown in Fig. 2.2 [2.9]. The system consists of two parallel circular plate electrodes. The upper electrode is connected to a rf generator through an impedance matching network. The radio frequency used is 13.56 MHz (normally allowed for industrial applications). The wafers sit on a lower electrode surface which is electrically grounded. The gas inlet is at the center of the lower electrode, and the gas or gas mixture flows outward in radial direction. A magnetic drive assembly permits rotation of the lower electrode, thus randomizing the substrate position and optimizing the deposition uniformity.

In the plasma chamber electrons, oscillating in the high frequency field, gain sufficient energy from the field to fragment, excite, and ionize the gas molecules. The condensable species created in the plasma will then diffuse to the electrode to contribute to the growth of the film. The DCC

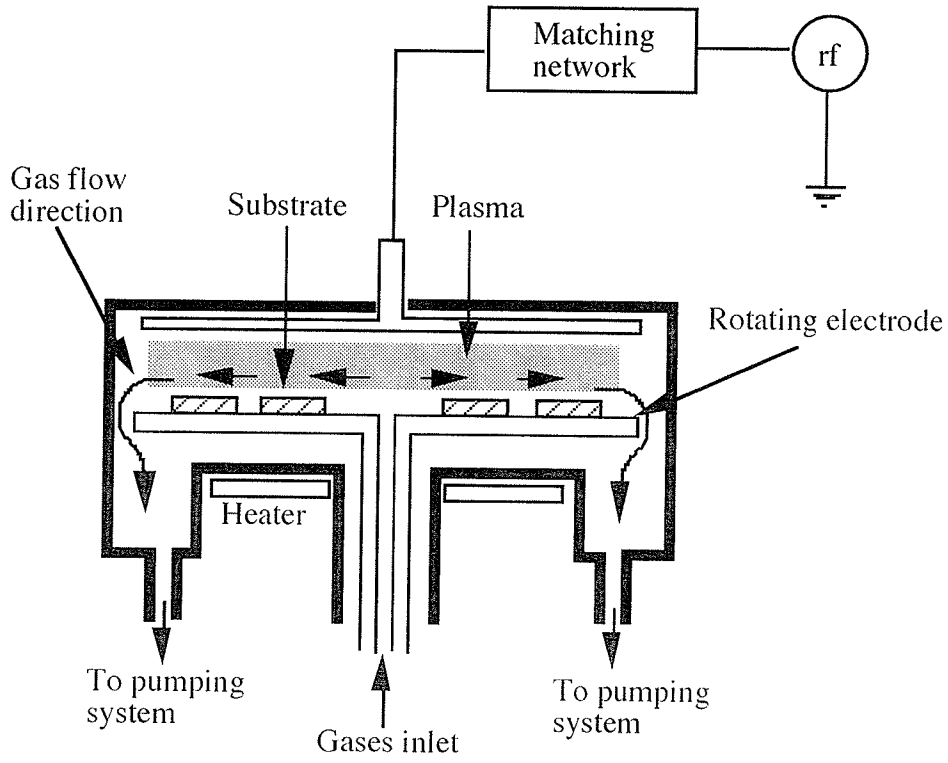

Figure 2.2. A typical direct capacitive coupled rf plasma system (after Rosler [2.9]).

rf plasma is generally produced at a pressure of about 1 torr and input power of 20 to 1000 watts. The concentrations of ions and electrons depend on the pressure and are of the order of about 10^{10} to 10^{11} cm^{-3} at 1 torr. Since the radicals are formed in the bulk of the plasma, the chemical processes are more prone to the occurrence of gas phase reactions involving these radicals (homogeneous reaction) [2.10]. The gas phase reactions would then produce dust particles to contaminate the on-growing films. The probability of the homogeneous reactions can be reduced by decreasing the electrode spacing and the radical density. However, the electrode spacing can not be arbitrarily reduced. It is always larger than the extent of the dark space at the operating pressure and is commonly about a few centimeters [2.10]. On the other hand, reducing the ion density by decreasing the gas pressure is not favored because the ion density

reduces rapidly as the pressure is decreased [2.11].

The direct PECVD of SiO_2 films using DCC rf plasmas can yield an extremely high deposition rate (>1000 Å/min) but the films tend to contain impurities, are porous, unstable, and have very poor electrical properties [2.12]. Furthermore, for the direct PECVD the problem of ion bombardment and other effects due to high energetic plasma environment cannot be avoided.

To reduce the homogeneous reactions in a DCC rf plasma, Batey et al [2.12] have suggested diluting the gas mixture with He gas. The SiO_2 films deposited using He as the diluting gas exhibit good electrical properties (breakdown strength of about 10 MV/cm and the interface trap density of the order of 2×10^{10} eV^{-1} cm^{-2}). It is believed that the He atom has a large cross section for excitation by energetic electrons, which makes the plasma relatively easy to excite and helps to keep the plasma less energetic. Also, because the gases are diluted, the fragmentation of the reactants is prevented, thereby avoiding the homogeneous chemical reaction to form dust particles. However, this technique requires a very large gas flow throughput that may limit the flexibility of changing the process variables (i.e., pressure and gas flow). Furthermore, the discharged gas mixture includes the SiH_4 gas; thus, the probability for the gas phase reaction may be reduced but not completely removed. In addition, the substrates are emerged in the plasma volume so that ion bombardment on the substrate surface and the on-growing films is still a concern for the deposition of high quality thin films.

What has discussed so far is related mainly to the low density rf

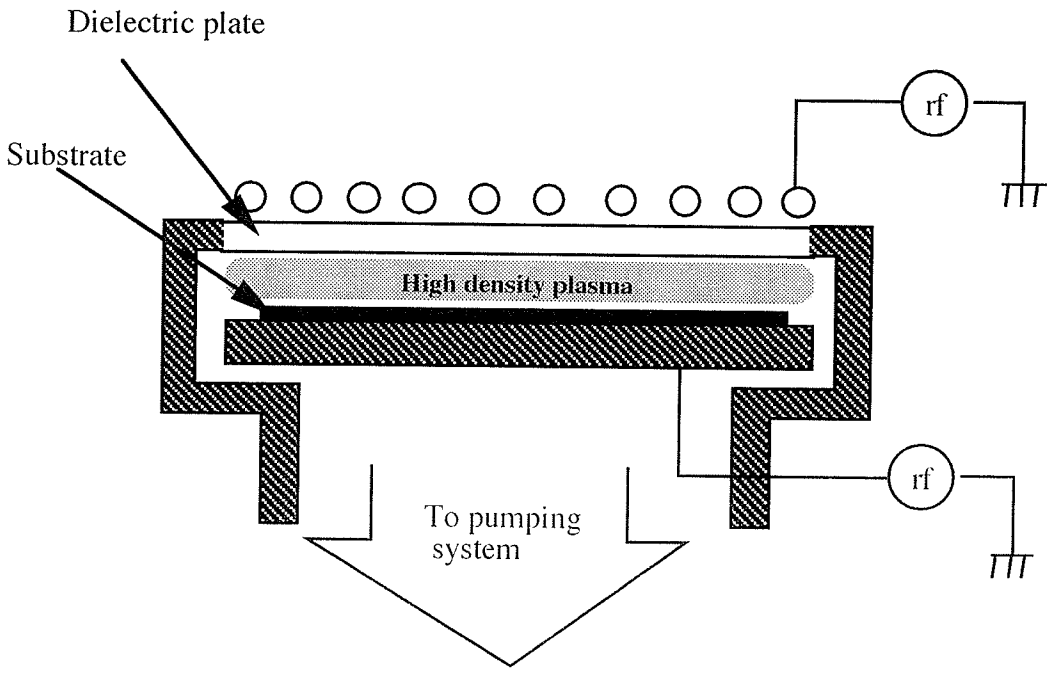

Figure 2.3. Schematic diagram of high density rf TCP system (after Singer [2.11]).

plasma. A variety of promising new rf plasma sources that are able to deliver high density plasmas at low pressures are beginning to emerge. These are the inductive coupling plasmas (ICP) and the transmission coupled plasmas (TCP). The former is used for the indirect PECVD and will be discussed later in the next section. The latter has been developed for fine pattern etching at low pressures. Typical rf TCP system is shown in Fig. 2.3. The rf power is coupled to the plasma via a spiral antenna through a dielectric plate. The plasma volume is directly beneath the dielectric plate and is not dependent on the distance between the substrate holder and the dielectric plate. The TCP can be produced at a pressure of about 300 mtorr and has an ion density of the order of 10^{12} cm^{-3}. The substrates sit on the substrate holder and face the plasma volume, which is similar to the DCC rf plasma system. This new technology is still under development. However, the possibility of homogeneous gas phase reaction

and radiation damage to the SiO_2 films or the SiO_2-Si systems are not ruled out if this system is used for the direct PECVD of SiO_2 films.

C. The ECR microwave plasma system

Microwave power can be supplied to a gas or a gas mixture simply by placing a gas discharge tube inside a wave guide or a cavity at the location of high electric fields. However, this technique has several disadvantages such as the sputtering of the discharge tube and the surrounding structures [2.13-2.14]. Subsequently, an external magnetic field is used for confining the plasma close to the center of the tube, thus preventing such a sputtering effects [2.15 - 2.18]. When a microwave plasma is subjected to an external magnetic field perpendicular to the electric field vector of the electromagnetic excitation, electrons and ions are forced to assume circular or helical paths around the lines of force of the magnetic field. Hence, the electrons and ions are confined in the direction perpendicular to the magnetic field vectors. The angular frequency of the electron rotation increases with increasing magnetic field. When this frequency reaches the angular frequency of the microwave excitation, the electron cyclotron resonance (ECR) condition sets in. The schematic diagram of the ECR microwave plasma system is shown in Fig. 2.4 [2.19]. Microwave power (usually with the frequency 2.45 GHz) is introduced into the plasma chamber through a rectangular wave guide and a window made of fused quartz plate. The plasma chamber is typically 20 cm in diameter and 20 cm in height and operates as a microwave cavity resonator (TE_{113}). Magnetic field coils are arranged around the periphery of the chamber for the ECR microwave plasma excitation. Reactant gases are introduced through two respective inlets into the plasma chamber and the processing

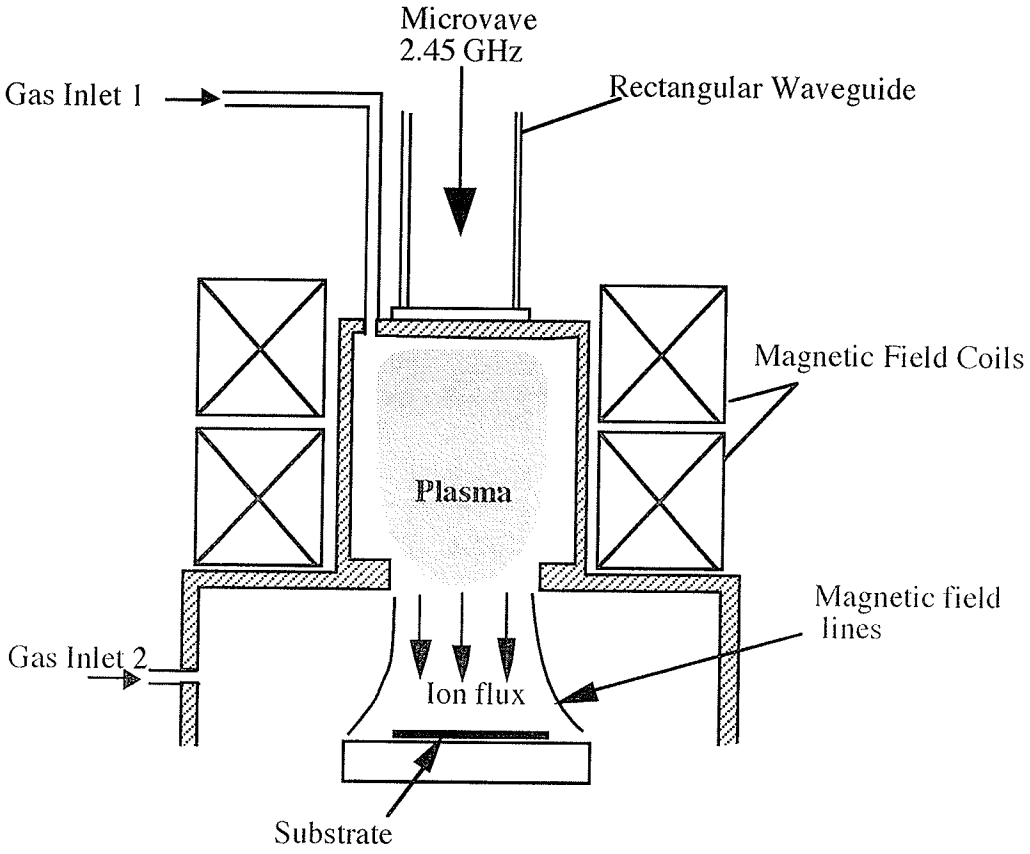

Figure 2.4. Shematic diagram of the ECR microwave plasma system (after Machida et al [2.19]).

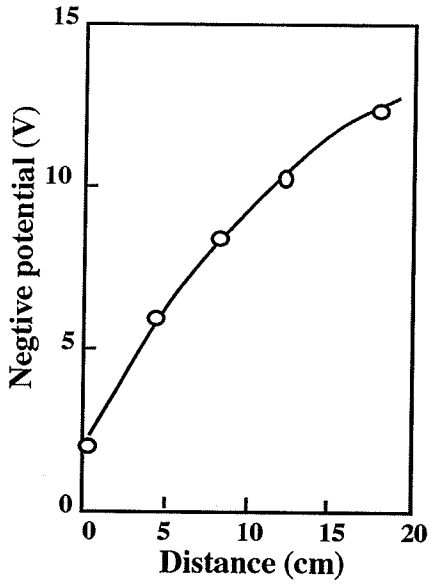

Figure 2.5. The floating potential as a function of the distance from the substrate holder to the ion attraction window at gas pressure 2x 10^{-4} torr and at microwave power 100 watt (after Machida et al [2.19]).

chamber. The plasma chamber and the magnet are water-cooled. A divergent magnetic field is used to guide the ions to move to the substrate. The floating potential measured at the substrate holder depends on the distance from it to the plasma extraction window. Typical results for this dependence are shown in Fig. 2.5. The energy of the ion bombardment is found as high as about 20 eV [2.19].

The ECR microwave plasma systems have been used for the deposition of SiO_2 films. The best quality SiO_2 films deposited by direct ECR microwave plasmas have a breakdown strength approaching 10 MV/cm [2.20], but the oxide trapped charge and the interface trap density are larger than those of the best thermally grown oxide films. The high interface trap density may be due to the damage at the interface by the ion bombardment. Many reports have dealt with the damage of the MOS devices by the ECR microwave plasmas during etching [2.21-2.22]. However, photon radiation from the plasma may be the main cause for the defects created in the SiO_2 films deposited by direct ECR microwave plasmas.

2.1.2. The indirect PECVD techniques

The objective of the after glow PECVD (indirect PECVD) is to reduce the damage due to radiation from the plasma and to reduce the dust particle formations due to SiH_4 gas discharge. In general, the gas containing oxygen such as N_2O or O_2 or CO_2 is electrically discharged to produce excited oxygen species. These species are then transported from the discharged region to the substrate location. Then the excited oxygen species will be mixed with the gas containing Si (SiH_4) for the chemical

reaction on the surface of the substrate. The chemical reaction pathway in the remote PECVD is often written in a general form as follows:

$$[A(gas)]^* + B(gas) \xrightarrow{\text{Sub. Temp.}} C(solid) + D(gas) \qquad (2.2)$$

The transportation of activated oxygen species to the reaction zone is usually carried out by an inert gas such as Ar or He with a high flow rate. The indirect PECVD can be grouped into the remote PECVD and the down stream PECVD depending on their configuration. These systems are now briefly described.

A. The remote rf PECVD system

Figure 2.6 shows the remote rf PECVD system using an inductive coupled plasma source. Gases delivered into the top of the reactor are excited in the glass tube, and then transported out of the discharge region into the main chamber. The length of the excitation region is about 10 cm, and the distance between the plasma and the substrate is also about 10 cm.

A great deal of works has been published about the structure of the SiO_2 films and the formation of the SiO_2 films using this system [2.5, 2.23, 2.28, 2.43]. For the deposition of good quality SiO_2 films, the helium gas has been used as a carrier gas to transport the excited oxygen to the processing chamber. A typical flow rate is 100 sccm for gases delivered through the top gas inlet port. The nominal pressure in the chamber is 0.3 torr. Under these conditions the mean free path for two body gas phase collisions is less than a millimeter. The use of a high gas flow rate and a high gas pressure is for the prevention of SiH_4 to diffuse into the plasma chamber, and, like the direct PECVD, the He gas also acts as the diluted gas

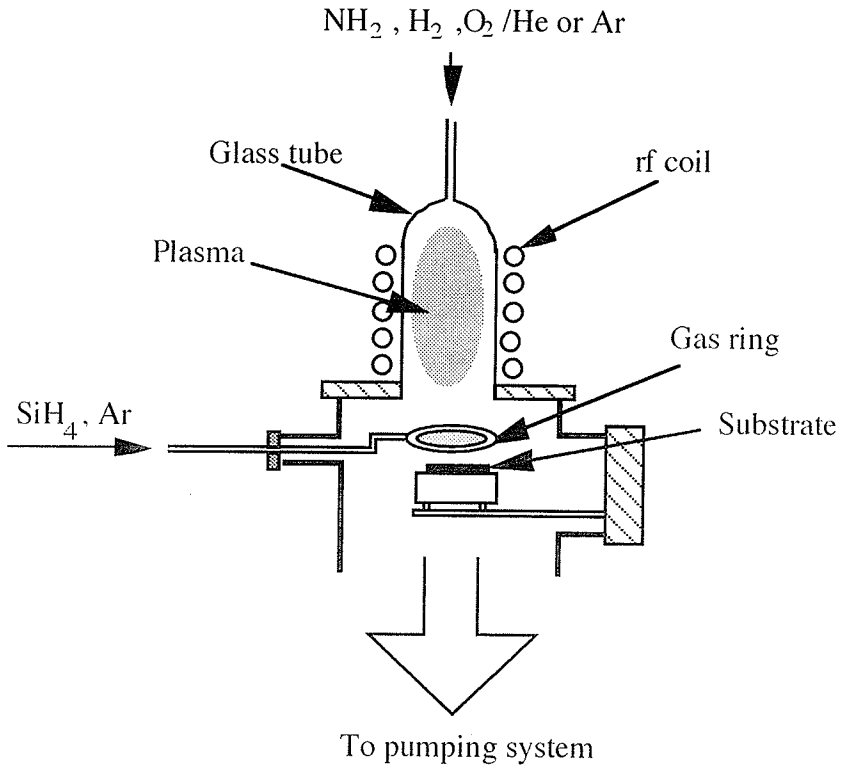

Figure 2.6. Schematic Diagram of the remote rf PECVD plasma system, (after Lucovsky et al [2.23]).

to prevent the homogenous gas phase reaction. Even though the substrate is located about 10 cm away from the plasma source, it can see the plasma volume, so the problem of photon impinging on the substrate surface and the on-growing films may still be a big concern.

B. The downstream PECVD system

In the downstream PECVD system, the substrates are located as far as 60-70 cm away from the plasma discharge volume [2.24,-2.26]. A typical downstream PECVD system is shown in Fig. 2.7 employing a microwave discharge tube. The mass flow controllers are used to deliver gas to a 5 cm diameter quartz tube via gas inlet #1. A typical gas flow rate is 760 sccm. In this arrangement, the plasma is confined in the 5 cm diameter quartz tube. Active species then transport down the long quartz tube of 7.5 cm

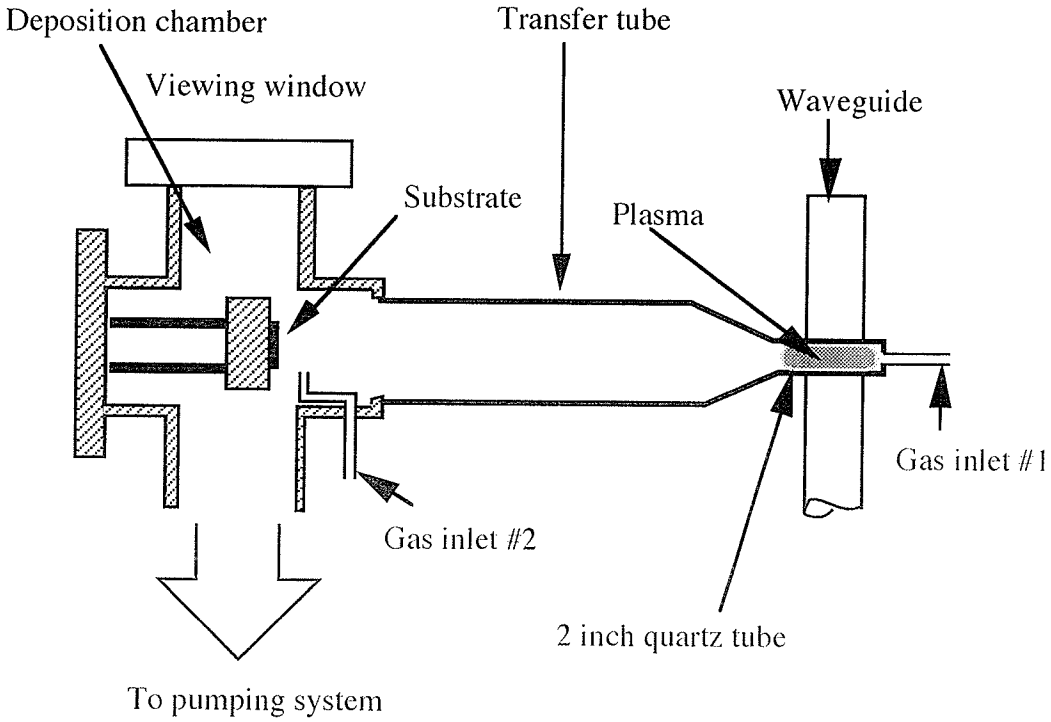

Figure 2.7. A typical downstream PECVD system (after Doziba et al [2.24]).

in diameter and 60 cm in length, to the deposition chamber. The substrates are mounted vertically onto a stainless steel heating stage. SiH_4 (10 % dilution in He) at a flow rate of 50 sccm is admitted into the chamber in front of the substrates via gas inlet #2 for chemical reaction with the incoming active species from the transfer tube. The downstream plasma system has been used successfully for the deposition of SiN_x [2.24] and SiO_2 films [2.24-2.26]. The electrical quality of SiO_2 films is close to that of the high quality thermally grown oxide films [2.3]. One of the disadvantages of the downstream PECVD is that it needs a very high gas flow rate in order to transport the active species to the deposition chamber. This may then limit the possibility for the system to be scaled up because the uniformity of the films may become a big concern.

2.2. Properties of silicon dioxide films

The major properties of SiO_2 films for microelectronic application are their physical and electronic properties. The former deal mainly with the structure, the composition (stoichiometry) and the density of the films, while the latter deal mainly with the charges and defects in the bulk of the film and at the SiO_2-Si interface.

2.2.1. Physical properties

The common techniques for the physical characterization of SiO_2 films are the infrared absorption (IR) spectroscopy and the ellipsometry. Both techniques are non-destructive, easy to operate, and fast to obtain the information. In the following, the use of infrared absorption spectroscopy and ellipsometry to characterize the SiO_2 films will be discussed.

A. The infrared (IR) absorption spectroscopy

Silicon dioxide, whose common name is silica, exists in many allotropic forms. Most of them are found in nature in abundant quantities, and some are made under certain laboratory conditions. The well know silica is quartz, tridymite, cristobalite, and amorphous vitreous silica. All these forms are built from the same fundamental structural unit, the SiO_4 tetrahedron. In other words, each silicon atom is surrounded by four oxygen atoms in the tetrahedral structure as shown in Fig. 2.8. Each oxygen atom is bonded to only two silicon atoms forming a Si-O-Si angle, denoted by θ. This angle varies from one allotrope to another [2.27]. The SiO_2 films used as insulation layers in the MOS devices are synthetic either by thermal oxidation or by chemical vapor deposition processes. The structure of these films are generally of amorphous vitreous silica and vary from stoichiometry (SiO_2) to sub-oxide (SiO_x). In either case, the

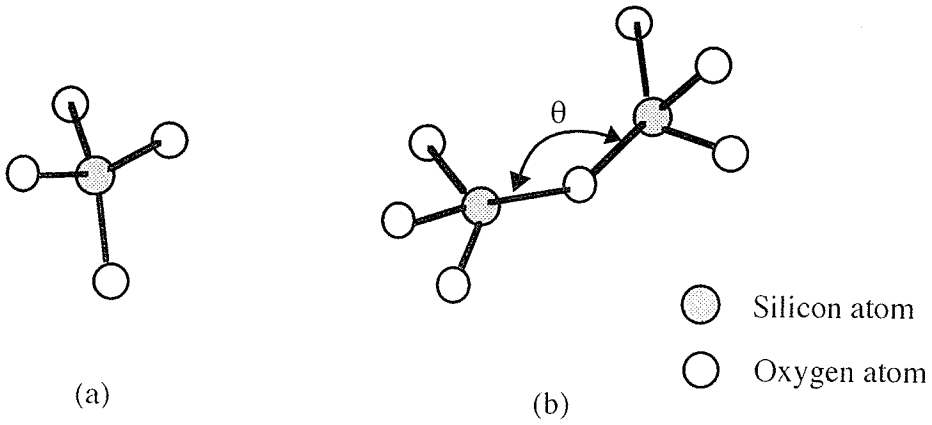

Figure 2.8. The basic SiO_2 units: (a) SiO_4 tetrahedral unit, (b) Adjacent units sharing a corner oxygen atom.

covalency is still preserved. The angle θ is dependent on the film growth process and the deposition parameters. For example, the PECVD films deposited at substrate temperatures ranging from 200°C to 350°C have θ varying between 140° and 144°, and the thermally oxide films grown at temperatures between 800 °C and 1150 °C have θ varying from 147° to 150° [2.28]. For stoichiometric SiO_2 films, the angle θ is related to the frequency of the Si-O-Si stretching absorption peak ν_m of the infrared absorption spectrum following the relation [2.29, 2.43]:

$$\nu_m = \sqrt{\frac{2(\gamma \sin^2 \frac{\theta}{2}) + \beta(\cos^2 \frac{\theta}{2})}{m_o}} \qquad (2.3)$$

Where γ and β are the central and non central force constants, respectively, and m_o is the mass of the oxygen atom. Thus a reduction in θ would cause a decrease in ν_m. The change in ν_m towards a lower value is directly related to an increase in the film density [2.31]. In other words, the reduction in the bond angle causes the film density to increase. However, for the sub-oxide (SiO_x) films, other factors may also contribute to the

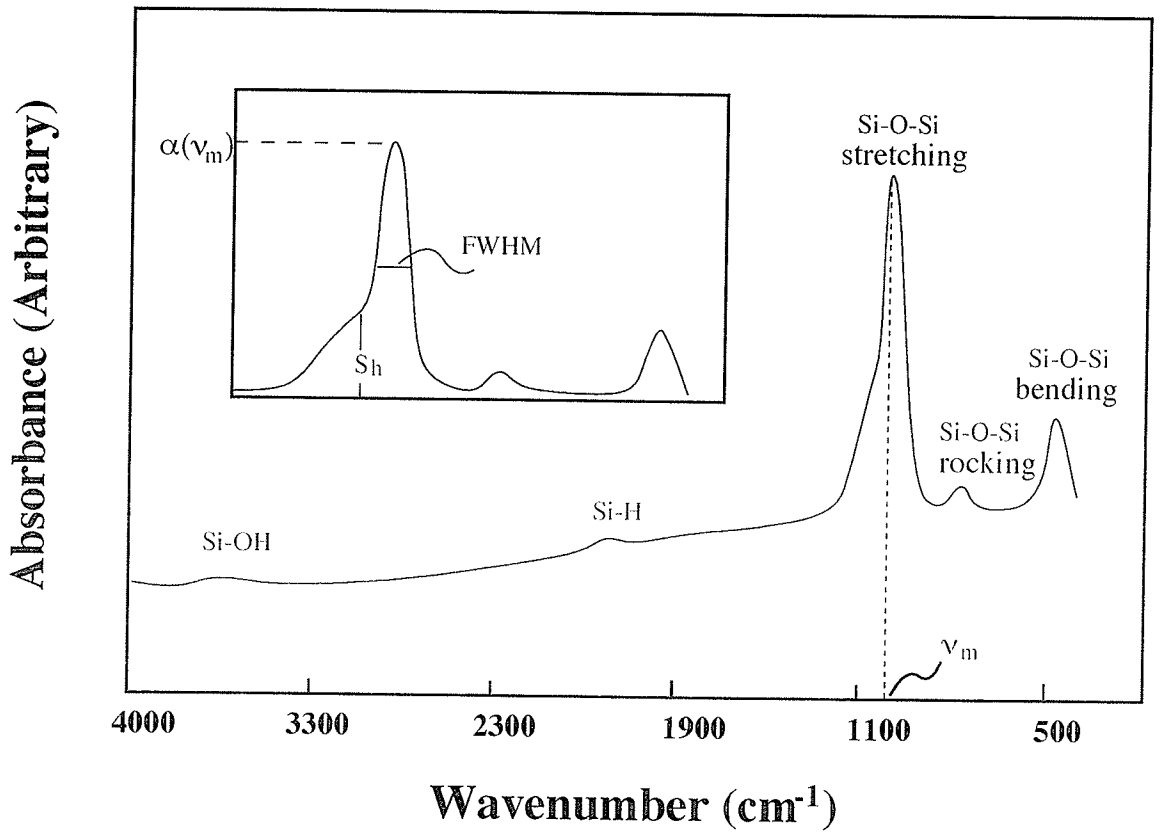

Figure 2.9. A typical infrared absorption spectrum of the silicon sub-oxide.

shift of ν_m towards a lower value. Thus, it is necessary to investigate other properties that appear in the IR absorption spectrum. Three principal Si-O-Si absorption modes in the infrared region are the stretching, the rocking, and the bending. These modes are assigned as follows: the stretching at 1080 cm^{-1}, the rocking mode at 805 cm^{-1}, and the bending mode at 465 cm^{-1} [2.30]. A typical IR spectrum of SiO_x is shown in Fig. 2.9. This spectrum shows the Si-H and Si-OH absorption peaks that could appear in the CVD SiO_x films. The dominant features in IR absorption spectrum of the SiO_2 are associated with the stretching motion of the oxygen atom. This vibration has been described as a rigid sub-lattice mode in which the oxygen and silicon atoms move in opposite directions [2.31]. This means that all the oxygen atoms around a

given silicon atom of the basic $SiO_{4/2}$ building block move with the opposite phase. There are three ways in which the IR spectrum can be used for the evaluation of the SiO_2 films, and they are [2.32].

1) The full-width at the half maximum (FWHM), the peak frequency (ν_m), and the ratio (R_{IR}) of the shoulder height (S_h) to the maximum absorption of the Si-O-Si stretching band, $\alpha(\nu_m)$, near 1080 cm^{-1}, are strongly influenced by the bond characteristics such as the stoichiometry, the density, and the porosity of the films.

2) The intensity of the absorption band near 3650 cm^{-1} (2.74 μm) and 3400 cm^{-1} (2.94 μm) due to hydrogen bonded hydroxyl groups and absorbed water are related to the porosity of the oxide.

3) The impurities other than hydroxyl groups or water can be detected by their characteristic absorption bands.

The relationship between the absorption band and the number of bonds can be estimated by [2.33]:

$$NB=K'\int \frac{\alpha(\nu)}{\nu}\, d\nu \tag{2.4}$$

$$NB=K\int \alpha(\nu)\, d\nu \tag{2.5}$$

where NB is the number of bonds per cm^3, ν is the frequency, K is the constant related to the oscillated strength, and $\alpha(\nu)$ is the absorption coefficient which is given by

$$\alpha(\nu)=\frac{A}{d} \tag{2.6}$$

where A and d are the absorbance and the film thickness, respectively. In practice, the total absorbance can be written as:

$$\int \alpha(\nu)\, d\nu = \alpha(\nu_m).(\mathrm{FWHM}) \tag{2.7}$$

where $\alpha(\nu_m)$ is the maximum absorption coefficient at ν_m. The relationship between ν_m and the oxygen concentration in the film has been proven theoretically [2.34] and confirmed experimentally [2.31, 2.34]. It has been shown that ν_m scales monotonically with the oxygen concentration with the value of 1075 cm^{-1} for stoichiometric SiO_2 to the value of 940 cm^{-1} for oxygen doped amorphous silicon films by simulation [2.34]. A unit of Si-O-Si, shown in Fig. 2.10, is used for this calculation. This unit consists of six atoms X (X could be Si or oxygen) around the two Si atoms. If X is an oxygen atom, ν_m will shift from 940 cm^{-1} to 1080 cm^{-1}, and thus ν_m increases proportionally with increasing number of the neighboring oxygen atoms. This assumption is based on the fact that the frequency for the occurrence of the absorption peak for an isolated Si-O-Si bond in ion implanted Si is at 940 cm^{-1}, and that for a Si-O-Si bond in SiO_2 is at 1080 cm^{-1}. The whole spectrum is then a sum of seven spectra from seven clusters with different numbers of neighboring oxygen atoms. Hence, in a random distribution of Si-O-Si bonds, the probability for the presence of Si-Si and Si-O-Si bonds can be calculated by.

$$P(\mathrm{Si}) = P(\mathrm{Si\text{-}Si}) = \frac{2 - 3x}{2(1 - x)} \tag{2.8}$$

$$P(\mathrm{O}) = P(\mathrm{Si\text{-}O\text{-}Si}) = \frac{2x}{2(1 - x)} \tag{2.9}$$

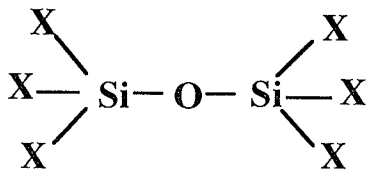

Figure 2.10. A unit Si-O-Si used by Morimoto et al [2.34] for the calculation of the Si-O bonds in a sub-oxide system.

where x is the oxygen content . Morimoto et al [2.34] have calculated the values of ν_m from equations (2.8) and (2.9) as a function of the oxygen content and their results are shown in Fig. 2.11. The solid curve represents the theoretical results and the points are the experimental results from Chao et al [2.35]. Thus, the shift in ν_m towards the lower wave number alone does not indicate whether the film is stoichiometric and high density or silicon sub-oxide. A combination of ν_m, FWHM, and R_{IR} must be considered before any conclusions about the properties of the SiO_2 film can be drawn. The FWHM indicates the sharpness of the stretching absorption peaks. The FWHM is strongly influenced by the bond strain, stoichiometry, and porosity of the films as well as the presence of impurities in the films [2.30, 2.32]. However, the FWHM is not influenced by the film density in the stoichiometric SiO_2 films [2.32] as in the case of the stretching peak frequency. The FWHM can be as low as 60 cm^{-1} for the stoichiometric thermally grown oxide or more than 100 cm^{-1} for the chemical vapor deposition SiO_x films. If the film thicknesses are greater than 100 Å, the FWHM will not depend on the film thicknesses. However, the FWHM is influenced by the film thicknesses under 100 Å [2.36]; the thinner the film the larger is the FWHM. This may be due to the presence of a silicon-rich transition layer at the SiO_2-Si interface. In the evaluation of the SiO_2 films by the IR spectroscopy, the film thicknesses should be greater than 100 Å in order to reduce the error due to the influence of

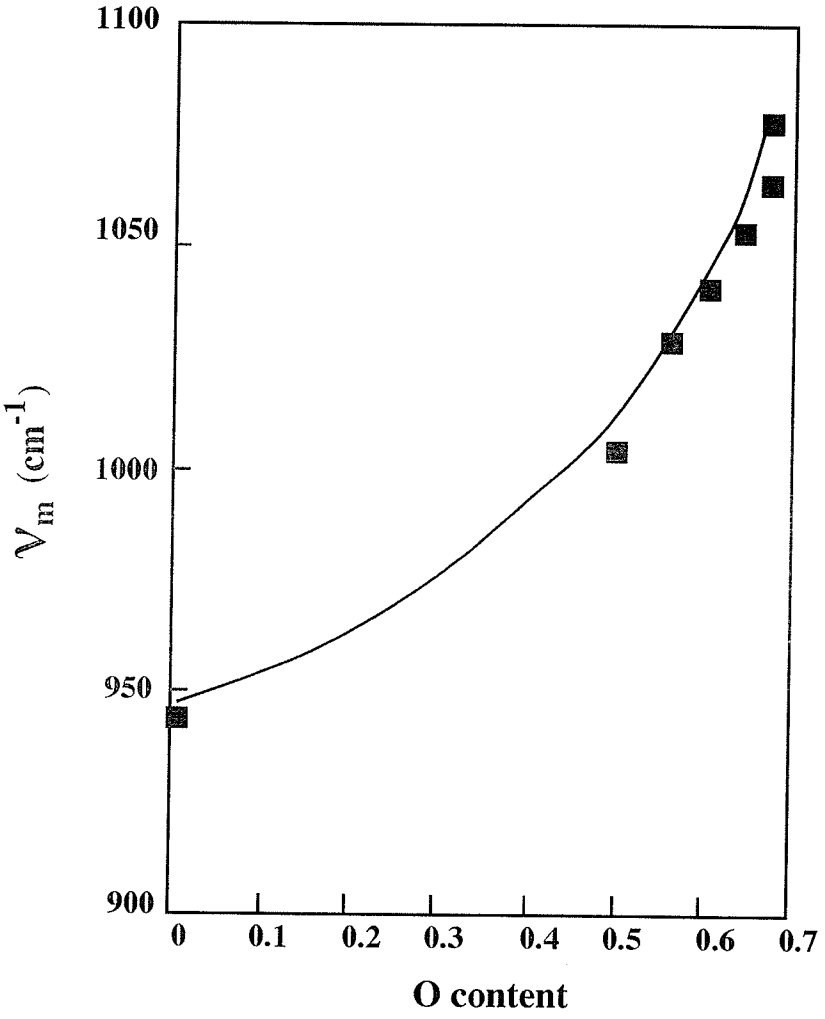

Figure 2.11. The frequency for the peak absorption of the Si-O-Si stretching mode as a function of the O content (after Morimoto et al [2.34]).

such a transition layer.

B. The ellipsometry

Another parameter which provides useful information about the film properties is the refractive index, which can be measured by ellipsometry [2.37, 2.38]. Two parameters measured from ellipsometry are the Azimuth angle Ψ and the phase difference Δ, which are defined on the basis of the ratio of the complex Fresnel reflection coefficients r_p and r_s for the

parallel polarization (p) and the normal polarization (s) upon reflection from a surface, respectively. This ratio is given by:

$$R(\lambda,\phi) = \frac{r_p}{r_s} = \tan\psi e^{i\Delta} \tag{2.10}$$

which depends on the light wavelength, λ, and the incident angle, ϕ. Since r_p and r_s depend on both the complex refractive index of SiO_2 which is given by:

$$n^* = n - ik \tag{2.11}$$

and that of Si given by:

$$n_s^* = n_s - ik_s \tag{2.12}$$

the values of n and k can be determinated form the measured values of Δ and Ψ, if n_s and k_s are known.

The refractive index is directly related to the density of the film. The relation derived by Gladstone Dale [2.39] is given by:

$$\rho = k_1(n - 1) \tag{2.13}$$

and that due to Lorentz-Lorenz (L-L) formula [2.40] by:

$$\rho = k_2\frac{n^2 - 1}{n^2 + 2} \tag{2.14}$$

where n is the refractive index, and k_1 and k_2 are constants. Figure 2.12 shows the plot of equations (2.13) and (2.14) in comparison to the experimental data. It can be seen that the simple Gladstone Dale equation, which is based on the assumption that the materials are basically the same except for variation in the porosity or the openness of the structure, is

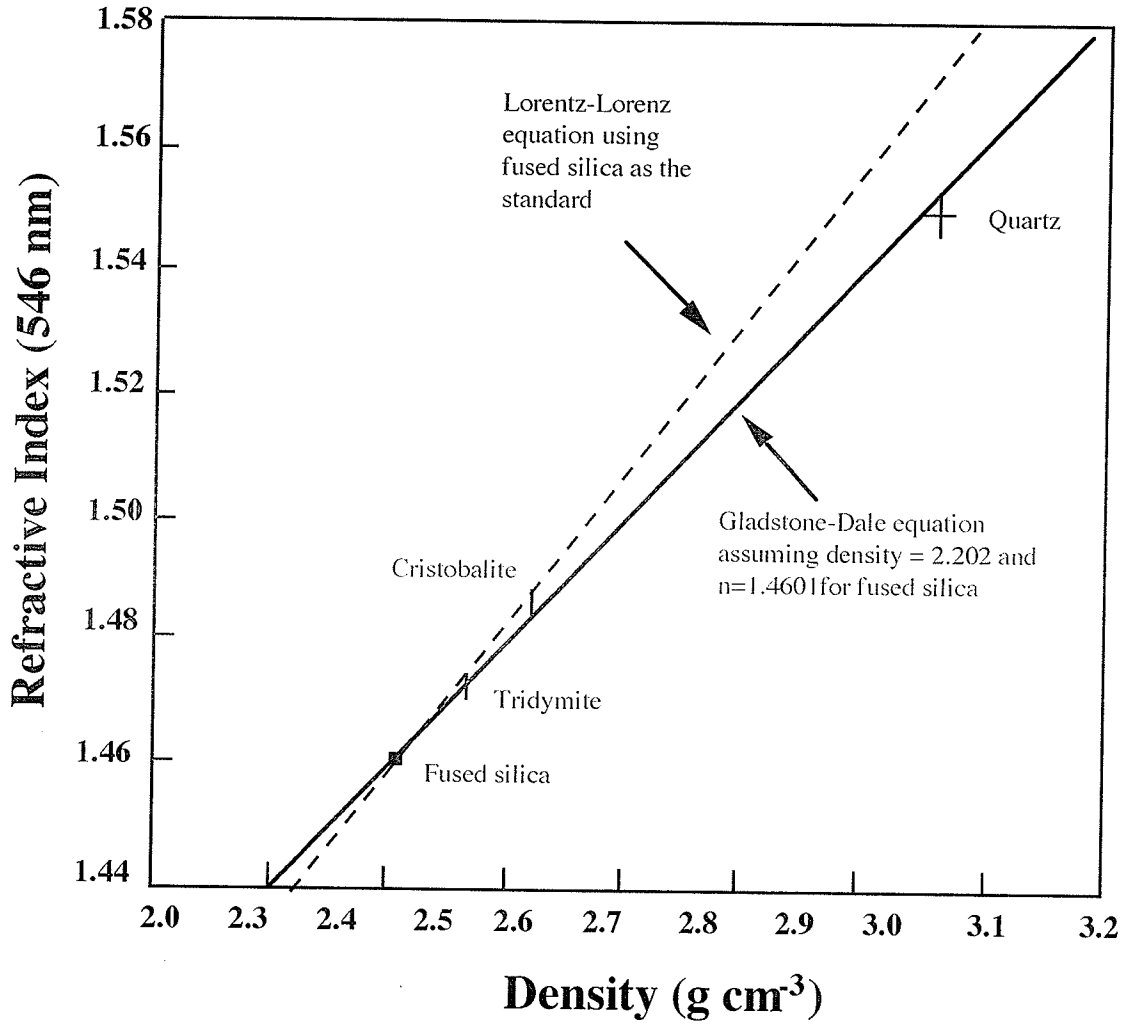

Figure 2.12. Density-refractive index relationship for various forms of silicon dioxide (after Pliskin [2.25]).

fitted better than the simple L-L formula. The relationship between the refractive index and the density of the SiO_2 films has also been found experimentally to follow a linear dependence [2.32]:

$$\rho = -4.789 + 4.785n \tag{2.15}$$

However, Archer [2.41], in the study of SiO_2 film growth by various processing techniques, has concluded that the linear dependence between n and ρ is only true for the stoichiometric SiO_2 films. Non-stoichiometric SiO_2 films such as the silicon rich (SiO_x) films grown by PECVD are

often found to have a higher refractive index than the thermally grown oxide. The high refractive index in silicon rich films can be explained as due to the replacement of Si-O by Si-Si bonds. This can be understood quantitatively in term of the L-L formula where two factors may contribute to this phenomenon, and they are: (i) the decreases in the molar volume as the Si content increases; and (ii) the difference between the polarization of Si-O bond and that of Si-Si bond [2.43]. By taking these into account, the L-L formula can be rewritten as [2.44]:

$$\frac{n-1}{n+2} = \frac{4\pi}{3}\frac{N}{V_m}\sum_j (f_j a_j) \qquad (2.16)$$

where N is the Avogadro number, V_m is the volume, the sum is taken over the polarities a_j of Si-O and Si-Si bonds, and f_j is the fraction of each bond type. In summary, It is emphasized that an early conclusion on the ellipsometric results may lead to a wrong interpretation because a low density ($n < 1.46$) and silicon rich ($n>1.46$) film could yield an apparent refractive index similar to that of the thermally grown oxide ($n\approx1.46$).

2.2.2. Electronic properties

Electronic properties of SiO_2 films are generally measured by means of the MOS devices. The electrical measurements provide information about defects that can not be detected either by the FTIR or ellipsometry.

A. Electric conduction

Electric conduction in the SiO_2 is generally electrode-limited because of their wide band gap (8.8 eV) and consequently high energy barrier at the interface to metal electrode. It can also be said that the electric conduction is not bulk-limited because the SiO_2 film has a low density of traps in the forbidden band gap [2.44] and a relatively high electronic

mobility in the conduction band [2.45]. The energy-band diagram of the MOS capacitor structure is illustrated in Fig. 2.13 for a p-type silicon substrate. The barrier height ϕ_s from the silicon conduction band edge to the oxide conduction band edge is about 3.25 eV and that ϕ_{sh} from the silicon valence band edge to the oxide valence band edge is about 3.8 eV [2.46]. The work function ϕ_m varies from 2.5 eV for magnesium to 4.2 eV for Silver [2.47]. In the dark, electric conduction is due to either Schottky emission of electrons over the barrier ϕ_m, or Fowler-Norheim (FN) tunneling through the triangular barrier into the oxide conduction band. However, the latter has been experimentally confirmed to be responsible for the electric conduction at room temperature [2.48, 2.49]. Emission of holes from the valence band of the silicon into the valence band of the oxide is not expected to play an important role because of a higher barrier height [2.50]. With a positive gate voltage, the silicon surface will be degenerated into an n-type behavior regardless the bulk doping because the metal work function is always smaller than the Si work function. In this case, silicon acts as an electron injecting contact, and the current becomes limited by the injection of electrons from the vicinity of the silicon conduction band edge through the triangular barrier into the oxide conduction band. According to Lenzinder et al [2.46], the injection of electrons into SiO_2 follows the FN theory for electrons injected into vacuum at high fields but for SiO_2-Si systems the following corrections should be included: (1) the electron effective mass (m_e^*) in the SiO_2 conduction band and (2) the image force, which causes the lowering of the barrier height. Even though the corrections have been made, the experimental results agree with experimental results only at high fields. On

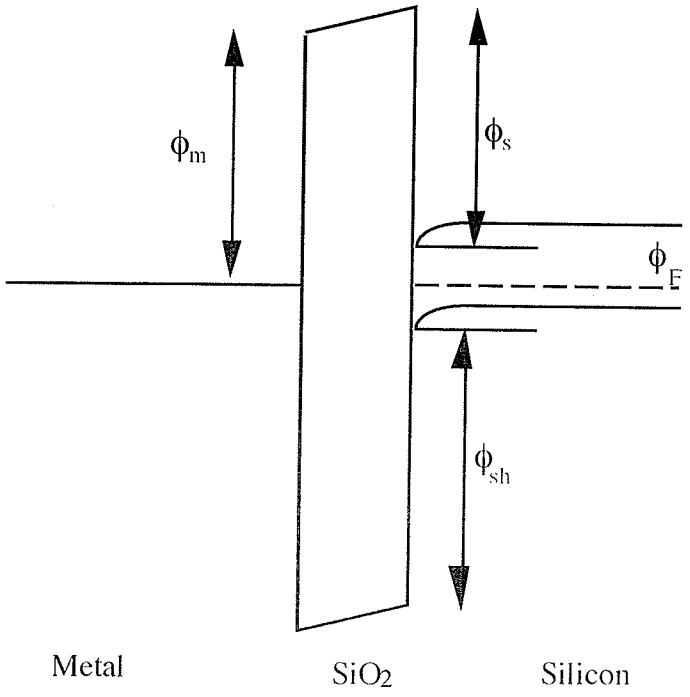

Figure 2.13. The energy band diagram of a typical MOS device with p type Si as the substrate.

the basis of experimental results, Ron et al [2.51] have suggested that the image potential may not be that important, but the defects at the Al-SiO_2 interface may be the main cause for the differences in the values between the theoretical and the experimental results. In fact, Weinberg [2.52] has reported that the image force correction for large barrier height is quite negligible because the image potential rounds the top of the barrier height only; thus, it hardly alters the tunneling distance. Indeed, only 2% correction in the slope of the barrier height and 4% correction in the mass of the electron are needed for the FN current derived without the image force correction [2.53]. The FN current without the image force correction is simply written as [2.52]:

$$J = CF^2 e^{\frac{-\beta}{F}} \tag{2.17}$$

where

$$C = \frac{q^3 m_c}{16\pi^2 h m_e^* \phi_m} \tag{2.18}$$

$$\beta = \frac{4(2m_c^*)^{\frac{1}{2}}}{3qh(\phi_m)^{\frac{3}{2}}} \tag{2.19}$$

where F is the applied field, q, m_e, and h are electronic charge, electron mass, and Plank's constant, respectively. The conduction process in SiO_2 films is not affected by the film thicknesses in the range of 200 and 1500 Å because the required electrical field to produce a given current density is independent on oxide thicknesses [2.48]. The FN current is also independent of substrate type, doping concentration, and injection electrode. However, for film thicknesses under 100 Å, the charge trappings inside the oxide can distort the electric field across the oxide and deviate the FN current away from the ideal one [2.54]. A typical I-V curve on a MOS capacitor with an aluminum electrode is shown in Fig. 2.14. The I-V curve consists of four defined regions: the displacement current (A), the FN current (B), the saturation (ledge) current (C), and the FN current (D). The threshold for electron injected into the stoichiometric SiO_2 films is about 5-6 MV/cm, and it shifts to a lower electric field if the films become silicon rich [2.85]. The ledge in the I-V curve can be used for studying trapping [2.86]. For a ramp rate r, the current increases rapidly with the time according to the FN equation (2.17). As the current and, hence, the trapping rate increases, an internal field rapidly builds up which opposes the electron injection as [2.86]:

$$\frac{dn_t}{dt} = \frac{\sigma j}{q}(N_t - n_t) \tag{2.20}$$

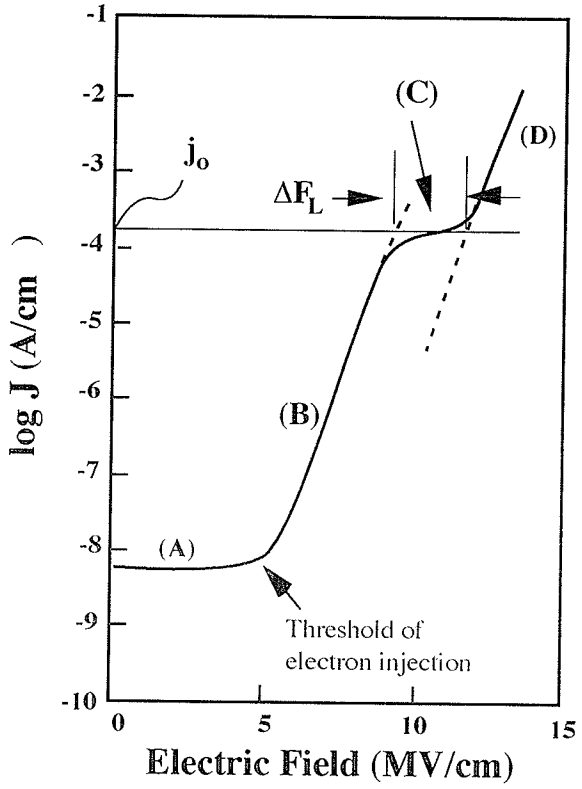

Figure 2.14. A typical I-V curve for oxide on n-type Si with Al electrode (after Solomon [2.86]).

$$\Delta F = \left(\frac{qn_t}{\varepsilon\varepsilon_o}\right)\left(1 - \frac{\bar{x}}{d}\right) \tag{2.21}$$

where n_t and N_t are the filled and total effective trap surface concentrations, respectively, σ is the trap effective cross section, j is the current density, q is the electronic charge, $\bar{x}$ is the distance of the centroid of the charge from the cathode and d is the oxide thickness. When the rate of increase of this internal field approaches the ramp rate r, the current tends to saturate at the value [2.86]:

$$j = \left[\frac{\varepsilon\varepsilon_o r}{\sigma(N_t - n_t)}\right]\left(1 - \frac{\bar{x}}{d}\right) \tag{2.22}$$

This saturation persists until all of the traps are filled, whereafter the current follows a FN curve displaced from the original by a field ΔF_L which is given as:

$$\Delta F_L = \left(\frac{qN_t}{\varepsilon\varepsilon_o}\right)\left(1 - \frac{\bar{x}}{d}\right) \tag{2.23}$$

Therefore, the trapping parameters can be simply obtained from the width of the ledge and the current at which it occurs. The FN technique coupled with the capacitance-voltage technique can be used to distinguish between charge trapped near the interface between the SiO_2 and the cathode and bulk charge. For example, if the FN and the C-V shifts are equals, the charges in the oxide are far from the interface between SiO_2 and the cathode; however, if the C-V shift is larger than the FN shift, the charge is close to the interface between the SiO_2 and the cathode.

B. Electric breakdown phenomena

The yield and the reliability of the MOS devices depend on the electric breakdown strength of the SiO_2 films. Electric breakdown in the SiO_2 films can be influenced by the device parameters such as bias polarity, ramp rate, electrode material, etc. For a p-type silicon MOS system with a negatively biased gate , the silicon surface is in accumulation mode and the entire applied voltage appears across the oxide. With a positively biased gate, the silicon surface can be either in depletion or inversion mode depending on the magnitude of the applied voltage and the minority carrier generation rate. In the thermal equilibrium, the maximum voltage across the silicon is equal to the maximum amount of band bending allowed or about 1 volt. This is a small correction factor for sample that breakdown at roughly 50 V or more. However, when the carrier generation rate is

slow in comparison to the voltage ramp rate a deep depletion can occur; then most of the applied voltage can be seen across the depletion region in the silicon. This could cause avalanche breakdown in the silicon which, in turn, could possibly trigger the breakdown in the SiO_2 films. Thus, the device under test is required to be illuminated by a strong light to increase the carrier generation rate in order to prevent the avalanche breakdown in silicon. It is found that the average value of the maximum breakdown strength for the accumulation mode can be about 0.4 MV/cm less than that for the depletion or the inverted mode [2.55]. Because of this potential difficulty, the measurements of the breakdown strength of the SiO_2 film with a p-type silicon substrate are normally carried out in the accumulation mode. For the MOS devices with an n-type silicon substrate, the behavior is the same as that with a p-type silicon substrate but in the opposite polarity.

The self-healing tends to be dependent on the polarity of the biased voltage. The self-healing occurs for both polarities of the biased voltage, but it is much less frequent when the breakdown strength is measured in the depletion mode. For example, for self-healing to occur in a negatively biased gate MOS devices with a p-type silicon substrate, a thinner Al gate electrode and a thicker SiO_2 layer are required [2.55]. Klein [2.56] has reported that the resistance of the discharge path is about an order of magnitude greater in the depletion mode (positively biased) than in the accumulation mode (negatively biased) for the MOS devices with a p-type silicon substrate. Thus, the initial current surged through the discharge path is an order of magnitude greater in the accumulation mode. The high current (in the accumulation mode) breakdown may vaporize the discharge

path and, hence, self-heal more effectively than the low current (in the depletion mode).

Less self-healing occurs in thin SiO_2 samples [2.55]. The fraction of high field breakdown events decreases with increasing oxide thickness [2.57]. Experimentally, the maximum breakdown strength of silicon dioxide film depends on film thickness, which may be expressed by an empirical equation $F_{br} \propto d^{-x}$ with $0.2 \leq x \leq 0.6$ [2.57-2.58].

The thickness of the gate electrode also influences the self healing events. The thicker the aluminum electrode, the fewer the self-healing breakdown events [2.55], and therefore the final breakdown strength appears lower. The minimum energy, W, required for evaporating the discharge path for self-healing depends on the capacitance area S, and oxide thickness d as:

$$W = \frac{\varepsilon\varepsilon_o S}{2d}(V_t^2 - V_r^2) \tag{2.24}$$

where V_t is defined as the threshold voltage such that no samples undergo self-heal for breakdown voltage lower than V_t. However, all samples with a breakdown voltage higher than V_t are self-healed. V_r is the minimum voltage remaining across the capacitor during a self-healing breakdown event [2.56-2.57].

The area of the electrode can also influence the breakdown. Figure 2.15 shows the fraction of high field breakdown P as functions of the electrode area for three Al electrode thicknesses. The relationship between the final breakdown and the electrode area is often used for the calculation of the defect density, η, which is expressed as [2.49]:

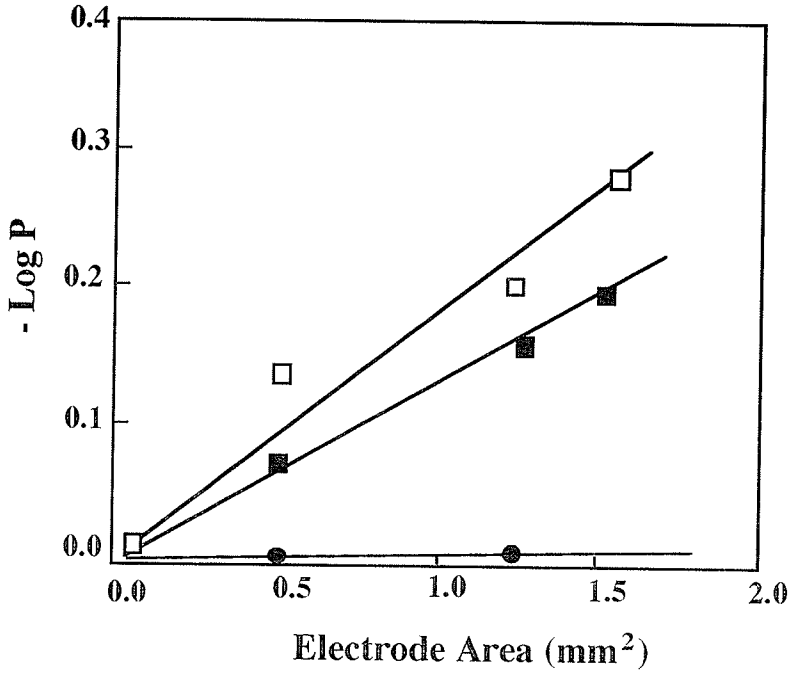

Figure 2.15. The fraction of the total number of breakdowns, P, as a function of the area of the Al electrode for three different electrode thicknesses □ for 4275 Å, ■ for 3150 Å , and ● for 750 Å, (after Osburn et al [2.49]).

$$-\mathrm{Ln}P = \eta S \tag{25}$$

Choice of electrode materials does not influence breakdown to any significant extent. For example, magnesium, chromium, aluminum, molybdenum, gold, and platinum give similar breakdown distributions with the maximum breakdown strength over 8 MV/cm [2.55]; however the electric conduction depends strongly on electrode materials, and many orders of magnitude difference in current levels at a fixed electric field may happen just because of different electrode materials [2.49].

Substrate doping has a rather small influence on the breakdown strength of the SiO_2 films with thicknesses above 500 Å. A high substrate doping reduces the breakdown strength by a few percent at the most. The effects of doping become as large as 20% when SiO_2 thicknesses are reduced to below 200 Å. Also, phosphorous has more influence on the

breakdown strength than boron. This may due to the fact that phosphorous segregates to the silicon during the SiO_2 growth while boron diffuses into the oxide [2.59-2.61].

C. Electrical breakdown theory

Many models have been put forward to explain how wearout in thin insulators would lead to breakdown. These models are generally based on the assumption that the breakdown occurs in two steps [2.62]: (1) During the wearout phase, defects or traps are created inside the oxide [2.63] and at the SiO_2-Si interface [2.64] due to the electrical stressing in the oxides and the current flowing through the oxides. (2) When the concentration of these defects becomes high enough to lead to the creation of a locally high current density then thermal runaway ensures [2.65]. Many techniques have been developed for studying thin oxide wearout and breakdown; however, it has been difficult to couple the two steps. One of the difficulties has been the lack of a consistent model describing the triggering mechanism causing the breakdown [2.66]. A model for trap generation involving impact ionization near the anode has been proposed [2.67]. This model appears to quite describe accurately the wearout and the breakdown in oxide thicker than 200 Å [2.68]. Another model involving the breaking of bonds and the creation of holes in the silicon near the anode and the drift or diffusion of these broken bonds into the silicon dioxide has been suggested [2.69]. However, questions have been raised concerning whether sufficient energy is available in the incoming carries to trigger this process, particularly in thinner oxides [2.68]. The most recent models are related to the trap generation due to the bombardment of hot electrons inside the oxide [2.70, 2.87]. The physical model that has been used to describe

wearout in thin insulators (≤120 Å) is shown in Fig. 2.16. During high electric stressing traps, are generated inside the oxide and at the oxide interfaces by high field emission of the electrons from the SiO_2-Si system. The emission of electrons is accompanied by the generation of the positive trap centers to conserve charge. The trap centers are stable at room temperature, and may be accompanied by motion of the atoms whose atomic bonds have been broken, as shown in Fig. 2.17. The traps, thus, become permanent inside of the oxide and subsequent recapture of an electron would not remove the trap from the silicon oxide structure. The only way to remove the traps would be the use of a high temperature annealing step. These traps are generated, more or less, uniformly throughout the oxide. When the field in the oxide during trap generation exceeds 6 MV/cm, high field generation of the traps occurs [2.71, 2.72]. The traps are generated at different energy levels below the oxide conduction band edge. There was a higher probability of generating shallow traps than of generating deep traps, thus shallow traps are generated early in the stress cycle or at lower stressing voltages, while the deeper traps are generated later in the wearout process. This energy dispersion relationship of the traps is supported by the measured fluence and field dependence of trap generation. No impact ionization has been found in this study, and this model can explain well the breakdown in thin oxide.

D. Defects in the SiO_2-Si systems

Electronic defects are the limiting factor in the performance of devices involving a metal oxide semiconductor structure. The fundamental defects in the SiO_2-Si systems are the interface trapped charges and the

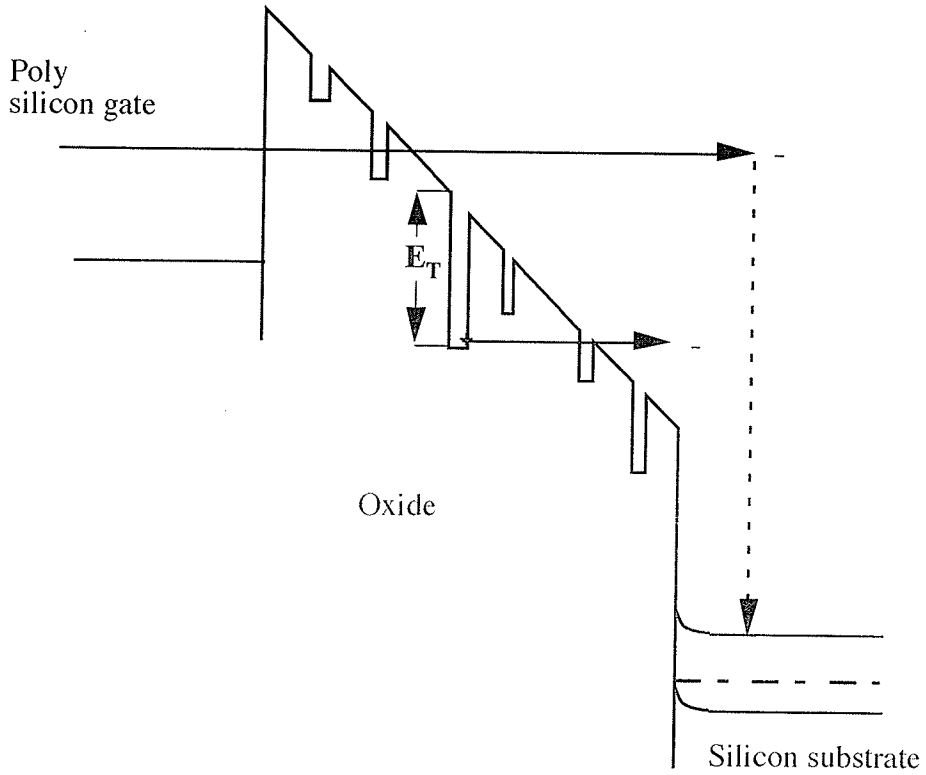

Figure 2.16. Traps are generated inside the oxide at different positions and energies as the oxide wear out (after Dumin [2.70]).

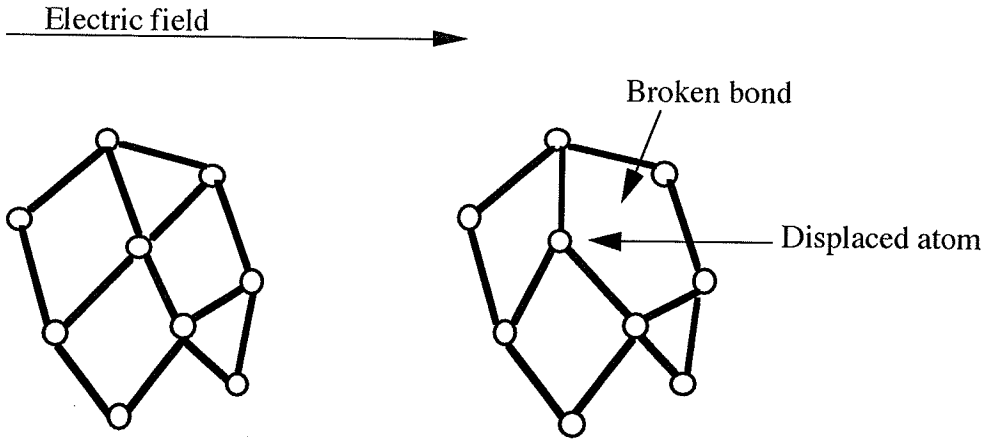

Figure 2.17. The model for atomic movement accompanying bond breaking and trap generation (after Dumin [2.70])

oxide trapped charges [2.73] . These charges can be calculated on the basis of the capacitance-voltage (C-V) and the current voltage (I-V) characteristics [2.74]. The nature, location, and sources of these charges have been studied extensively in the past three decades [2.74].

i. Defects at the SiO_2-Si interface

The interface trapped charges, Q_{it}, are located at the SiO_2-Si interface (within 10 Å of the Si-SiO_2 interface) [2.74]. The interface trap density D_{it} and the silicon surface energy level are related by a U sharp characteristic. There are 3-models that have been put forward to explain this U-shape characteristic distribution, and they are the coulombic, the bond, and the defect models. These models are described briefly as follows:

a. The coulombic model

The coulombic model is proposed by Goetberger et al [2.75]. Based on this model, charges in the oxide induce potential wells in the silicon; within these wells are identified with interface trap levels. For the most part, such interface trap levels are located in energy levels near the silicon band edges. The mid-gap levels are expected only if many charges are clustered together producing a deep potential well. However, such clusters are unlikely, thus, the density of the mid-gap levels is expected to be smaller than the density of shallow trap levels, giving a U-shape distribution.

b. The bond model

Laughin et al [2.76] have suggested that the distribution of bond angles or stretched bonds at the silicon surface is related to the distribution of interface trap levels because the strain from SiO_2 causes a distortion on

the silicon side of the interface. The distortion of the Si-Si bonds produces anti-bonding level in the upper half of the silicon band gap and bonding level in the lower-half of the silicon band gap. This produces a shallow trap level at the band edges whereas a layer of distortion is needed to produce trap levels near the mid-gap. However, this model is based upon the argument by analogy and is not quantitatively proven.

On a different approach Sakurai et la [2.77] have reported that D_{it} is a result of the bond stretching at the interface. Using the tight-binding model for the silicon and the Beth Lattice model for the SiO_2, Sakurai et al have shown that the stretched Si-O bonds at the interfacial plane can cause trap levels in the lower half of the band gap, and that oxygen vacancy or stretched Si-Si bonds can cause trap levels in the upper half of the band gap. Furthermore, the silicon dangling bonds at the SiO_2-Si interface can produce trap levels near the mid-gap.

c. The defect model

The defects within or near the interfacial region are caused by stacking faults and micro-pores as well as various atomic or molecular fragments left as a residue of imperfect oxidation. Two most common defects are assumed for interface traps, which are: excess silicon [2.78], and impurities [2.79].

The excess silicon at the Si-SiO_2 interface is due to non-complete oxidation of the silicon or vacancies in silicon during oxidation. Hence, the silicon atom shares three of its four valence electrons with neighboring silicon atoms. The remained unsatisfying valence bond acts as a hole trap becoming positively charged after capturing a hole and remaining neutral

when empty. There is some tentative experimental evidence that trivalent silicon exits in SiO_2 and may act as interface trap. Nishi [2.80] and Poindexter et al [2.81] have reported that the spin resonance signal P_b in the Si-SiO_2 interface behaves in the same manner as the mid-gap interface traps under oxidation or after annealing. They believe that the electron spin resonance signals are due to trivalent silicon, and the excess silicon at the Si-SiO_2 interface results in the interface trap charges. The P_b center acting as defects in the SiO_2-Si system are the defects which have been the most thoroughly studied. It occurs in two different variations depending on silicon interface orientation. On (111) silicon, it has one form, a silicon atom bonded to three other silicon atoms in the silicon surface at the interface, with a non-bonded orbital normally containing one (paramagnetic) electron, and directed perpendicular to the interface into the SiO_2 as shown in Fig. 2.18a. On (110) silicon, the same center occurs in two of the four crystalographically possible orientations, along the nominal (111) bond directions aimed into the oxide as shown in Fig. 2.18b. On (100) silicon, there are two kinds of the P_b center. The P_{bo} center is essentially like the lone P_b variant occurring on (111), but is aimed along the two allowable (111) directions at the interface. The P_{b1} has a different chemical structure and is thought to be due to the =Si-O- defects at the surface as shown in Fig. 1.18c.

The other types of defects are impurity atoms at the interface. Because the strain at the interface creates a potential minimum for impurities, the interface can accommodate many of the impurities incorporated in the relatively open SiO_2 lattice. There is also a strain region at the metal-SiO_2 interface. Strained regions at either interface are likely to act as a sink for

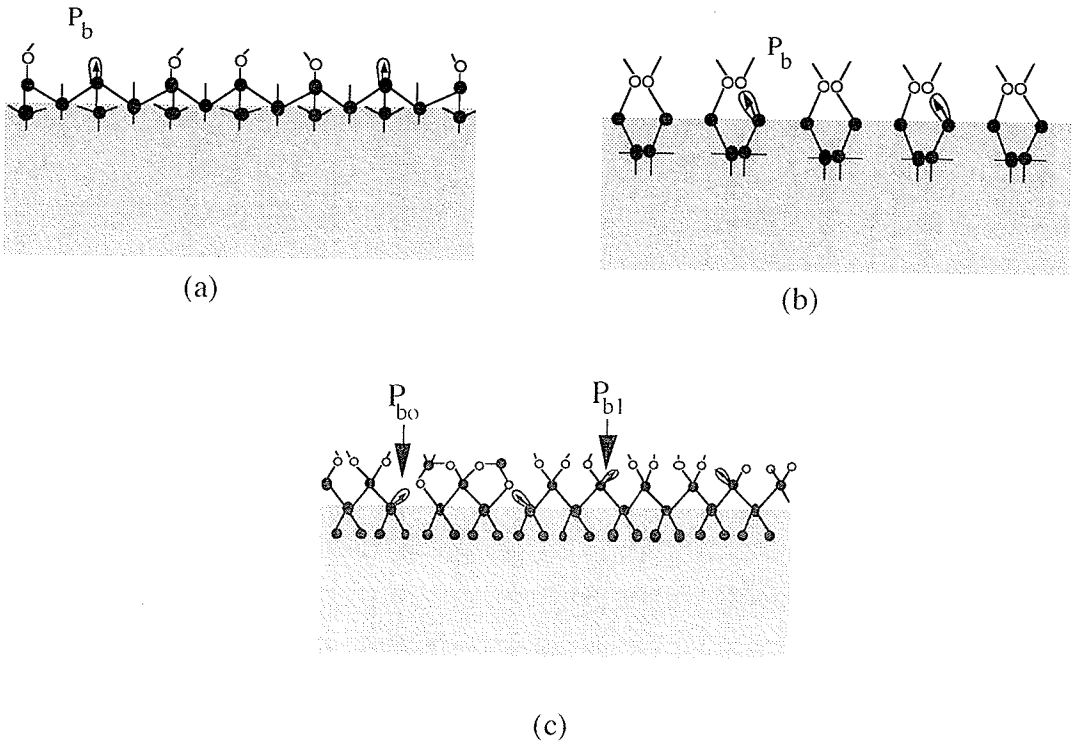

Figure 2.18. The P_b centers in the SiO_2-Si system for (a) (111) Si, (b) (110) Si, and (c) (100) Si.

the impurities to incorporate. This model has been confirmed experimentally by Kar et al's work [2.79], which shows that metal impurities can induce interface traps.

ii. Oxide Charges

Oxide charge includes the mobile-ionic charge, the oxide-fixed charge, and the oxide-trapped charge. In the following, these charges will be discussed separately.

a. Mobile impurity ions

The mobile impurity ions are normally due to positive alkali ions (Na^+, K^+, Li^+) in the oxide. These ions will drift when the gate is biased and heated at temperatures above 100 °C. However, other ions such as H^+ or H_3O^+ will drift under bias at room temperature. Thus, in some cases the

mobile impurity ions can cause device instabilities even at room temperature. All mobile impurity ions can be gettered at elevated temperature (>900 °C) using a complexity agent such as phosphor silicate glass.

b. Oxide fixed charge

The candidate for the oxide fixed charge is the non-bridging oxygen atom. In a normal SiO_2 lattice, oxygen shares electrons with adjacent silicon atoms, forming a "bridge" between the two silicon atoms. When one of the Si-O bonds is broken, the formerly bridging oxygen atom is now called a non bridging oxygen atom. The non-bridging oxygen atom shares one of its two valence electrons with the remaining silicon atom, and its unsatisfied valence bond acts as an electron trap, becoming negatively charged by electron capture and remaining neutral when empty. Non bridging oxygen defects at the SiO_2-Si interface may be due to: a) the strain in the region near the interface and b) water related electron traps near the SiO_2 interface. Non-bridging oxygen could act as negatively charged centers when the water-related traps capture energetic electrons. However, because electrons are seldom present in the conduction band of the SiO_2, the formation of negatively charged centers may be impossible. More probable may be the loss of an electron from a non-bridging oxygen center near the SiO_2-Si interface to the silicon, making it a positively charged center leading to the formation of the oxide fixed charge [2.88].

c. The oxide trapped charge

The possible candidate for oxide trapped charge (Q_{ot}) is the E' center. The E' center is associated with oxygen vacancy sites. Electron spin resonance (ESR) measurements indicate that an electron localizes

preferentially onto one of the two silicon dangling bonds directs into the vacancy, and that the other silicon atom is positive charged, relaxes out of the vacancy towards a planar configuration as shown in Fig. 2.19 [2.84]. Most of the Q_{ot} can be annealed out by low temperature annealing in the forming gas. The Q_{ot} is usually located either near the metal-SiO_2 interface or at the SiO_2-Si interface. One exception is that if the oxide traps are introduced by ionizing radiation such as X-rays, electrons, neutrons, etc., then they may be located anywhere in the oxide. That is why sometimes Q_{ot} is called the radiation induced trapped charge.

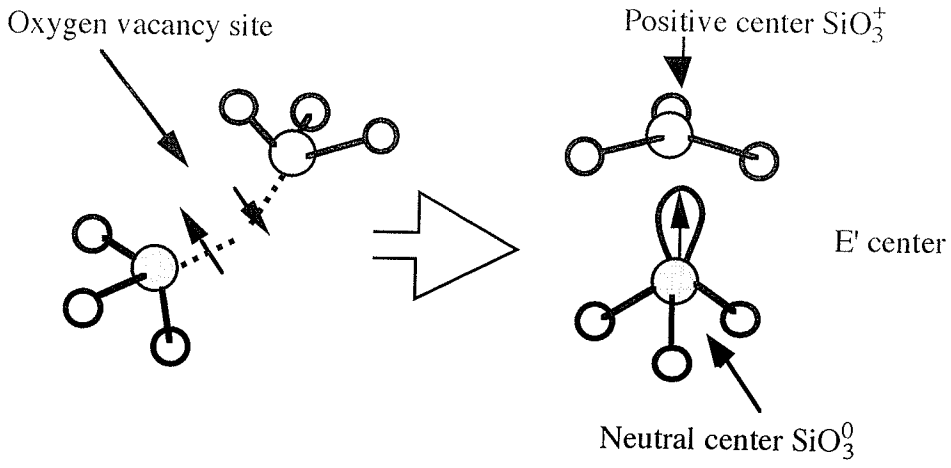

Figure 2.19. Diagram representation of the formation of an E' center.

References for chapter 2

[2.1] T. V. Herak, T. T. Chau, D. J. Thompson, S. R. Mejia, D. A. Buchanan, and K. C. Kao, "*Low Temperature Deposition of SiO_2 Films from ECR Microwave Plasma*," J. Appl. Phys. **63**, 4744(1988).

[2.2] T. T. Chau, T. V. Herak, D. J. Thompson, S. R. Mejia, D. A. Buchanan, R. D. McLeod, and K. C. Kao, "*Silicon Dioxide Films Fabricated by ECR Microwave Plasma*," IEEE Trans. Elec. Insul., **25**, 593(1990).

[2.3] B. Robinson, T. N. Nguyen, and M. Copel, in "*Deposition and Growth Limits for Microelectronics*", Edited by G. W. Rubloff, AIP, Series 4, Anaheim, CA, 1987, pp. 112-123.

[2.4] P. D. Richard, R. J. Markunas, G. Lucovsky, G. G. Fountain, A. N. Mansour, and D. V. Tsu, "*Remote Plasma Enhanced CVD Deposition of Silicon Nitride and Oxide for Gate Insulators in (In, Ga)As FET Devices*," J. Vac. Sci. Technol. **A3**, 867(1985).

[2.5] G. Lucovsky, D. V. Tsu, and G. N. Parsons, in "*Deposition and Growth Limits for Microelectronics*", Edited by G. W. Rubloff, AIP, Series 4, Anaheim, CA, 1987, pp. 156.

[2.6] B. Chapman, "*Glow Discharge Process*", John Willey & Son, New York, 1980, chapter 3, Page 78.

[2.7] K. Suzuki, A. Sawabe, and T. Inuzuka, "*Growth of Diamond Thin Films by dc Plasma Chemical Vapor Deposition and Characteristics of the Plasma*," Jpn. J. Appl. Phys., **29**, 153(1990).

[2.8] J. L. Vossen, "*Glow Discharge Phenomena in Plasma Etching and Plasma Deposition*," J. Electrochem. Soc., **126**, 319 (1979).

[2.9] R. S. Rosler, "*The Evolution of Commercial Plasma Enhanced CVD Systems*," Solid state Technol., **34(6)**, 67(1991).

[2.10] F. Jansen, in "*Plasma deposited of Thin Films*", Edited by J. Mott and F. Jansen, 1986, CRC press, pp 1-17.

[2.11] P. Singer, "*Trends in Plasma Sources the Search Continues*," Semicon. Inter., **15(8)**, 52(1992).

[2.12] J. Batey and E. Tierney, J. Stasiak and T. N. Nguyen, "*Plasma Enhanced CVD of High Quality Insulating Films*," Applied Surface Sci., **39**, 1(1989).

[2.13] S. R. Mejia, M. Sc. Thesis, "*The effects of Deposition Parameters on Hydrogenated Amorphous Silicon Films by Microwave Glow Discharge Techniques*," University of Manitoba, 1984.

[2.14] J. F. Currie, P. Depelsenaire, J. P. Huot, L Paquin, M. R. Weitheimer, and A. Yelon, "Compositional Characterization of Microwave Plasma a-Si:H Films," Can. J. Phys., **61**, 582(1983).

[2.15] P. Pomathiod, R. Debrie, Y. Arnal, and J. Pelletier, "*Microwave Excitation of Large volume of Plasma at ECR in Multipolar Confinement*," Phys. Lett., **106 A**, 301(1984).

[2.16] S. R. Mejia, R. D. McLeod, K. C. Kao, and H. C. Card, "*The effects of Deposition Parameters on Hydrogenated Amorphous Silicon Films by Microwave Glow Discharge Techniques*," J. Non-Cryst. Solids, **59&60**, 727(1983).

[2.17] R. D. McLeod, "*Studies of Amorphous Silicon*," Ph. D. Thesis, University of Manitoba, 1985.

[2.18] T. T. Chau, "*Microwave Plasma Processing of Thin Film Semiconductors*," M. Sc. Thesis, University of Manitoba, 1988.

[2.19] K. Machida and H. Oikawa, "*SiO_2 Planarization Technology with biasing and Electron Cyclotron Resonance Plasma Deposition for Submicron Connection*," J. Vac. Sci. Technol., **B4**, 818(1986),

[2.20] T. V. Herak, T. T. Chau, D. J. Thomson, and S. R. Mejia, D. A. Buchanan, and K. C. Kao, "*Low Temperature Deposition of Silicon Dioxide*," J. Appl. Phys., **65**, 2457(1989).

[2.21] C. T. Grabiel and J. P. Mcvittie, "*How Plasma Etching Damage Thin Gate Oxide*," Solid State Technol., **35(6)**, 81(1992).

[2.22] S. A. Bell and D. W. Hess, "*Radiation Damage to Thermal Silicon Dioxide Films in Radio Frequency and Microwave Down Stream Photoresist Striping Systems*," J. Electrochem. Soc., **139**, 2904(1992).

[2.23] G. Lucovsky, D. V. Tsu, S. S. Kim, R. J. Markunas, and G. G. Fountain, "*Formation of Thin Film Dielectric by Remote Plasma Enhanced Chemical Vapor Deposition*," Appl. Surface. Sci., **39**, 33(1989).

[2.24] S. Doziba, S. Meikle, and R. W. Streater, "*Downstream Plasma Induced Deposition of SiN_x on Si , InP, and InGAs*," J. Electrochem. Soc., **134**, 2599(1987).

[2.25] W. A. Pliskin, "*Comparison of Properties of Dielectric Films Deposited by Various Methods*," J. Vac. Sci. Technol., **14**, 1064(1977).

[2.26] R. Iyer and D. L. Lile, "*Kinetics of Low Pressure CVD Growth of SiO_2 on InP and Si*," J. Electrochem. Soc., **135**, 691(1988).

[2.27] S. T. Pantelides and W. A. Harison, "*Electronic Structure, Spectra, and Properties of 4:2 Coordinated Materials: Crystalline and Amorphous SiO_2 and GeO_2*," Phys. Rev., **B13**, 2667(1976).

[2.28] G. Lucovsky, J. T. Fitch, D. V. Tsu, and S. S. Kim, "*Atomic Structure in SiO_2 Thin Films Deposited by Remote Plasma-Enhanced Chemical Vapor Deposition*," J. Vac. Sci. Technol., **A7**, 1136(1989).

[2.29] A. Leman, L. Shumann, and K. Hubner, "*Optical Phonons in Amorphous Silicon Dioxides*," Phys. Status. Solidi., **B117**, 689(1983).

[2.30] P. G. Pai, S. S. Chao, Y. Takagi, and G. Lucovsky, "*Infrared Spectroscopic Study of SiO_x Films Produced by Plasma Enhanced Chemical Vapor Deposition*," J. Vac. Sci. Technol. **A3**, 689(1986).

[2.31] F. L. Galeener and G. Lucovsky, "*Longitudinal Optical Vibrations in Glass*," Phys. Rev. Lett. **37**, 1474 (1976).

[2.32] W. A. Pliskin and H. S. Lehman, "*Structural Evaluation of Silicon Dioxide Films*," J. Electrochem. Soc., **112**, 1013(1965).

[2.33] A. C. Adams, "*Plasma Deposition of Inorganic Films*," Solid State Technol., **26(4)**, 135(1983).

[2.34] A. Morimoto, H. Noriyama, and T. Shimizu, "*Structure and Defects in Amorphous Si-O Films*," Jpn. J. Appl. Phys., **26**, 22(1987).

[2.35] S. S. Chao, G. Lucovsky, S. Y. Lin, C. K. Wong, P. D. Richard, D. V. Tsu, Y. Takagi, J. E. Keem, J. E. Tyler, and P. Pai, "*A Study of Electronic States in a-SiO_x and a-SiN_x Thin Films by Infrared, Auger Electron and X-Ray Photoelectron Spectroscopies*," J. Noncryst. Solids, **77&78**, 929(1985).

[2.36] I. W. Boyd and J. I. B. Wilson, "*Silicon-Silicon Dioxide Interface: An Infrared Study*," J. Appl. Phys., **62**, 3195(1987).

[2.37] R. M. Azzam and N. M. Bashara, "*Ellipsometry and Polarized Light*", North -Holland, Amsterdam 1977.

[2.38] F. L. McCrackin, E. Passaglia, R. R. Stromberg, and H. L. Steinberg, "*Measurement of the Thickness and Refractive Index of Very Thin Films and the Optical Properties of Surfaces by Ellipsometry*," J. Res. Natt. Bur. Stand. Sect. A., **67 A**, 363(1963).

[2.39] J. H. Gladstone and T. P. Dale, "*Researches on the Refraction and Dispersion and Sensitiveness of Liquid*," Trans. Roy. Soc., **153**, 317(1863).

[2.40] M. Born and E. Wolf, "*Principle of Optics*", Pergamon, Oxford, 1965, 3rd Rev. ed. p87.

[2.41] A. J. Archer, "*Determination of the Properties of Films on Silicon by the Method of Elipsometry*," J. Opt. Soc. Amer., **52**, 970(1962).

[2.42] J. E. Stanworth, "*Principal Properties of Glass*", Clarendon, Oxford, 1950, p.56.

[2.43] G. Lucovsky, M. J. Manitini, J. K. Srivastava, and E. A. Irene, "*Low Temperature Growth of Silicon Dioxide Films: A Study of Chemical Bonding by Ellipsometry and Infrared Spectroscopy*," J. Vac. Technol., **B5**, 530(1987).

[2.44] R. William, "*Photo Emission of Electrons from Silicon into Silicon Dioxide*," Phys. Rev., **140A**, 569(1965).

[2.45] A. M. Goodman, "*Electron Hall Effect in Silicon Dioxide*," Phys. Rev., **164**, 1145(1967).

[2.46] M. Lenzinder and E. H. Snow, "*Fowler-Nordheim Tunneling into Thermally growth SiO_2*," J. Appl. Phys., **40**, 278(1969).

[2.47] B. E. Deal, E. H. Snow, and C. A. Mead, "*Barrier Energies in Metal-Silicon Dioxide-Silicon Structures*," J. Phys. Chem. Solids, **27**, 1873(1966).

[2.48] E. L. Murphy and R. H. Good, Jr., "*Thermiomic Emission, Field Emission, and the Transition Process*," Phys. Rev., **102**, 1464(1956).

[2.49] C. M. Osburn and E. J. Weitzman, "*Dielectric Breakdown in Silicon Dioxide Films on Silicon. II. Influence of Processing and Materials*," J. Electrochem. Soc., **119**, 603(1972).

[2.50] A. M. Goodman, "*Photoemission of Holes from Silicon into Silicon Dioxide*," Phys. Rev., **152**, 780(1966).

[2.51] M. Av-Ron, M. Shatzker, T. H. DiStefano, and R. A. Gdula, "*Electron Tunneling at Al-SiO_2 Interfaces*," J. Appl. Phys., **52**, 2897(1981).

[2.52] Z. A. Wienberg, "*On Tunneling in Metal Oxide Silicon Structures*," J. Appl. Phys., **53**, 5052(1982).

[2.53] R. E. Burgers, H. Kroemer, and J. M. Houston, "*Correct Values of Fowler-Nordheim Field Emission Function v(y) and s(y),*" Phys. Rev., **90**, 515(1953).

[2.54] Y. N. Cohen, J. Shappir, and D. F. Bentchkowsky, "*Measurement of Fowler-Nordheim Tunneling Currents in MOS Structures Under Charge trapping Conditions*," Solid. State Electron., **28**, 717(1985).

[2.55] C. M. Osburn and D. W. Ormond, "*Dielectric Breakdown in Silicon Dioxide Films on Silicon: I. Measurement and Interpretation*," J. Electrochem. Soc., **119**, 591(1972).

[2.56] N. Klien, "*The Mechanism of Self Healing Electrical Breakdown in MOS Structures*," IEEE Trans Electron. Devices, **ED13**, 788(1966).

[2.57] C. M. Osburn and D. W. Ormond, "*Dielectric Breakdown in Silicon Dioxide Films on Silicon: II. Influence of Processing and Materials*," J. Electrochem. Soc., **119**, 597(1972).

[2.58] I. H. Pratt, "*Thin Film Dielectric Properties of r.f. Sputtered Oxides*," Solid State Technol., **12(12)**, 49(1969).

[2.59] A. S. Grove, O. Leistiko, Jr., and C. T. Sah, "*Redistribution of Acceptor and Donor Impurities During Thermal Oxidation of Silicon*," J. Appl. Phys., **35**, 2695(1964).

[2.60] B. E. Deal, A. S. Grove, E. H. Snow, and C. T. Sah, "*Observation of Impurity Redistribution During Thermal Oxidation of Silicon Using the MOS Structure*," J. Electrochem. Soc., **112**, 308(1965).

[2.61] J. S. T. Huang and L. C. Welliver, "*On the Redistribution of Boron in the Diffused Layer during Thermal Oxidation*," J. Electrochem Soc., **117**, 1577(1970).

[2.62] E. Harari, "*Conduction and Trapping of Electron in Highly Stress Ultra Thin Films of Thermal SiO_2*," Appl. Phys. Lett., **30**, 601(1977).

[2.63] E. Harari, "*Dielectric Breakdown in Electrically Stressed Thin Films of Thermal SiO_2*," J. Appl. Phys., **49**, 2478 (1978).

[2.64] Y. N. Cohen, J. Shappir, and D. Frohman-Bentchkowsky, "*Determination of SiO_2 Trapped Charge Distribution by Capacitance-Voltage Analysis of Undopped Polycrystalline Silicon-Oxide-Silicon Capacitors*," Appl. Phys. Lett., **44**, 417(1984).

[2.65] Y. UraoKa and K. Tuji, "*A New Techniques for Evaluating Gate Oxide Reliability Using a Phonon Emission Method*," IEICE Trans. Electron., **E76-C**, 519(1993).

[2.66] J. Sune, I. Placencia, N. Barniol, E. Farres, and X. Aymerich, "*Degradation and Breakdown of Gate Oxides in VLSI Devices*," Phys. Status Solidi, **A111**, 675(1989).

[2.67] D. DiMaria, E. Cartier, and D. Arnold, "*Impact Ionization, Trap Creation, Degradation, and Breakdown in Silicon Dioxide Films on Silicon*," J. Appl. Phys., **73**, 3367 (1993).

[2.68] D. Arnold, E. Cartier, and D. DiMaria, "*Theory of High Field Electron Transport and Impact Ionization in Silicon Dioxide*," Phys. Rev., **B49**, 278(1994).

[2.69] I. C. Chen, S. Holland, and C. Hu, "*Hole Trapping and Breakdown in Thin SiO_2*," IEEE Electron Device Lett., **EDL-7**, 164(1986).

[2.70] D. J. Dumin, "*Wearout and Breakdown, in Thin Silicon Dioxide*," J. Electrochem. Soc., **142**, 1272(1995).

[2.71] N. Shiono and M. Itsumi, "*A Lifetime Projection Method Using Series Model and Acceleration Factors for TDDB Failures of Thin Gate Oxides*," Pro. Int. Rel. Phys. Symp., **31**, 1(1993).

[2.72] J. S. Suehle, P Chaparala, C. Messick, W. M. Miller, and K. C. Boyko, "*Field and Temperature Acceleration of Time-Dependent Dielectric Breakdown in Intrinsic Thin SiO_2*," Pro. Int. Rel. Phys. Symp., **32**, 120(1994).

[2.73] B. E. Deal, "*Standardized Terminology for oxide Charges Associated with Thermal Oxidized Silicon*," IEEE Trans. Electron. Dev., **ED27**, 606(1980).

[2.74] E. H. Nicollian and A. Goetzberger, "*The Si-SiO_2 Interface-Electrical Properties as Determined by the Metal-Insulator-Silicon Conductance Technique*," Bell Sys. Tech. J., **46**, 1055(1967).

[2.75] A. Goetzberger, V. Heine, and E. H. Nicollian, "*Surface States in Silicon from Charges in the oxide Coating*," Appl. Phys. Lett., **12**, 95(1968).

[2.76] R. B. Laughin, J. D. J. Nopoulous, and D. J. Chali, in "*The Physics of SiO_2 and its interfaces*", Edited by S. T. Pantelides, Pergamon, NY, 1978, chapter 6, pp. 321-327.

[2.77] T. Sakurai and T. Sugano, "*Theory of Continuously Distributed Trap States at Si-SiO_2 Interfaces*," J. Appl. Phys., **52**, 2889(1981).

[2.78] C. C. Chang, in "*Semiconductor Characterization Techniques*", Edited by P. W. Barners and G. A. Rozgonyi , The Electrochem. Soc. Proceeding, Princeton, NY, 1978, p106.

[2.79] S. Kar and W. E. Dahlke, "*Potentials and Direct Current in Si (20 to 40 Å) SiO_2-Metal Structures*," Solid State Electron., **15**, 869(1972).

[2.80] Y. Nishi, "*Study of Silicon-Silicon Dioxide Structure by Electron Spin Resonance*," Jpn. Appl. Phys., **10**, 52(1971).

[2.81] E. H. Poindexter, E. R. Ahlstrom, and P. J. Caplan, in "*The Physics of SiO_2 and Its Interfaces*", Edited by S. T. Pantelides, Pergamon, NY, 1978, chapter 4, p. 227.

[2.82] R. Schmitt, "*Ultra-Stable Si-SiO_2 Interface*," J. Electrochem. Soc., **116**, 249c(1969).

[2.83] S. I. Raider and A. Berman, "*On the Nature of Fixed Oxide Charge*," J. Electrochem. Soc., **125**, 629(1978).

[2.84] D. L. Griscom, "*Electron Spin in Glass*," J. Non. Cryst. Solid, **40**, 211(1980).

[2.85] D. J. DiMaria, D. W. Dong, C. Falcony, T. N. Theis, J. R. Kirtley, J. C. Tsang, D. R. Young, F. L. Pesavento, and S. D. Brorson, "*Charge Transport and Trapping Phenomena in Off-Stoichiometric Silicon Dioxide Films*," J. Appl. Phys., **54**, 5801(1983).

[2.86] P. Solomon, "*High Field Electron trapping in SiO_2*," J. Appl. Phys., **48**, 3843(1977).

[2.87] K. C. Kao, "*New Theory of Electrical Discharge and Breakdown in Low Mobility Condensed Insulators*," J. Appl. Phys., **55**, 752(1984).

[2.88] E. H. Nicollian and J. R. Brews, "*MOS Physics and Technology*", John Wiley and Sons, NY, 1982.

3

The Close Proximity Plasma Processing System

In chapter 2, the principles and performance of various plasma processing systems, which have been put forward, were described. These systems each have their own short-comings and to overcome these, a close proximity plasma processing (CPPP) system has been developed. This system is in fact an ECR microwave plasma processing system consisting of a plasma chamber and a processing chamber as well as a new apparatus called the "species selector and energy controller (SSEC)." With this new SSEC apparatus, the substrates can be placed close to the plasma and this is why this system is called the CPPP system. In the present chapter, this system will be described in some detail. Some experimental results will then be presented to demonstrate that the properties of SiO_2/Si systems with the SiO_2 fabricated by the CPPP system are much better than those with the SiO_2 fabricated by the conventional ECR microwave plasma processing system without the SSEC apparatus.

3.1. The ECR Microwave CPPP system and the SSEC

The ECR microwave CPPP system is shown schematically in Fig. 3.1. A magnetron operating in a continuous mode at a frequency of 2.45 GHz is used to generate the microwave power. The plasma chamber and the processing chamber are constructed as a stainless steel wave guide, 34 cm long with standard dimensions of the WR-284 wave guide. A turbo-molecular pump is used in conjunction with a chemical rotary pump for

evacuating the system to a base pressure of 10^{-6} torr. The operating pressure for film deposition is in the range of 10^{-4} to 10^{-1} torr, and is monitored by a capacitance manometer. A water cooled coil is mounted around the plasma chamber to provide an axial magnetic field for confining the plasma in the transverse direction and creating an ECR condition. The plasma chamber and the processing chamber are physically separated by the SSEC and therefore they can not see each other, as shown in Fig. 3.1. The end of the plasma chamber is vacuum sealed by a quartz window, and the end of the processing chamber by a stainless steel substrate supporter flange. The microwave power is fed through the quartz window in the TE_{10} mode. The plasma chamber and the processing chamber can be heated to any temperature up to 400 °C by a thermostatically controlled heating element surrounding the chambers. For the fabrication of SiO_2 films, a gas containing oxygen (N_2O) or oxygen at a flow rate of 10 sccm is fed into the plasma chamber via gas inlet 1 and a gas mixture containing silicon (10% SiH_4 in Ar) is fed into the processing chamber in front of the substrate via gas inlet 2. The substrate supporter is mounted in such a way that substrate surfaces are perpendicular to the chamber axis, and it can also be heated to any temperature up to 400 °C by a thermostatically controlled tungsten lamp inserted beneath the table surface. An electrical feed-through also facilitates the plasma characterization and the control of the substrate temperature.

The basic function of the SSEC is to suppress the traffic of the energetic electrons, ions, and photons in order to avoid their bombardment on the substrates and the on-growing films. Under the ECR condition, the magnetic field confines the plasma around the plasma chamber axis, thus

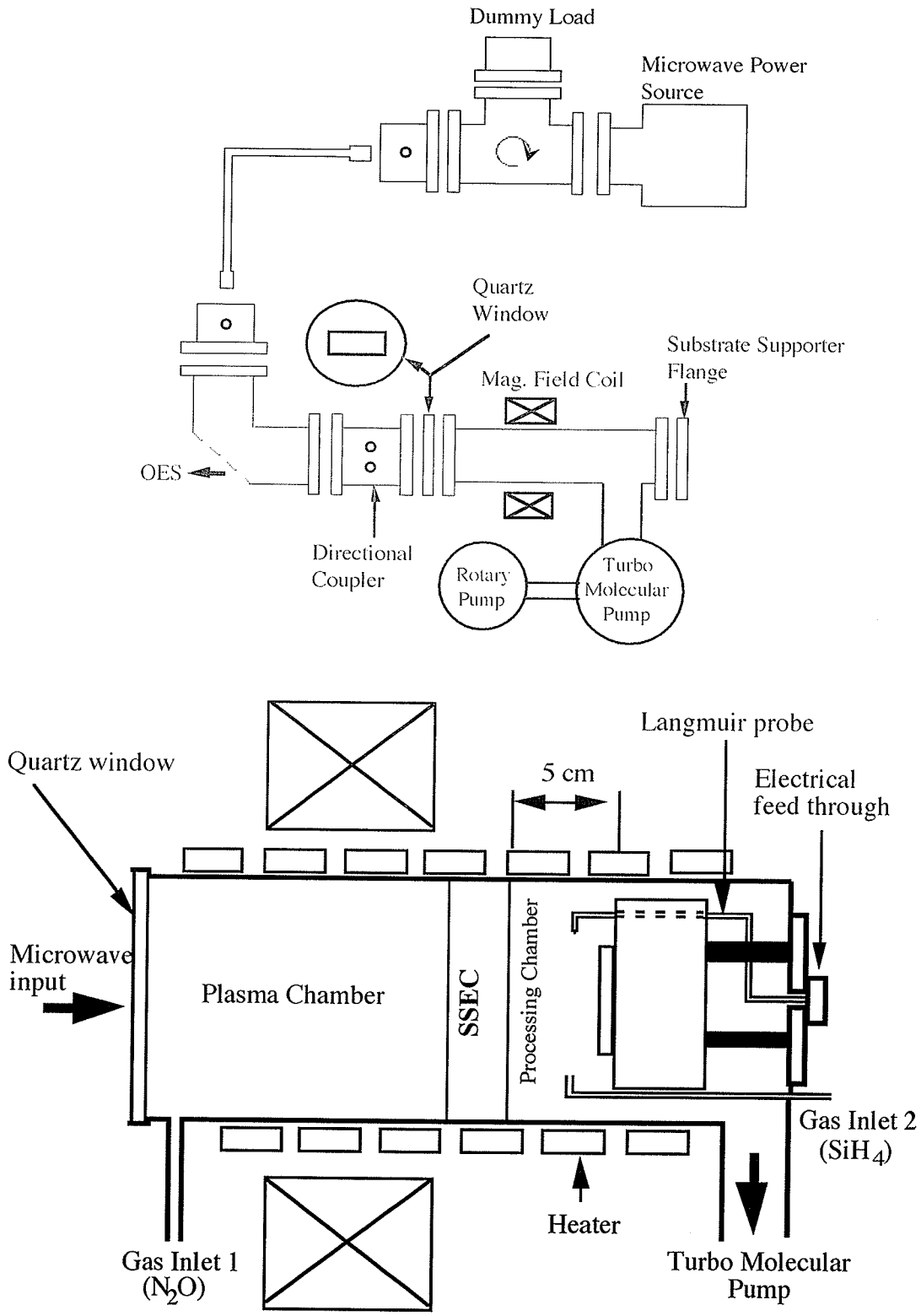

Figure 3.1. The ECR microwave CPPP system consisting the plasma chamber and the processing chamber separated by the SSEC apparatus.

preventing energetic electrons and ions from bombarding the surrounding structures and reducing the electron loss to the chamber walls and hence reducing the electromagnetic power required for sustaining the plasma. The plasma chamber contains a mixture of ions, electrons, neutral atoms and molecules, activated atoms and molecules, oxidizing species, as well as photons of various energies. The SSEC acts as a filter tending to filter out the charged particles and photons and also to block the diffusion of reactant gas from the processing chamber to the plasma chamber because with the SSEC the pressure in the plasma chamber can be maintained slightly higher than that in the processing chamber. Figure 3.2 illustrates the flow of various particles from the plasma chamber to the processing chamber via the SSEC. In the plasma the charged particles (ions and electrons) gain their energies from the input microwave power. Since the microwave is reflected from the SSEC, the charged particles after passing through the SSEC, will not regain their energies. The substrates are located close to the plasma region but separated by the SSEC, and the distance between the substrates and the SSEC is about 5 cm. One of the major functions of the SSEC is to remove the majority of charged particles. Without biasing, there is still a small number of charged particles reaching the processing chamber. If the amount is small, the electric fields created by a small ion sheath would also be small. As the mean free paths at the gas pressure used are much smaller than the distance between the substrate and the SSEC, multiple particle collisions would also occur. It is therefore likely that the kinetic energy of the remaining ions impinging on the growing films would be small. The activated species diffuse through the SSEC to the processing chamber, and most of them have the chance to arrive at the substrate

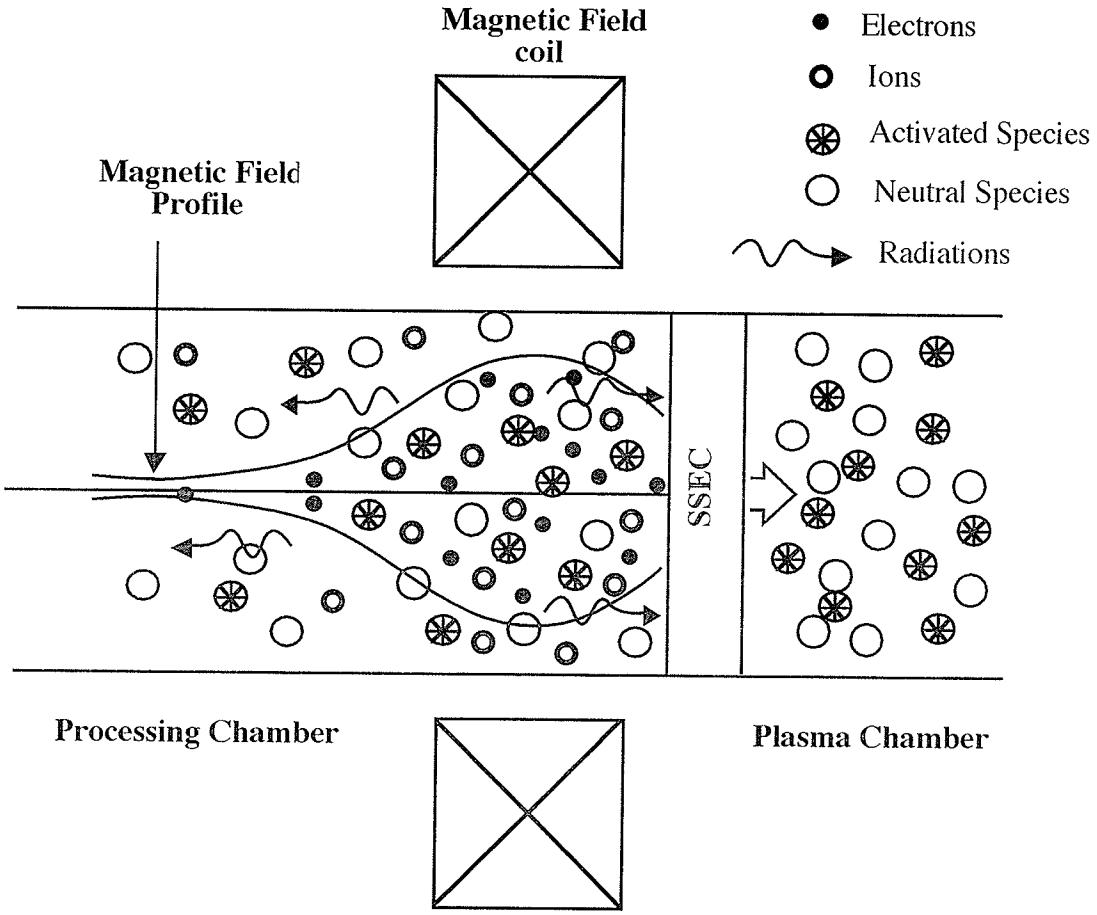

Figure 3.2. Illustrating the flow of particles between the plasma chamber and the processing chamber and the function of the SSEC.

surface to react with SiH_4 injected there to form solid SiO_2 films. This is why this system is called the CPPP system.

The SSEC is placed at about the edge of the coil generating magnetic fields or behind the plasma volume. The SSEC can be designed in several ways depending on what functions the SSEC is desired to optimize. Figure 3.3(a) shows the design of the SSEC used for this investigation. It is made of stainless steel and consists of two walls separated by a distance of 1 cm. The two walls have openings so that the gases, due to the slight pressure difference between the plasma and the processing chambers, can channel between the two walls. The gas species and other particles will collide with

one or both walls before they can enter the processing chamber. Thus, high energy particles will lose a large portion of their energy before entering the processing chamber. This SSEC also blocks completely the photon radiation directed to the substrate, and suppresses the charged particles (ions and electrons) from entering the processing chamber thus avoiding the impingement of both photons and charged particles on the substrates and the on-growing films, which is the major cause of the defects in the deposited films. The energy of the precursor species can be controlled by the walls in the SSEC. The energy tends to decrease as the number of walls is increased or as the separation between them is increased. The energy of precursor species can also be controlled by regulating the gas pressure difference between the plasma and the processing chambers. In most cases, the operating pressure is in the range of 10^{-3} to 10^{-1} torr, for which the gas flow is laminar. The main stream of the gas flow will be located primarily at the center of the chamber cross section [3.1], while the gas convection current which carries SiH_4 will flow along the chamber wall in the direction opposite to the gas main stream. The first wall of the SSEC creates a resistance to the main stream of the gas flow, thus making the pressure in the plasma chamber slightly higher than that in the processing chamber. The first wall of the SSEC also acts as a shield to block the flow of charged particles (ions and electrons). The second wall of the SSEC acts as a barrier to block the convection current and to change its direction so that it will mix with the incoming gas flow from the plasma chamber. Figure 3.3(b) shows that the individual wall can be isolated from the chamber wall so that it can be biased with a positive or negative dc voltage to eliminate completely electrons or ionic particles. It should be noted that a mask-screen grid

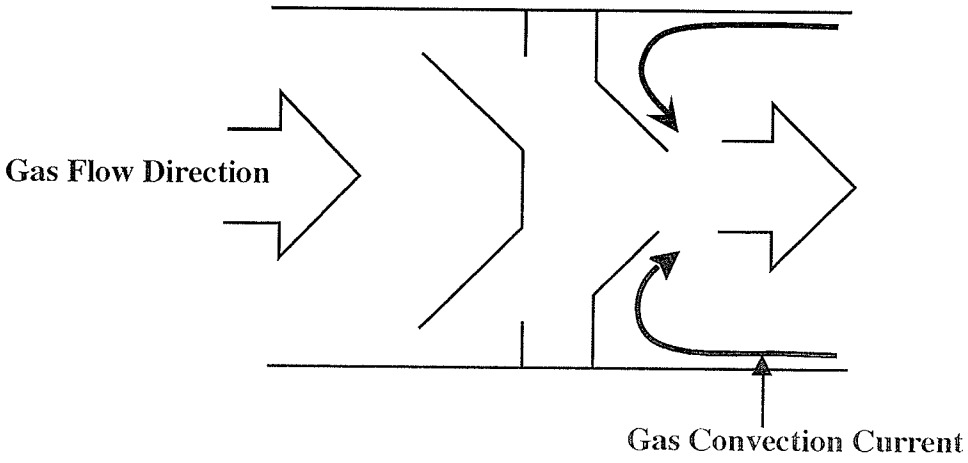

Figure 3.3(a). Schematic diagram of the SSEC without dc bias.

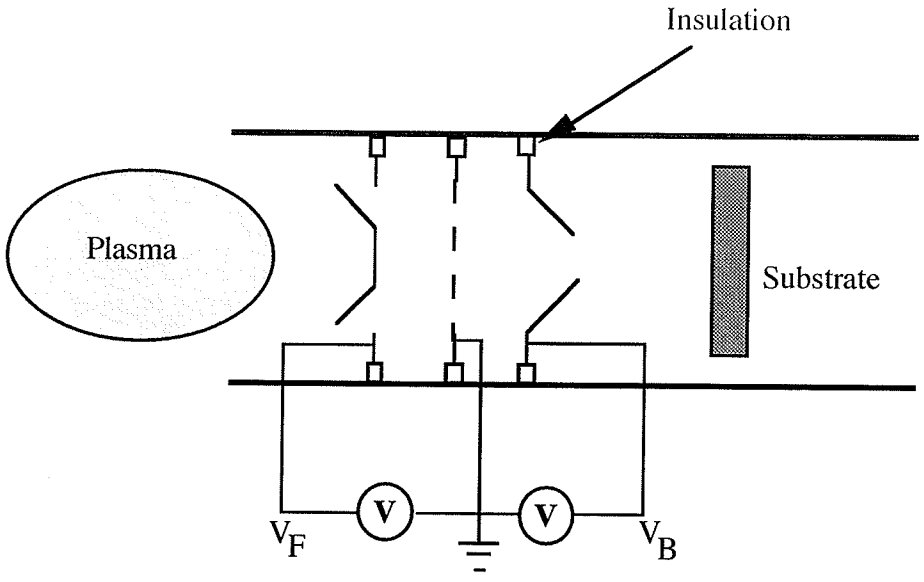

Figure 3.3(b). Schematic diagram of the SSEC with external dc biasing.

with tiny windows biased with suitable voltage may be capable of repelling one type of charged particles (e.g. negatively charged electrons) and accelerating the other type (e.g., positively charged ions). Such a grid has been used to control the impinging ion energy in microwave plasma etching [3.2]. In this case a negative bias is used. If two such grids, one biased with a negative voltage and the other biased with a positive voltage, are placed in parallel between the plasma and the processing chambers, this method can effectively suppress charged particles (ions and electrons) from bombarding the substrates and the on-growing films. However, the biased grid cannot block the photon radiation nor can it stop the diffusion of SiH_4 into the plasma chamber. The SSEC with dc biasing is shown in Fig. 3.3 in which the separation between any two of the three walls is 0.5 cm.

3.2. Optical emission spectra of the oxygen plasma

Figure 3.4 shows the schematic diagram of the experimental set-up for the measurements of the optical emission spectra (OES) of the plasmas. The optical emission from the plasma was sampled through a quartz window and a metal screen mesh. A telescope was used for focusing the emitting light onto one end of an optic fiber cable, which was then guided to a 25 μm slit of a Jarrell-Ash Monospec 27 spectrometer equipped with a 1200 grooves/mm grating and 1024 diode array EGG-PARC multi-channel analyzer. The OES were measured for three cases: (a) pure oxygen plasma, (b) oxygen + 5% of SiH_4 in Ar without the SSEC, and (c) oxygen + 5 % SiH_4 in Ar with the SSEC. O_2 gas was used rather than N_2O gas because the oxygen plasma OES is much simpler than the OES of N_2O for producing a clear picture about the reactant gas diffusion from the

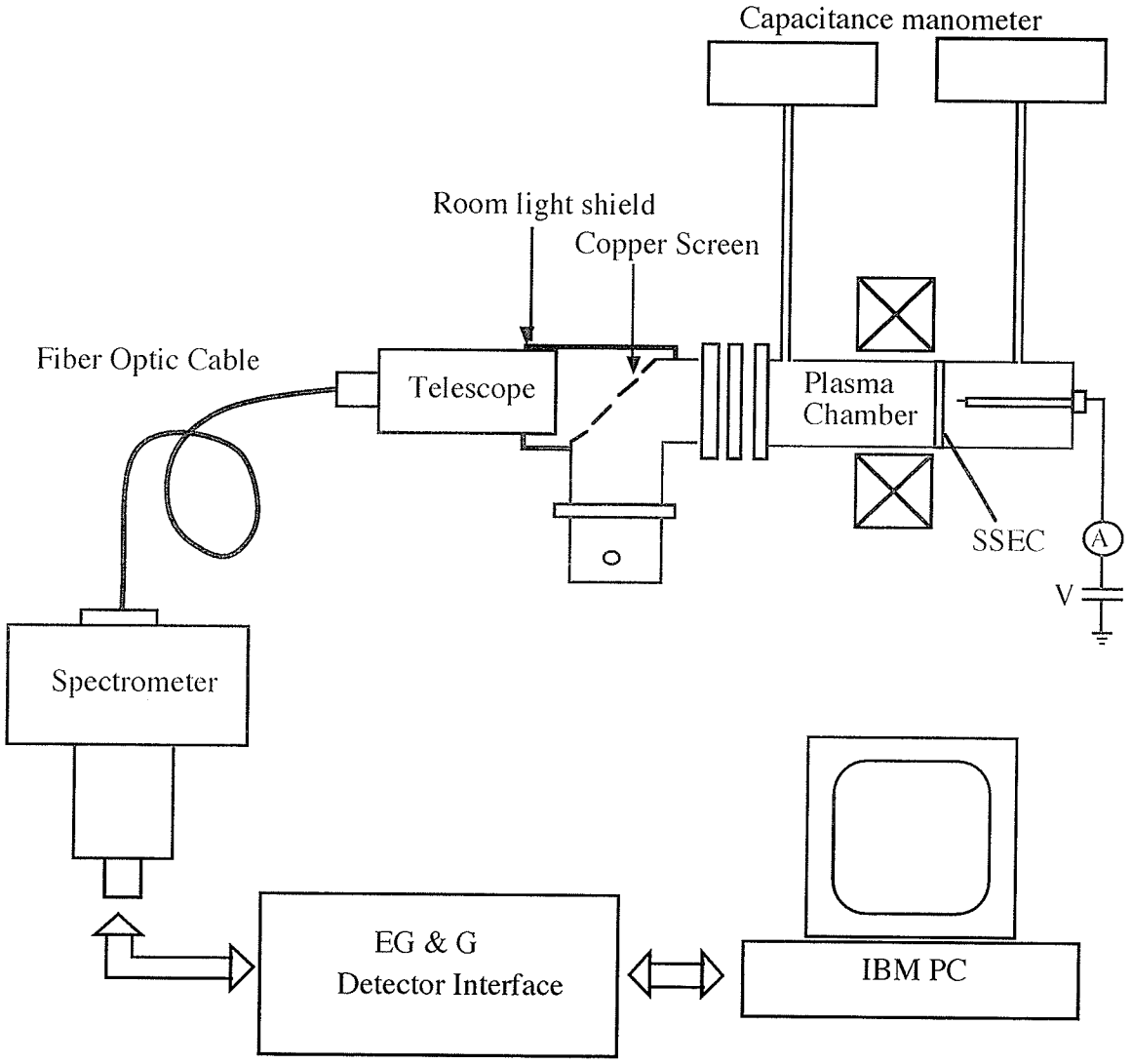

Figure 3.4. Experimental set up for optical emission spectra, Langmuir probe, and pressure measurements of the plasma in the plasma chamber.

processing chamber to the plasma chamber. The OES was taken at the pressure of 3 x 10^{-2} torr. This slightly higher pressure was chosen because it was desired to see the diffusion of SiH_4 by increasing the gas flow rate ratio to 20 sccm (O_2)/10 sccm (5% SiH_4 in Ar) instead of the ratio 10 sccm (N_2O)/1 sccm (5% SiH_4 in Ar), which was normally used for film deposition. The optical emission spectra for the plasma of the three cases are shown in Fig. 3.5. Figure 3.5(a) shows the standard O_2 plasma

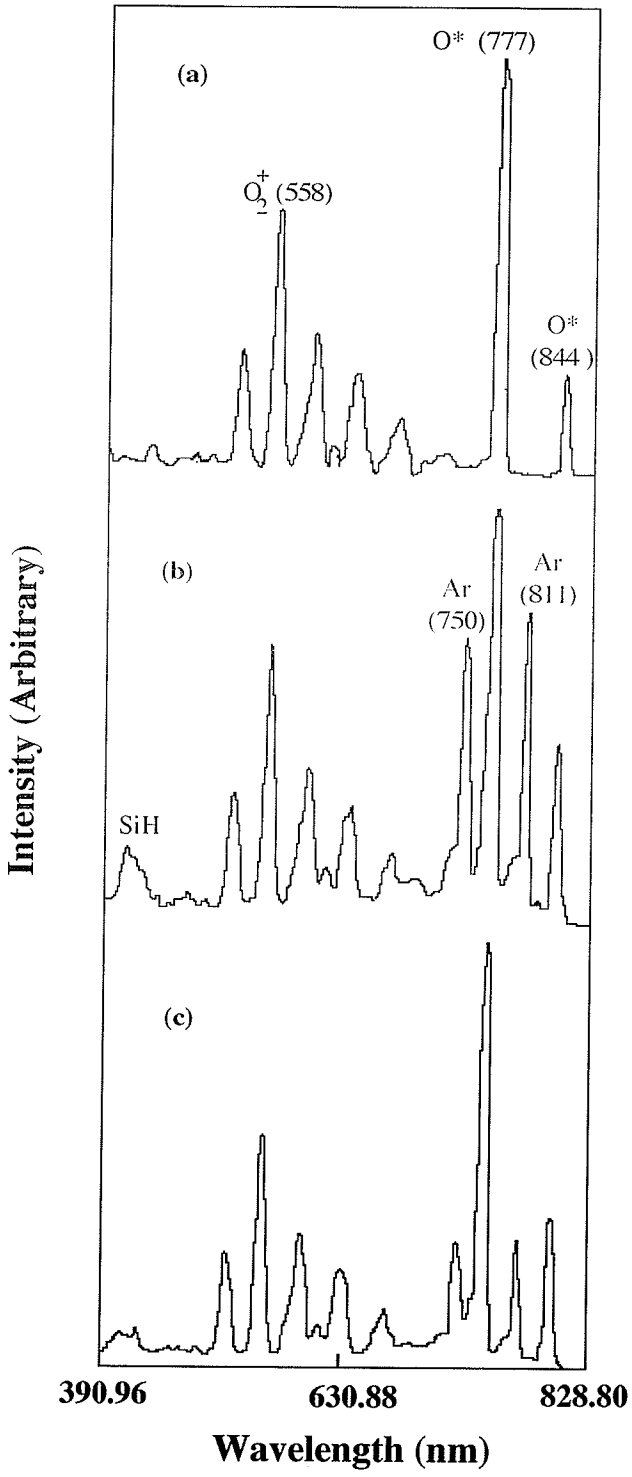

Figure 3.5. The optical emission spectra of the plasma for (a) pure oxygen gas, (b) pure oxygen gas + 5 % of SiH_4 in Ar for the case without the SSEC, and (c) pure oxygen gas + 5 % of SiH_4 in Ar for the case with the SSEC.

OES [3.3, 3.4]. When an Ar + 5 % SiH_4 gas is introduced into the processing chamber, the OES in the plasma chamber is changed. Figure 3.5(b) shows that new OES peaks at 421 nm due to the presence of SiH [3.5] and at 750 nm and 811 nm due to the presence of Ar [3.3, 3.6] appear for case (b) without the SSEC. This indicates that the reactant gas (Ar and SiH_4) diffuses into the plasma region. However, with the SSEC placed between the plasma and the processing chambers, the intensities of these new OES peaks are significantly reduced, as shown in Fig. 3.5(c). This experiment results show clearly that the SSEC inhibits the upstream diffusion of the reactant gas from the processing chamber to the plasma region.

Figure 3.6 shows the emission intensities for the O_2^+ at 558 nm, O* at 777 nm, and Ar at 811 nm versus the flow rate of the gas containing 5% of SiH_4 in Ar for the case without SSEC. The emission intensities of O_2^+ (558 nm) and O* (777 nm) decrease with increasing flow rate of the SiH_4 gas, indicating that the O_2^+ and O* species react spontaneously with SiH_X species. The chemical reactions can be described as follows:

(a) The reaction of SiH_X species with O_2^+:

$$SiH_x + O_2^+ + e^- \rightarrow SiO_2 + \frac{x}{2}H_2 \qquad x \le 4 \qquad (3.1)$$

$$SiH_x + O_2^+ + e^- \rightarrow SiH_{x-1}OH + O^* \qquad (3.2)$$

$$SiH_x + O_2^+ + e^- \rightarrow SiOH + H_{(x-1)}O \qquad x \le 2 \qquad (3.3)$$

$$SiH_4 + \frac{5}{2}O_2^+ + e^- \rightarrow 2SiOH + 3H_2O \qquad (3.4)$$

(b) The reactions of SiH_X species with O*:

$$SiH_x + O^* \rightarrow SiOH + \frac{x-1}{2}H_2 \qquad x \le 4 \qquad (3.5)$$

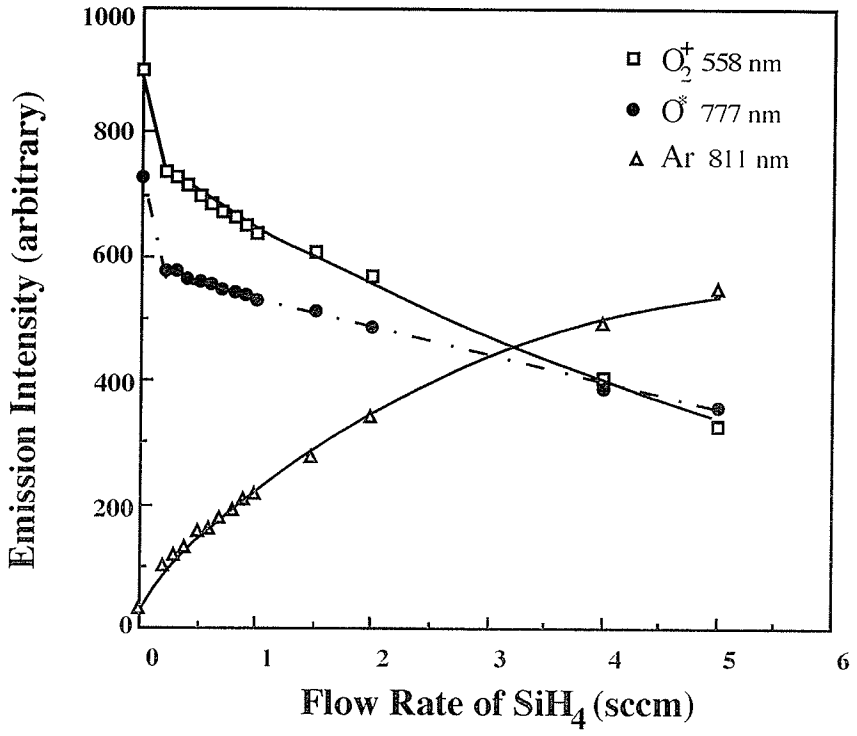

Figure 3.6. Emission intensities of O_2^+ (558 nm), O^* (777 nm), and Ar (811 nm) as functions of the flow rate of the gas consisting of 5 % SiH_4 in Ar for the case without the SSEC. Flow rate of oxygen: 10 sccm, gas pressure: 10-12 mtorr, and microwave absorption power under ECR condition: 6 watts.

$$SiH_x + O^* + e^- \rightarrow SiH_{x-1}OH \qquad (3.6)$$

Process (3.1) shows a direct gas phase reaction that may be responsible for the production of dust particles during the deposition processes. Processes (3.2) to (3.6) are gas phase reactions producing precursor species, which may be responsible for the deposition of SiO_2 films. However, the decrease of the emission intensity of O^* (777 nm), when SiH_4 was introduced into the chamber, may not be due to the reaction between O^* and SiH_X species (3.5-3.6), but may be due to the inhibition of the formation of O^* species such as:

$$O_2^+ + e^- \rightarrow 2O^* \qquad (3.7)$$

$$O_2 + e^- \rightarrow O + O \qquad (3.8)$$

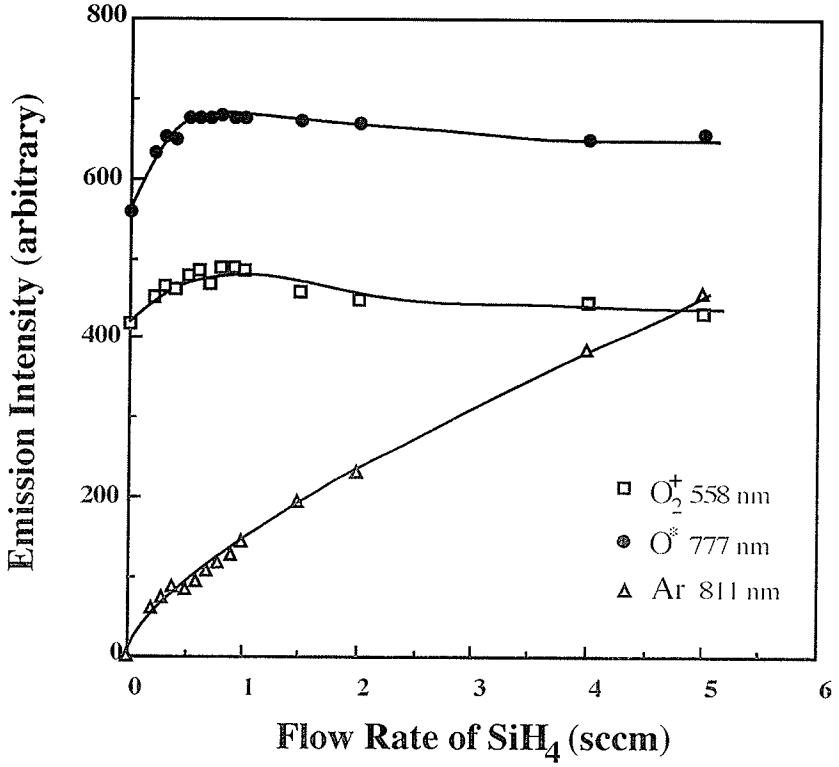

Figure 3.7. Emission intensity of O_2^+ (558 nm), O^* (777 nm), and Ar (811 nm) as functions of the flow rate of the gas consisting of 5 % SiH_4 in Ar for the case with the SSEC. Flow rate of oxygen: 10 sccm, gas pressure: 10-12 mtorr, and microwave absorption power under ECR condition: 6 watts.

$$O + e^- \rightarrow O^* \qquad (3.9)$$

Furthermore, process (3.8) may have a much higher reaction rate than process (3.7) [3.7]. If this is the case, then O_2 species may also react with the SiH_X species leading to the results shown in Fig. 3.6.

Figure 3.7 shows the emission intensities of O_2^+, O^*, and Ar as functions of the flow rate of SiH_4 for the CPPP system with the SSEC. In contrast to the case without the SSEC, the emission intensities of O_2^+ and O^* increase with increasing flow rate of SiH_4, indicating that there is no reaction between oxygen species and SiH_X taking place inside the plasma chamber. The increases of the emission intensity peaks are mainly caused

by the increase in pressure, which corresponds to the introduction of SiH_4 into the processing chamber. The emission intensity peaks at 558 nm and 777 nm decrease when the flow rate of 5 % SiH_4 in Ar is higher than 1 sccm. However, this decrease is only about 3 % of the total emission intensity, and it seems independent of the flow rate of SiH_4. This result again confirms that the SSEC can inhibit SiH_4 from diffusing toward the plasma chamber. Even though Ar appears in the plasma chamber, it is believed that the amount of SiH_4 leaking through is very small because the molecular weight of SiH_4 is much larger than that of Ar, and its concentration is only 5 % in the total gas mixture.

3.3. Langmuir probe measurements

Using a tungsten Langmuir probe biased at +10 V and -10 V and positioned at 5 cm from the edge of the magnetic field coil, the electron and the ion currents of the N_2O plasma have been measured using a Keithly 610 C electrometer with and without the SSEC. Figure 3.8 shows the electron and the ion currents as functions of the microwave power absorbed at a constant flow of 10 sccm of N_2O gas. The electron current is in general higher than the ion current irrespective of the SSEC as expected because electron mobility is larger than the ion mobility. However, both currents for the case with the SSEC are about three orders of magnitude smaller than those without the SSEC, indicating that the SSEC does effectively suppress the energetic charged particles from entering the processing chamber. Neither the electron nor the ion current vary with the microwave power absorbed, implying that the numbers of electrons and ions generated in the plasma have reached the saturation values at the ECR condition. The electron and the ion currents were also measured as

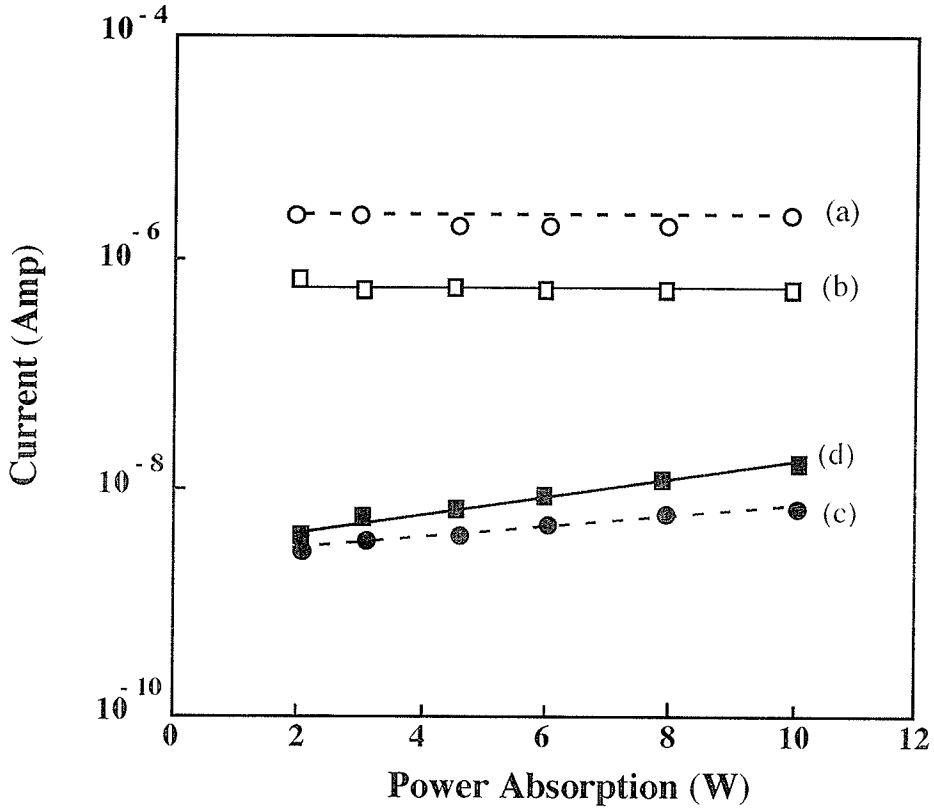

Figure 3.8. The electron and the ion currents of the N_2O plasma at a constant flow rate of 10 sccm as functions of microwave power absorbed. (a) the electron current without the SSEC, (b) the ion current without the SSEC, (c) the electron current with the SSEC, and (d) the ion current with the SSEC.

functions of gas pressure. The results are shown in Fig. 3.9. Again, both currents for the case with the SSEC are about three orders of magnitude smaller than those without the SSEC. The decrease of the current with increasing pressure can be explained as due to the decrease in mean free path as the pressure is increased, thus increasing the collision among particles and hence reducing the energies of both electrons and ions. It should be noted that the electrons and ions are not completely shielded by one unit of the SSEC. In the SSEC, the two walls are about 1 cm apart and both walls are arranged in such a way that there is no straight-path opening which would allow particles to move directly from the plasma chamber to

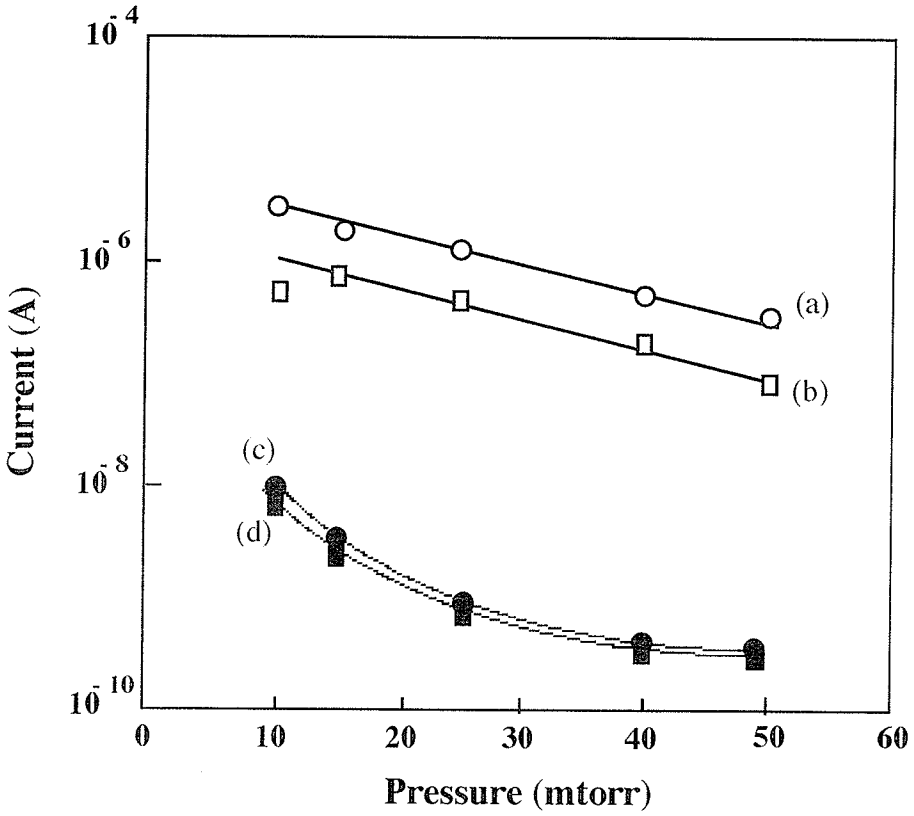

Figure 3.9. The electron and ion currents of the N_2O plasma at a constant microwave power of 6 W as functions of gas pressure (a) the electron current without the SSEC, (b) the ion current without the SSEC, (c) the electron current with the SSEC, and (d) the ion current with the SSEC.

the processing chamber, or vice versa. One unit of the SSEC consists of two walls, so that any particle has to collide at least once with the wall because most particles are moving in parallel with the chamber axis due to the magnetic field confinement. Electrons and ions may lose some energy by such a collision with the wall. Only those with higher energy may still have sufficient energy after losing some due to collision to proceed toward the processing chamber. In general, the average energy of the electrons and ions in an ECR microwave plasma is within the range of 3-10 eV [3.8]. However, in the case without the SSEC there must be a large number of high energy electrons and ions (>10 eV) entering the processing chamber

and thus causing bombardment damage to the substrates and the on-growing films. The major function of the SSEC placed between the plasma and the processing chambers is to remove the majority of charged particles (electrons and ions) before they have a chance to enter the processing chamber. This function is clearly demonstrated in Figs. 3.8 and 3.9. As a result of this action, the concentration of the remaining charged particles in the processing chamber is small and hence the electric field near the substrate surface created by the ion sheath is small. Thus, the kinetic energy of the remaining charged particles impinging on the substrates and the on-growing films is likely small and may not cause any significant damage. This is also why the properties of the SiO_2 deposited with the SSEC approach those of high quality thermally grown SiO_2 films. It should be noted that the activated oxygen species have to flow to the processing chamber for chemical reaction with the reactant gas to form solid films. Like the charged particles, the amount of these species which can enter the processing chamber is also considerably reduced because of the SSEC. For this reason, it is desirable to limit the number of the SSEC walls to only two and with a suitable biasing as shown in Fig. 3.3(b) in order to effectively suppress the flows of electrons and ions, and in the mean time, not to seriously hinder the flow of the activated oxygen species.

The SSEC also creates a pressure difference between the plasma and the processing chamber. Figure 3.10 shows the ratio of the pressure in the plasma chamber (P_1) to that in the processing chamber (P_2) as a function of the pressure in the plasma chamber. The SSEC makes the pressure in the plasma chamber about twice as large as that in the processing chamber for

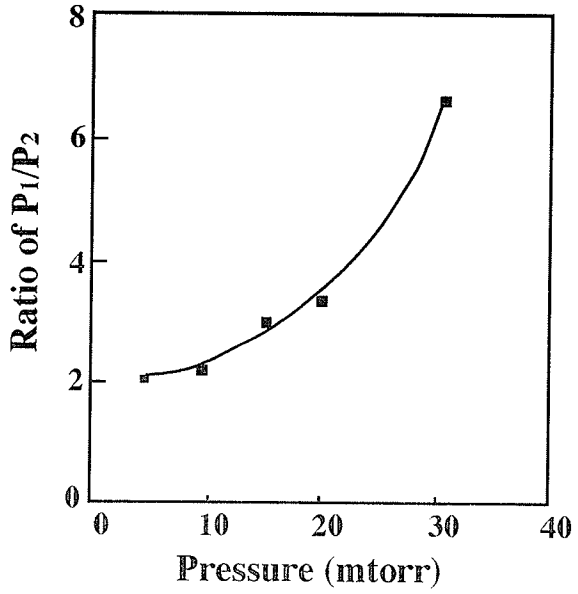

Figure 3.10. The ratio of the gas pressure in the plasma chamber (P_1) to that in the processing chamber (P_2) as a function of gas pressure in the plasma chamber (by varying the pumping speed) for the case with the SSEC. The flow rate of N_2O: 10 sccm, the flow rate of N_2: 1 sccm.

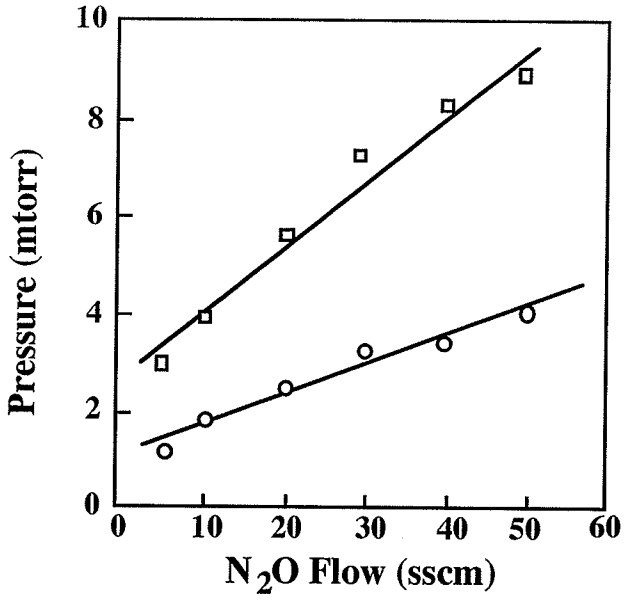

Figure 3.11. The difference between the gas pressure in the plasma chamber (P_1) and that in the processing chamber (P_2) as a function of the flow rate of N_2O gas (with a constant pumping speed) for the system (a) without the SSEC and (b) with the SSEC.

a pressure in the plasma chamber of 10^{-3} torr which is normally used for the deposition of SiO_2 films. This pressure difference makes upstream diffusion of the reactant gas (such as SiH_4) difficult from the processing chamber to the plasma chamber. An experiment was also performed to measure the pressure difference (P_1-P_2) as a function of gas flow rate of N_2O gas injected via the gas inlet 1 to the plasma chamber with the flow rate of N_2 gas injected via gas inlet 2 to the processing chamber kept constant at 1 sccm. The results are shown in Fig. 3.11. As expected, the pressure difference increases with increasing flow rate, and in general this pressure difference is much higher for the system with the SSEC than without. Again, this experiment further demonstrates that the SSEC acts as the pressure regulator and that it not only suppresses upstream diffusion but also blocks the convection current flow of the gas from the processing chamber to the plasma chamber.

3.4. Comparison of the properties of SiO_2 films deposited with and without the SSEC

SiO_2 films were deposited on n-type, <100> oriented, 1-2 Ω-cm silicon wafer substrates using the microwave ECR plasma system described above with and without the SSEC. The film samples deposited without the SSEC are labeled group A samples and those with the SSEC are labeled group B samples. For FTIR measurements, the wafers were thinned by a HF/HNO_3 solution to increase the IR transmission prior to film deposition. Both group A and group B films were deposited under the same plasma conditions with the following parameters: gas mixture of 5 % SiH_4 in Ar at a flow rate of 1 sccm and 100 % N_2O at a flow rate of 10 sccm, gas pressure of $16x10^{-3}$ torr in the plasma chamber for the case without the

SSEC, gas pressures of $22x10^{-3}$ torr in the plasma chamber and $16x10^{-3}$ torr in the processing chamber for the case with the SSEC, microwave absorption power of 4 watts, magnetic field of 875 Gauss for the ECR condition, and deposition temperature of 300 °C.

It is interesting to note that for the system with the SSEC, the deposition rate of SiO_2 films increases with increasing deposition temperature and gradually becomes saturated for deposition temperatures higher than 200 °C as shown in Fig. 3.12. In contrast, for the case without the SSEC, the deposition rate decreases with increasing deposition temperature. These results indicate that the films deposited with the SSEC follow a heterogeneous surface rate-limited reaction which has an Arhenius type temperature dependence. The Arrehenius plot of the deposition rate versus 1/T yields an activation energy of 0.035 eV. For the case without the SSEC, the deposition rate follows a gas phase mass-limited reaction. The deposition rate decrease with increasing temperature is due to the densification of the films at higher deposition temperatures. For the case with the SSEC, the rate of densification is much smaller than the rate of surface reaction, so that the deposition rate increases with increasing deposition temperature.

The refractive index for each film was also measured using a Gartner ellipsometer with a helium-neon laser light of wavelength of 6328 Å. SiO_2 films with thicknesses of 1200-1400 Å were used for this investigation because this thickness range corresponds to approximately half an ellipsometric cycle and is supposed to yield more accurate ellipsometric results. The film thickness was also measured by ellipsometry and checked by capacitance measurement. Figure 3.13 shows

the refractive index of SiO_2 films as a function of deposition temperature. For the films deposited with the SSEC, the refractive index of SiO_2 is about 1.38 at the deposition temperature of about 30 °C. It increases rapidly as the temperature is increased and become saturated at temperatures higher than 200 °C. At these temperatures the refractive index is about 1.456 indicating that the films may have become denser as the deposition temperature increases. For the case with the SSEC, the refractive index increases from 1.41 at 30 °C to 1.456 at the deposition temperature of 300 °C implying that the film also becomes denser as the deposition temperature is increased.

The basic parameters governing the film deposition rate are the rate of mass transport of reactants to the substrate surface and the rate of chemical reaction at the substrate surface. The reaction rate depends mainly on the concentration of the reactants and deposition temperature. For the case with the SSEC, the reactants are activated oxygen species and SiH_4, and the mass transport of these reactants can be considered to be constant because both the gas pressure and the gas flow rate are kept constant during deposition. The saturation of the deposition rate at deposition temperatures higher than 250 °C implies that the reaction in the deposition process is heterogeneous and is surface-rate limited. The surface reaction is due to the reaction of SiH_4 adsorbed on the substrate surface and the approaching activated oxygen species generated from the N_2O plasma. The reaction between SiH_4 and activated oxygen species is an exothermic type of reaction [3.9]; hence, the reaction itself may contribute part of its energy to promote the reaction. The deposition rate for this particular set of deposition parameters is low when compared with those using other

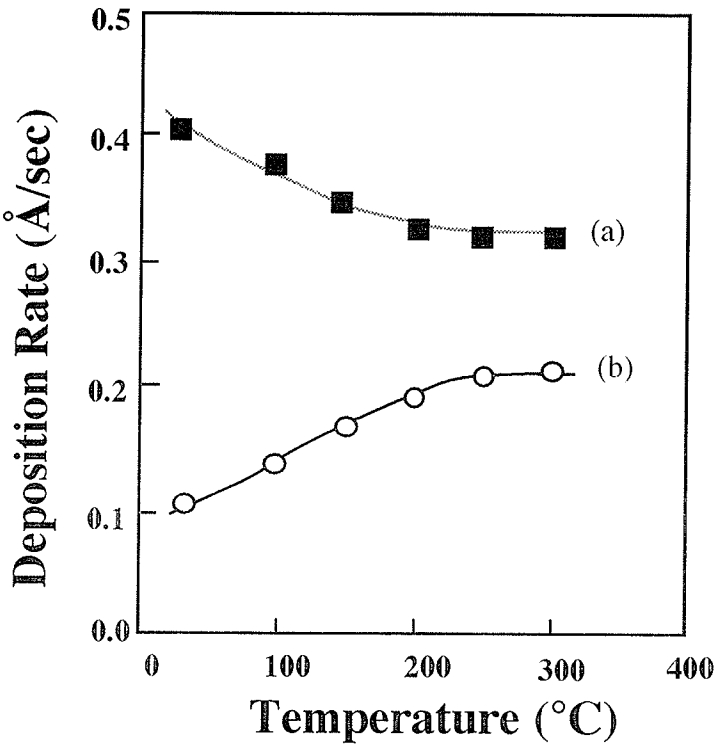

Figure 3.12. The deposition rate of SiO_2 films as a function of deposition temperature for the films deposited (a) without the SSEC and (b) with the SSEC.

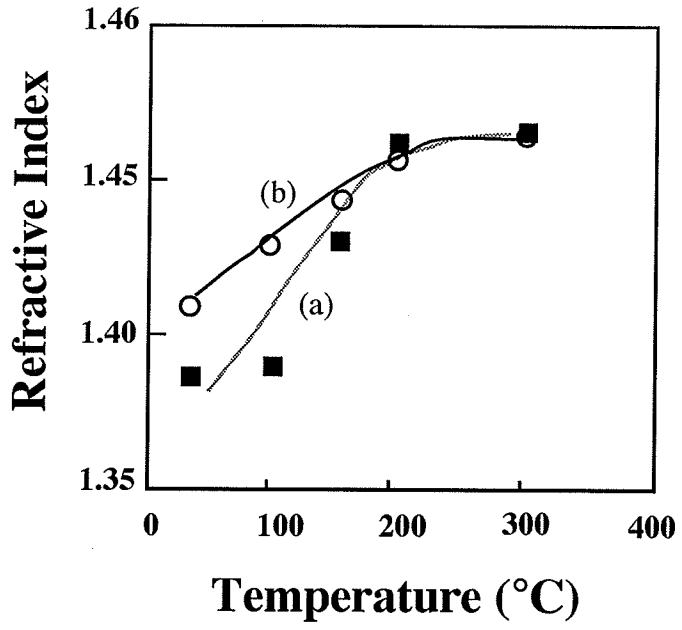

Figure 3.13. The refractive index of SiO_2 films as a function of deposition temperature for the films deposited (a) without the SSEC and (b) with the SSEC.

PECVD processes [3.10, 3.11]. However, several investigators [3.12, 3.13] have reported that the quality of the films is directly related to the deposition rate. SiO_2 films deposited at slow rates of the order of those in this present investigation usually exhibit good electronic properties. From a practical point of view, the slow deposition rate, on the other hand, provides an easy control of film thickness, particularly for very thin gate oxides (100-200 Å in thickness) for VLSI. It should be noted that the low activation energy of 0.035 eV is the same as that reported by Adam et al [3.14], but is about 10 times smaller than that for the SiO_2 films deposited by a LPCVD process [3.15], which is about 0.4 eV. Although this activation energy is small, it still plays an important role in the change of the film composition. In other words, the activation energy is related to the energy required for the arrangement of the activated atoms to form SiO_2 species and for the formation of a stable SiO_2 film structure. The evidence of this action is that the SiO_2 films change from a silicon rich composition to a more stoichiometric composition as the deposition temperature is changed from 25 °C to 300 °C.

Figure 3.14 shows the infrared (IR) spectra of the SiO_2 films measured with a Bomem 1000 FTIR spectrometer. The Si-O stretching mode absorption peak occurs approximately at 1070 cm^{-1} for (a) the films deposited without the SSEC and (b) the films deposited with the SSEC and at 1080 cm^{-1} for (c) the films fabricated by thermal oxidation at 1100°C. The full widths at half maximum (FWHM) of these peaks are 85 cm^{-1}, 75 cm^{-1} and 70 cm^{-1} for (a), (b), and (c), respectively. A more careful observation reveals that the peak in (a) is much more asymmetric than that in (b) and (c), exhibiting a high frequency shoulder in (a) larger than that

in (b) and (c). The ratios of the absorbance at the shoulder edge to the absorbance peak (R_{IR}) are 0.4, 0.2, and 0. 13 for (a), (b), and (c), respectively. It can be seen clearly that the IR spectrum of the SiO_2 films fabricated with the SSEC approaches that of the high quality thermal oxides.

For electrical measurements, aluminum electrodes 1000 Å in thickness and 5 x 10^{-3} cm^2 in area each were vacuum deposited on the SiO_2 surface through a shadow mask to form MOS capacitors. The SiO_2 layer was in the range of 200-250 Å. The I-V characteristics were measured with the gate biased at positive polarity (accumulation mode) using a current ramp technique. The high frequency (1 MHz) and the quasi-static C-V characteristics were measured for the devices after being subjected to post metalization annealing (PMA) in a forming gas (10 % of H_2 in N_2) at 400 °C for 30 min using a linear voltage ramp in conjunction with a Boonton capacitance meter and Keithly 604 electrometer. The ramp rates used for I-V and C-V measurements were 1 V/s and 50 mV/s, respectively.

The MOS capacitors were first subjected to a low field test (1 MV/cm) to screen out those which were short circuited. The devices which withstood the low field test were then subjected to a ramp voltage stressing with the ramp rate of 0.5 MV/cm-sec until the occurrence of destructive breakdown. The histograms of typical breakdown distributions for films deposited without the SSEC (group A) and films deposited with the SSEC (group B) are shown in Fig. 3.15. For group A samples, about 40 % of the devices could not sustain the low field test at 1 MV/cm, and the average breakdown strength was about 7 MV/cm. For group B samples only 12 % of the devices failed in the low field test, and the average breakdown

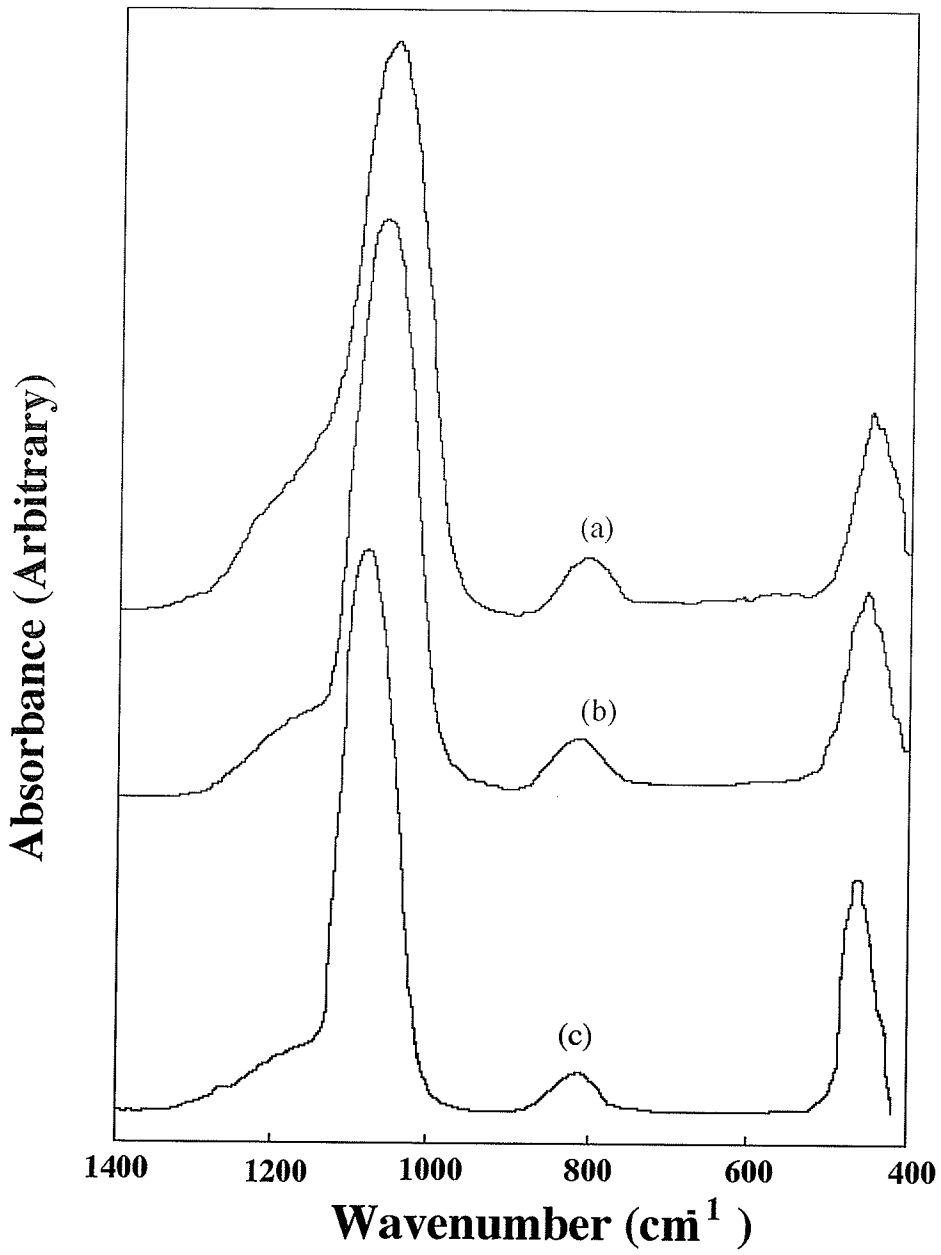

Figure 3.14. The infrared absorption spectra of SiO_2 films (a) deposited without the SSEC, (b) deposited with the SSEC, and (c) fabricated by thermal oxidation at 1100°C.

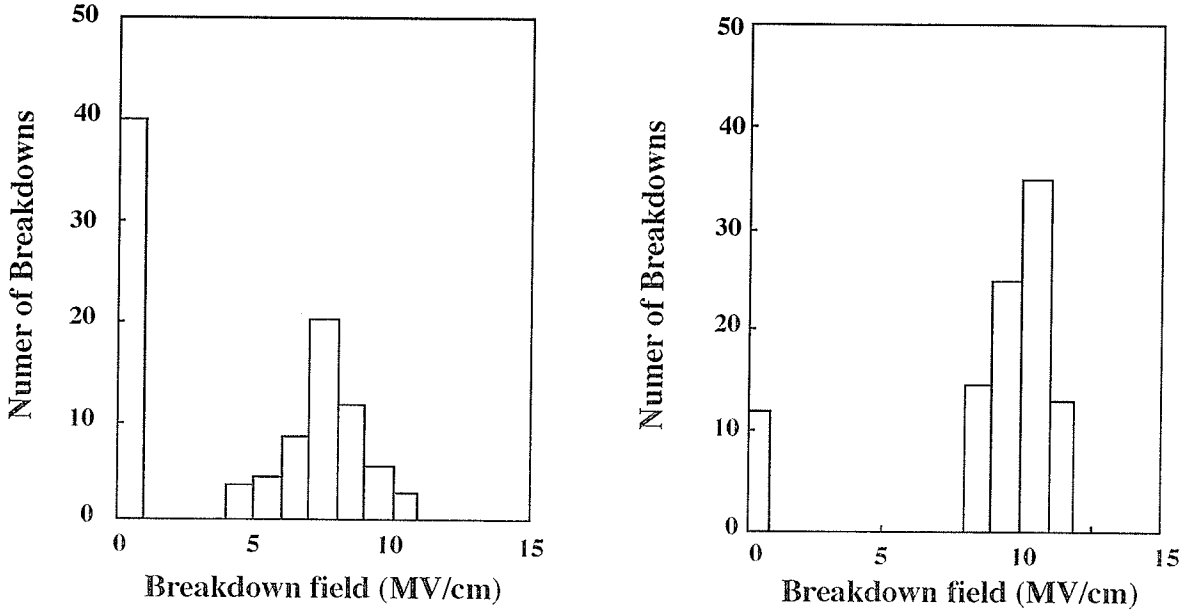

Figure 3.15. The histograms of typical breakdown distributions. (A) MOS capacitors with SiO_2 deposited without the SSEC, and (B) MOS capacitors with SiO_2 deposited with the SSEC.

strength was about 10 MV/cm. Furthermore, the spread of the breakdown distribution for group A samples is much wider than that for group B samples. The destructive breakdown may be characterized into three modes: (i) for the breakdown strengths (E_{BD}) ≤ 1 MV/cm, the breakdown may be caused by dust particles and pin holes in SiO_2 films; (ii) for 1 MV/cm ≤ E_{BD} ≤ 9 MV/cm, the breakdown may be associated with weak spots in SiO_2 films, and (iii) for E_{BD} ≥ 9 MV/cm the breakdown may be considered to be intrinsic. Group A samples contains more dust particles and pin holes as well as more weak spots as compared with group B samples. The difference between these two group samples may be attributed to the difference in their film growth processes. Group A samples were deposited without using the SSEC, the SiH_4 was in direct contact with the plasma formed by N_2O, which produces species due to

discharge. These species underwent heterogeneous gas phase reaction to form micro-dust particles which then landed on the substrate surfaces and on-growing film surfaces. These harmful particles, depending on their size, might be embedded inside the film to form weak spots. For the case of group B samples, the SiH_4 was kept away from the plasma region by the SSEC, thus minimizing the chance for the formation of micro-dust particles. The current-voltage (I-V) characteristics of SiO_2 films deposited without (A) and with (B) the SSEC are shown in Fig. 3.16. The I-V characteristics for (B) samples are similar to those for the high quality thermal oxides. At fields higher than 5 MV/cm, the current is mainly due to Fowler-Norheim (FN) tunneling injection [3.16] with the final breakdown occurring at the field range of 8-11 MV/cm. No self-healing phenomenon was observed in (B) samples prior to the final breakdown. However, self-healing phenomenon was observed in (A) samples when the applied fields were higher than 2 MV/cm. This indicates that (A) samples have weak spots so that the breakdown point could be self-healed during breakdown at low fields due to the melting of the aluminum electrode. During the growth of (A) samples, the substrates and the on-growing films were exposed to the plasma, and therefore subjected to the bombardment of energetic particles such as ions, electrons, and photons. The ultraviolet radiation created by the plasma alone could break weak Si-O bonds [3.17], which would, in turn, create electron traps. These traps will then capture electrons coming from the plasma, and as the electron capturing process continues throughout the deposition period, layer by layer of negative charges will build up. The threshold field for the FN tunneling injection is higher for the SiO_2 films deposited without the SSEC than that for the SiO_2 films deposited with the SSEC as shown in Fig. 3.16 indicating that

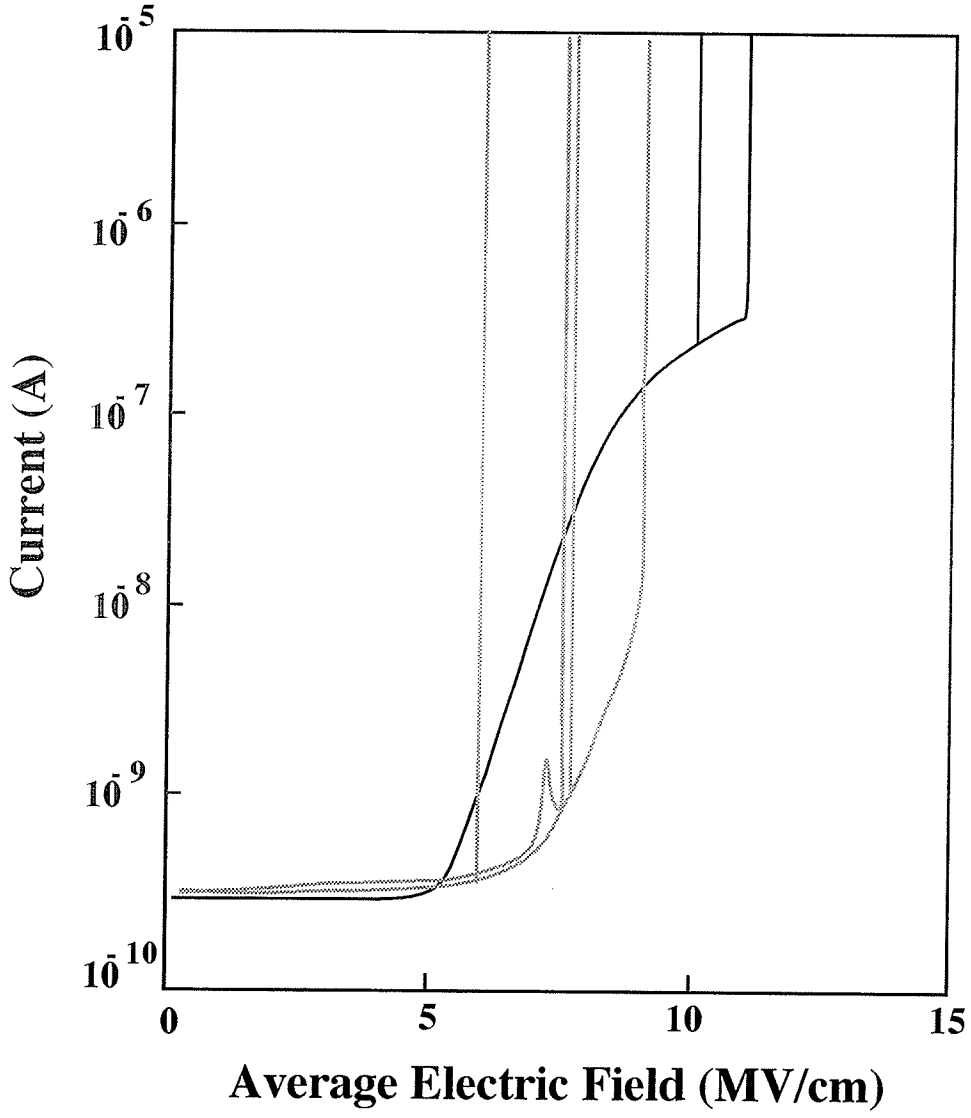

Figure 3.16. The I-V characteristics for SiO_2 films deposited without the SSEC (dotted) and with the SSEC (solid).

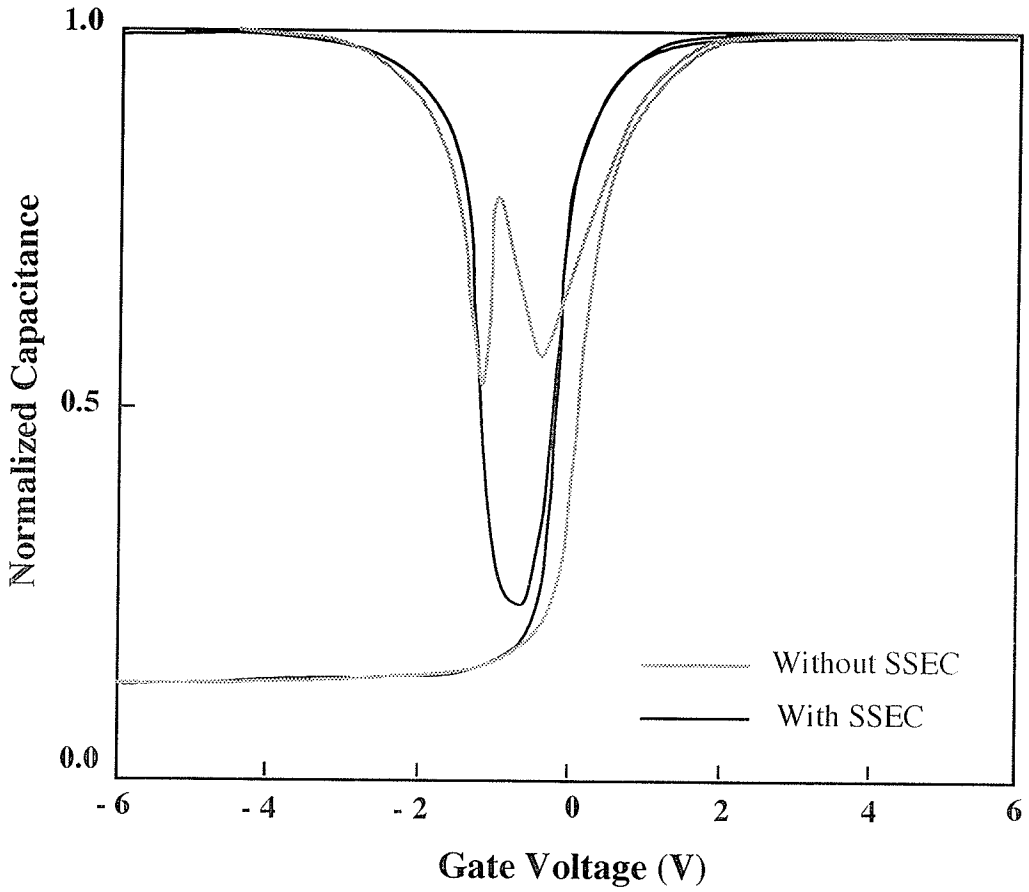

Figure 3.17. The quasi-static and high frequency capacitance-voltage characteristics for SiO_2 films deposited without and with SSEC.

the concentration of bulk trapped charge is higher for the former case than the latter. This phenomenon is similar to the shift of the I-V curve towards higher fields due to the build-up of trapped electrons injected from the negatively biased silicon in the MOS capacitor. The breakdown strength of the SiO_2 films deposited without the SSEC spreads unevenly in the range 5-9 MV/cm. The early breakdown at lower fields may be associated with the micro-dust particles incorporated in the bulk of the films coupled with the build-up of negatively charge layers. The former has been observed under helium laser light reflection and the latter is consistent with the observation

of Holland and Hu [3.18] who have reported that the injection of positive charge carriers into SiO_2 results in an increase of the breakdown strength.

The high frequency (1 MHz) and the quasi-static capacitance-voltage (C-V) characteristics for SiO_2 films deposited without and with the SSEC are shown in Fig. 3.17. It can be seen that both the high frequency and the quasi-static C-V curves for the SiO_2 films deposited with the SSEC are very similar to those of high-quality thermal oxides with an interface trap density (D_{it}) of $5x10^{11}$ eV^{-1} cm^{-2} after PMA. However, for the SiO_2 films deposited without the SSEC, the high-frequency C-V characteristic is shifted toward the positive bias voltage indicating that the film contains a high concentration of negatively trapped charge. Also, the quasi-static C-V characteristic is distorted as shown in Fig. 3.17 indicating that the film has a high interface trap density. The value of D_{it} after PMA for this case has been estimated to be about 10^{13} eV^{-1} cm^{-2}.

References for chapter 3

[3.1] J. M. Coulson and J. F. Richardson, "*Chemical Engineering*," Pregamon, New York, 1977, p. 52.

[3.2] K. Suzuki, S. Okudaira, S. Nishimatsu, K. Usami, and I. Kanomata, "*Microwave Plasma Etching of Si With CF_4 and SF_6 Gas*," J. Electrochem. Soc., **129**, 2766(1982).

[3.3] G. N. Parsons, D. V. Tsu, C. Wang, and G. Lucovsky, "*Precursor for the Deposition of Amorphous Silicon-Hydrogen Alloys by Remote Plasma Enhanced Chemical Vapor Deposition*," J. Vac. Sci. Technol. **A7**, 1124 (1989).

[3.4] R. E. Walkup, K. L., Saenger, and S. S. Selwyn, "*Studies of Atomic Oxygen in O_2 + CF_4 rf Discharges by Two-Photon-Laser-*

Induced Fluorescence and Optical Emission Spectroscopy," J. Chem. Phys., **84**, 2668(1986).

[3.5] T. Sato and T. Goto, "*Emission Cross Sections of Excited Fragments Produced by 0-100 eV Electron Impact on SiH_4: Application of the 'He Standard'*," Jpn. J. Appl. Phys., **25**, 937(1986).

[3.6] J. S. Kckillop, J. C. Forster, and W. M. Holber, "J. Vac. Sci. Technol., A 7, 908, (1989).

[3.7] E. J. H. Collart, J. A. G. Baggerman, and R. J. Visser, "*Excitation Mechanisms of Oxygen Atoms in a Low Pressure O_2 Radio-Frequency Plasma*," J. Appl. Phys., **70**, 5278(1991).

[3.8] K. Shirai, T. Iizuka, and S. Gonda, "*Electrical Probe Measurements in an ECR Plasma CVD Aparatus*," Jpn. J. Appl. Phys., **28**, 897(1989).

[3.9] S. Samukawa, "*Damage Caused by Stored Charge During ECR Plasma Etching*," Jpn. J. Appl. Phys., **29**, 980 (1990).

[3.10] T. V. Herak, T. T. Chau, D. J. Thomson, S. R. Mejia, D. A. Buchanan, and K. C. Kao, "*Low Temperature Depostion of Silicon Dioxide Films from Electron Cyclotron Resonant Microwave Plasma*," J. Appl. Phys., **65**, 2457 (1989).

[3.11] S. Matsuo and M. Kiuchi,"*Low Temperature Chemical Vapor Deposition Method Utilizing an Electron Cyclotron Resonance Plasma*," Jpn. J. Appl. Phys., **22**, L210(1983).

[3.12] L. G. Meiners, "*Indirect Plasma Deposition of Silicon Dioxide*," J. Vac. Sci. Technol., **21**, 675(1982).

[3.13] P. D. Richard, R. J. Markunas, G. Lucovsky, G.G Fountain, A. N Mansour, and D. V. Tsu., "*Remote Plasma Enhanced CVD*

Deposition of Silicon Nitride and Oxide for Gate Insulators in (In, Ga)As FET Devices," J. Vac. Sci. Technol., **A3**, 867(1985).

[3.14] A. C. Adam, F. B. Alexander, C. D. Capio, and T. E. Smith, "*Characterization of Plasma Deposited Silicon Dioxide*," J. Electrochem. Soc., **128**, 1545(1981).

[3.15] R. Iyer and D. L. Lile, "*Kinetics of Low Pressure CVD Growth of SiO_2 on InP and Si*," J. Electrochem. Soc., **135**, 691 (1988).

[3.16] B. K. Ip, K. C. Kao, and D. J. Thomson, "*Charges and Defects in SiO_2 Films deposited by Plasma Enhanced Chemical Vapor Deposition at Low Te,peratures*," Solid State Electron., **34**, 123(1991).

[3.17] H. S. Witham and P. M. Lenahan, "*Nature of Deep Hole Trap in MOS Oxides*," IEEE Trans. Nucl. Sci., **34**, 1147 (1987).

[3.18] S. Holland and C. Hu, "*Corelation Between Breakdown and Process-Induced Positive Charge Trapping in Thin Thermal SiO_2*," J. Electrochem. Soc., **133**, 1705(1986).

4

Effects of Deposition Parameters on Properties of SiO_2/Si systems

In this chapter, some results and discussion about the effects of deposition parameters on properties of SiO_2/Si systems with the SiO_2 films fabricated by the ECR microwave plasma processing system with the SSEC apparatus will be described. The deposition parameters include the gas flow rate, the gas pressure, the substrate temperature, and the dc bias of the SSEC. The effects of the thickness of the SiO_2 films have also been systematically studied and are also included in this chapter.

4.1. The effects of the gas flow rate

As mentioned previously, the gas flow rates, the pressure, and the substrate temperatures are important parameters that depict control of the film deposition rate and the film composition. It has been reported that the deposition rate of SiO_2 films fabricated by PECVD has to be low in order to produce high quality SiO_2 films [4.1-4.3]. In practice, the low deposition rate is generally acceptable for gate oxide fabrication because this enables precise control of the film thickness. However, for other applications such as dielectric inter-layers for metal routing, thicker SiO_2 films (>1000 Å) are required. Thus, the trade-off between film quality and film deposition rate should be optimized for given applications. Figure 4.1 shows the deposition rate and the refractive index of SiO_2 films as functions of the gas flow ratio (N_2O/SiH_4). The deposition rate is about 65

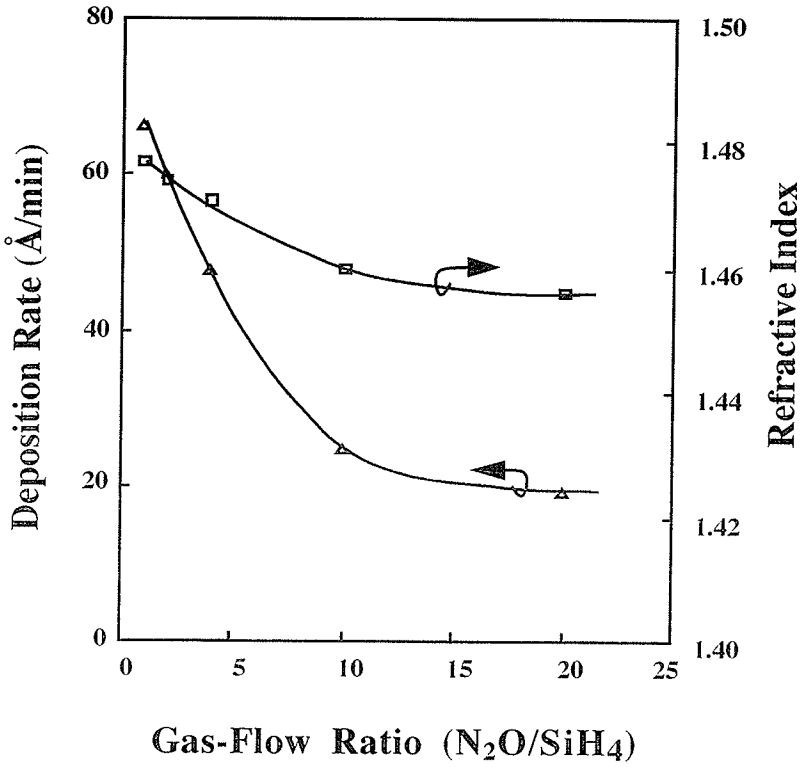

Figure 4.1. Deposition rate and refractive index of SiO_2 films as functions of gas-flow ratio at a constant pressure of 27 mtorr.

Å/min at a gas flow ratio of 1 (6.5:6.5 of N_2O:SiH_4). The films deposited at a gas flow ratio of 1 have a refractive index of 1.477 indicating that the films are silicon rich. As the N_2O gas-flow ratio increases, the deposition rate tends to decrease and so does the refractive index. However, when the gas-flow ratio reaches 10, the refractive index and the deposition rate tend to become saturated. The films deposited at a gas-flow ratio of 10 have a refractive index of 1.46, which is close to the refractive index of the thermally grown oxide. Figure 4.2 shows the breakdown strength as a function of the gas-flow ratio. The breakdown strength increases with increasing gas-flow ratio for the gas-flow ratios less than 10. But for gas-flow ratios between 10 and 20, the breakdown strength becomes saturated. Figure 4.3 shows that the oxide fixed charge (Q_f) and the interface trap

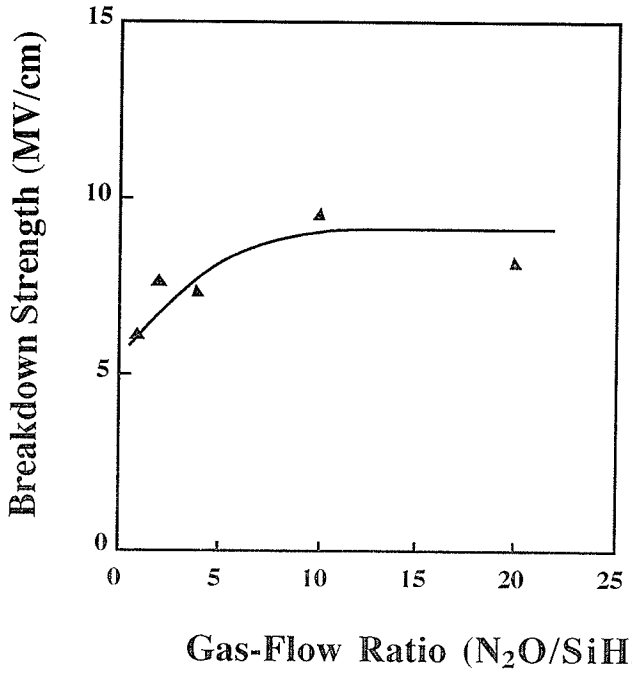

Figure 4.2. Breakdown strength of SiO_2 films as a function of gas flow ratio at a constant pressure of 27 mtorr.

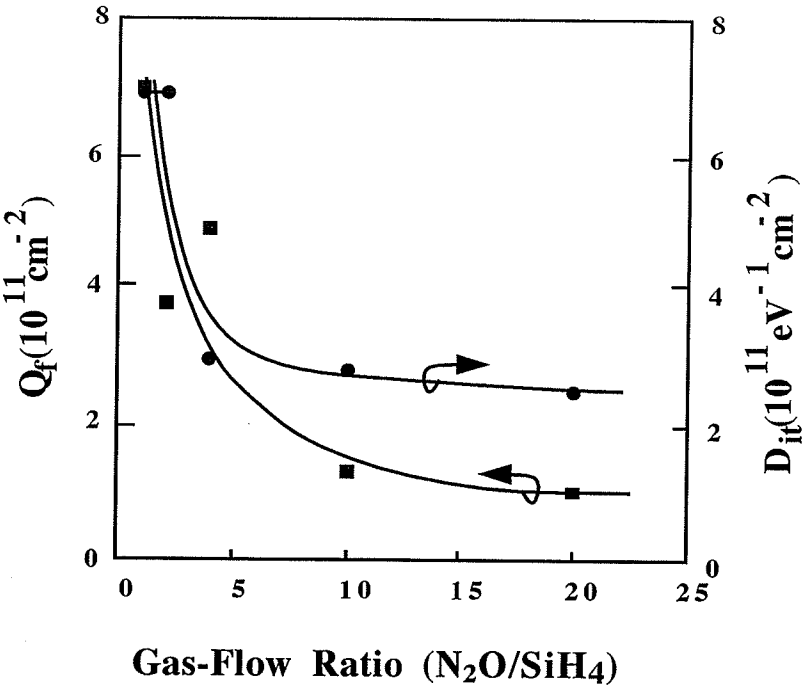

Figure 4.3. Oxide fixed charge (Q_f) and interface state density (D_{it}) as functions of gas flow ratio at a constant pressure of 27 mtorr.

density (D_{it}) as functions of gas-flow ratio after the PMA process. Films deposited at a low gas-flow ratio have a higher oxide fixed charge than those deposited at a high gas-flow ratio, and the value of D_{it} can reach as low as 10^{11} eV^{-1} cm^{-2} for films deposited at gas flow ratios between 10 and 20. The value of D_{it} follows the same trend of the oxide fixed charge. These results indicate that the higher the concentration of SiH_4 (gas flow-ratio of 1) the faster the deposition rate. The films produced at a fast deposition rate tend to be off-stoichiometry, which is reflected by their higher refractive index, lower breakdown voltage, and higher bulk and interface trap densities. Thus, to increase the deposition rate by using excess silicon concentration in the gas mixture can cause degradation in the film quality. Excess silicon concentration in the gas mixture may not only result in silicon rich films, but may also promote gas phase nucleation to form silicon dust particles inside the reactor.

4.2. The effects of the gas pressure

Figure 4.4 shows the deposition rate and the refractive index of the SiO_2 deposited films as functions of the gas pressure. The deposition rate increases linearly with the gas pressure. Thus, much higher deposition rates can be achieved by controlling the gas pressure than by controlling the gas flow ratio. The refractive index tends to increase, but the breakdown voltage tends to decrease with increasing pressure as shown in Fig. 4.5. The final breakdown strength is around 8-9 MV/cm for films deposited at gas pressures larger than 100 mtorr. Thus, the films deposited at pressures higher than 100 mtorr may not be stoichiometric, but the structure is not as bad as in the case of the gas-flow ratio less than 10. The high breakdown voltage of the films deposited at higher pressures can be

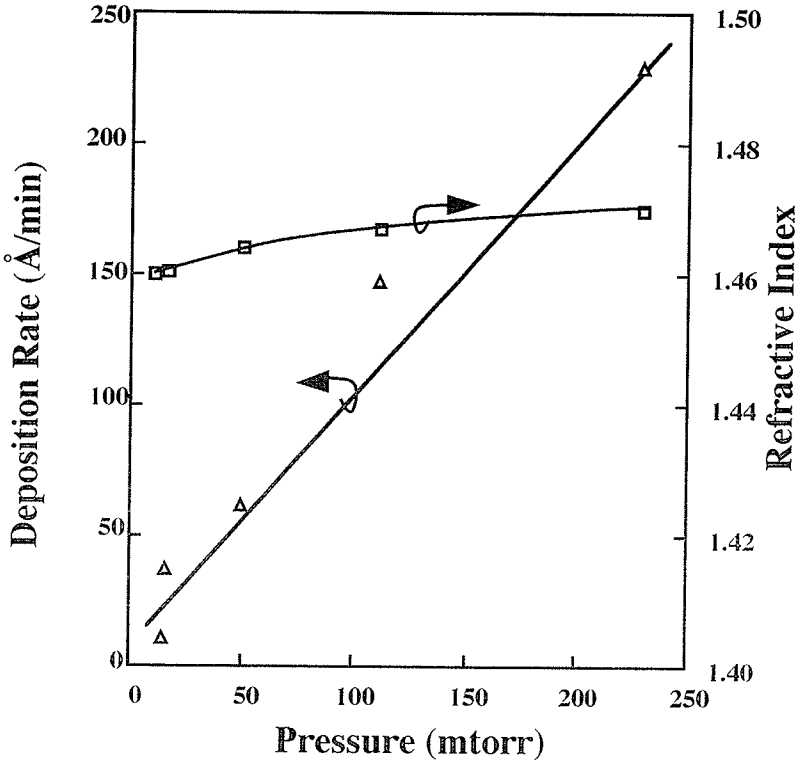

Figure 4.4. Deposition rate and refractive index of SiO_2 films as functions gas pressure at a constant gas-flow ratio of 10.

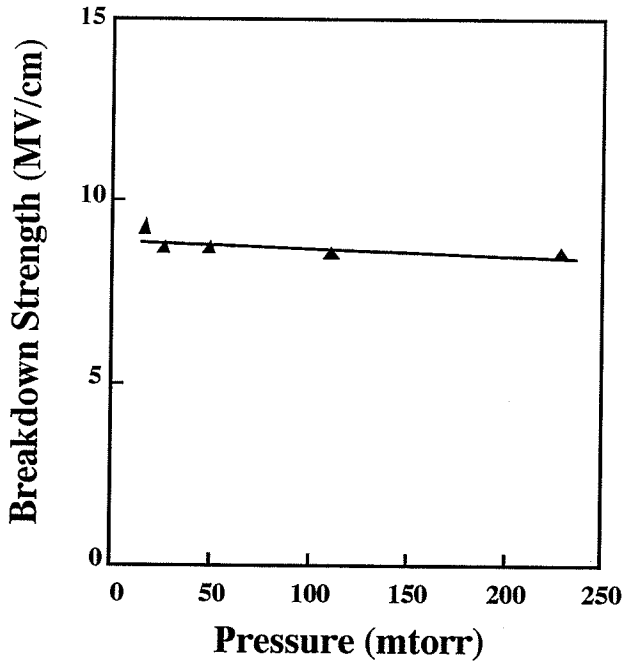

Figure 4.5. Breakdown strength of SiO_2 films as a function of gas pressure at a constant gas-flow ratio of 10.

explained as due to the increase in electron trapping in the high field region, which is caused by the non-stoichiometric SiO_2 or silicon rich films [4.4]. Such trapped electrons create an internal field opposite to the applied field as indicated by the ledge in the I-V characteristics. Oxide fixed charge increases with increasing gas pressure as shown in Fig. 4.6. For the PECVD films fabricated at low substrate temperatures, the adsorbed gas molecules on the substrate surface have a low mobility and hence they need a certain time to move around to reach a stable state. If the deposition rate is high, the adsorbed gas molecules could not move around to search for a stable state. This leads to a non-complete chemical reaction thus creating more defects or silicon rich films. However, the value of D_{it} does not depend on pressure, suggesting that the value of D_{it} may not depend on the growth process. This may be due to the fact that the present films were fabricated using the new system, and therefore they were not subjected to either ionic particle or photon bombardment, and that prior to the deposition process a thin native oxide film was already present on the silicon surface. It is also worthy to mention that before the PMA process, the D_{it} level is quite high ($>10^{13}$ eV^{-1} cm^{-2}). However, this high value of D_{it} can be annealed out by the PMA process. The high value of D_{it} before annealing may be due to the formation of an interface transition layer between Si and SiO_2 film, which may be similar to the native oxide that had already been present prior to the deposition process. This may be why the quality is not as good as the transition layer of the thermally grown oxide before annealing. Nevertheless, the treatment of the deposited SiO_2 in an H_2 environment at 400 °C can anneal out the excess D_{it} as previously have mentioned. This indicates that the role of H_2 in the annealing of PECVD films is as important as in the thermally grown oxide,

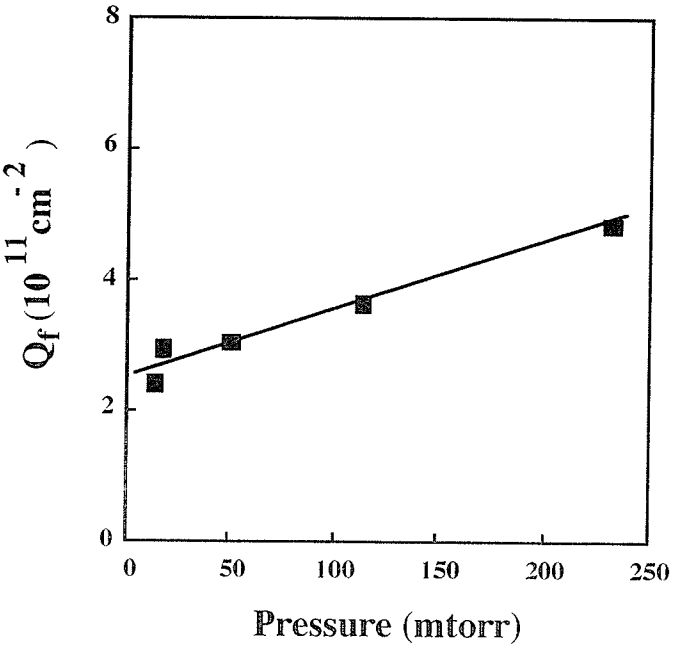

Figure 4.6. Oxide fixed charge (Q_f) and interface trap density (D_{it}) as functions of gas pressure at a constant gas-flow ratio of 10.

and that the substrate preparation for PECVD films is much more important than in the case of thermally grown oxide.

4.3. The effects of the substrate temperature

As mentioned in section 3.4, the chemical reaction at the substrate surface in the CPPP system is a heterogeneous surface rate limited reaction, and the deposition rate increases with increasing substrate temperature for temperatures below 300 °C. The refractive index of the SiO_2 films deposited by the CPPP system depends also on the substrate temperature. In this section some other results on the substrate temperature dependence will be presented. The infrared spectra of the SiO_2 films as functions of substrate temperature are shown in Fig. 4.7. It can be seen that there is an extra absorption band in the region of 850-950 cm^{-1} for films deposited at 30 °C and 100 °C, but this absorption band

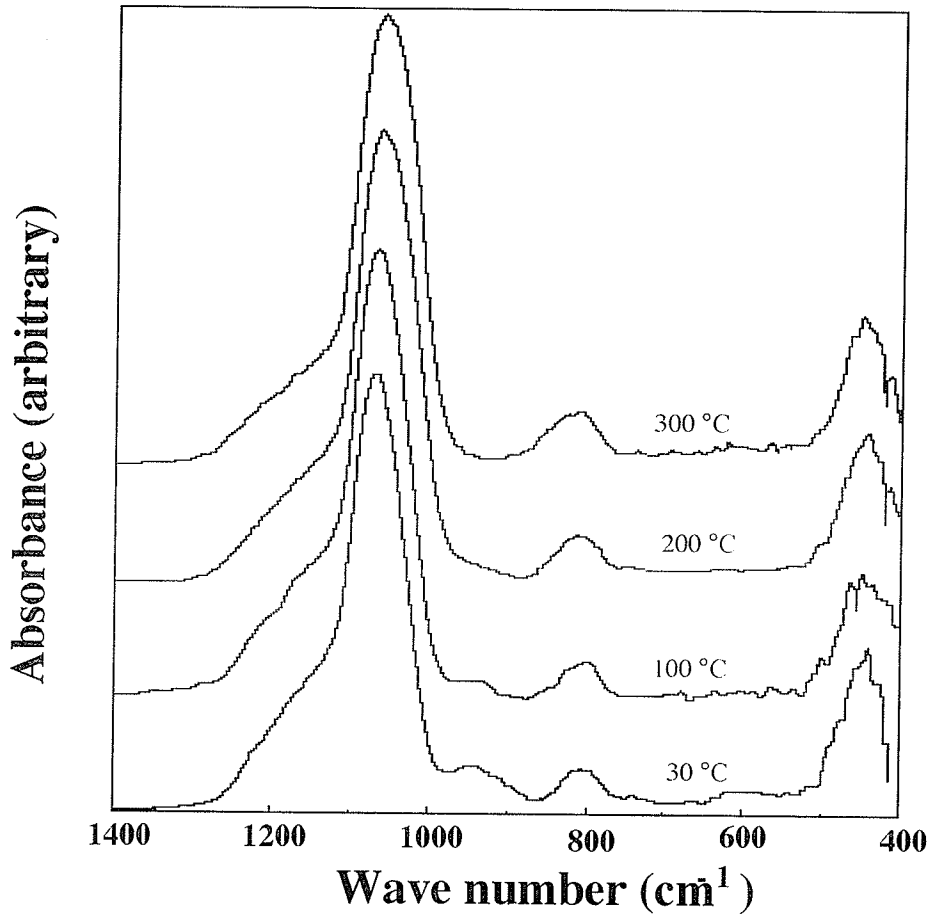

Figure 4.7. The IR absorption spectra of SiO_2 films deposited at various substrate temperatures for films fabricated by the CPPP system.

gradually disappears for films deposited at 200 °C or higher temperatures. This band is difficult to identify because it involves two absorption bands, 885 and 940 cm^{-1}. The 885 cm^{-1} band is frequently observed in deposited silicon dioxide films [4.5, 4.6] and has been assigned to Si-OH [4.7], Si-H[4.6], Si-N [4.8], and Si_2O_3 [4.5, 4.9,] vibrations. The 940 cm^{-1} band has been assigned to Si-OH [4.10] and Si-Si [4.11] vibrations. Adam et al [4.12] have also reported that there is a strong correlation between the intensities of the 885 and 940 cm^{-1} bands and the Si-H and Si-OH stretching modes, respectively. As there are no absorption in the stretching modes of Si-OH, Si-H and Si-N based on our IR absorption spectra, it is believed that this

850-950 cm^{-1} band may be assigned to oxygen deficiency, which is normally observed in pyrolytic silicon dioxide films [4.13, 4.14]. When the substrate temperature increases, this absorption band decreases and disappears as the substrate temperature reaches 300 °C, indicating that the substrate temperature does promote a phase change from a silicon-rich to a more stoichiometric structure.

The ratio (R_{IR}) of the shoulder height to the maximum absorption of the Si-O-Si stretching band R_{IR} as a function of substrate temperature is shown in Fig. 4.8. A value of $R_{IR} \leq 0.20$ indicates $x \approx 2$ for SiO_x [4.15] The present films deposited at 300 °C have $R_{IR} \approx 0.25$ indicating that x is very near 2 implying that the films are stoichiometric. This deduction is supported by the leakage current of these films measured at a constant electric field of 2 MV/cm as shown in Fig. 4.8. Both the R_{IR} and the leakage current increase as the substrate temperature decreases, implying that the films deposited at temperatures lower than 250 °C gradually become silicon rich.

The peak frequency of the Si-O-Si stretching absorption mode ν_m decreases with increasing substrate temperature. For a substrate temperature of 300 °C, ν_m is 1060 cm^{-1}, which is normally observed for high quality PECVD films. As the substrate temperature decreases, ν_m shifts toward a higher wave number and becomes 1070 cm^{-1} for a substrate temperature of 30 °C. Furthermore, FWHM increases with increasing substrate temperature, indicating that the films deposited at 300 °C have a higher intrinsic stress than those deposited at lower temperatures. Nakamura et al [4.16] have reported that ν_m is directly related to intrinsic stress and decreases with increasing intrinsic stress. The low intrinsic

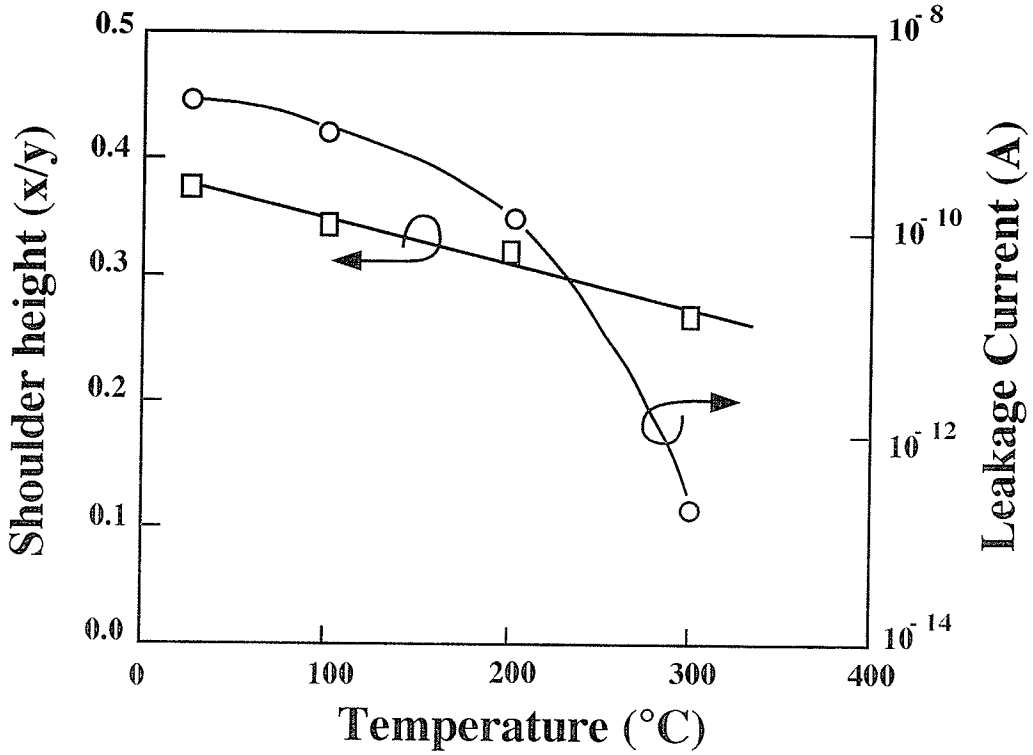

Figure 4.8. The shoulder height and the leakage current at an average dc field of 2 MV/cm as functions of substrate temperatures.

stress for film below 200 °C may be associated with the mixture of SiO_2 and genius silicon phase [4.16]. This is also consistent with the presence of the 850-950 cm^{-1} band. The high intrinsic stress in PECVD films is associated with the nature of the film growth process. The stress in PECVD films is tensile, that may be caused by the low pressure and low temperature during film deposition. The low pressure may lead to the film growth rate lower in the absorbed phase (before reaction) than in the solid phase (after reaction). This may in turn lead to the formation of elongated bonds thus resulting in the built-in tensile stress. Furthermore, low substrate temperature during film deposition may reduce the probability for the active species to reach an optimal position for interaction at the

substrate surface because of low surface mobility. This could also result in the elongated bonds in the films [4.17].

The I-V characteristics as functions of substrate temperature are shown in Fig. 4.9. As the substrate temperature decreases, the low-field leakage current increases and the breakdown strength decreases. It appears that at least a temperature of ≈ 270 °C is required to deposit good quality SiO_2 films. At substrate temperatures lower than 250 °C, premature injection occurs at fields much lower than the normally accepted threshold field ≈ 5 MV/cm. These results are consistent with the high-frequency C-V characteristics shown in Fig. 4.10. As the substrate temperature decreases, the C-V curve tends to shift towards negative gate voltage, indicating that the positive trapped charge inside SiO_2 films increases. The total oxide charges based on the flat-band shifts for four substrate temperatures are listed in Table 4.1. For the substrate temperature of 25 °C the C-V curve is stretched out indicating that the film consists of a high concentration of interface traps. The quasi-static C-V characteristics have also been measured. Typical results for three different substrate temperatures are shown in Fig. 4.11. Again, they show the same tendency: the interface trap density (D_{it}) increases as the substrate temperature is decreased below 300 °C. The values of D_{it} for different substrate temperatures are also given in Table 4.1. For the substrate temperature of 300 °C, D_{it} is about 5 x 10^{10} cm^{-2} eV^{-1}, which is about the same order as that for high quality thermal oxides. For a substrate temperature of 100 °C the C-V is quite distorted possibly due to high concentrations of both oxide traps and interface traps.

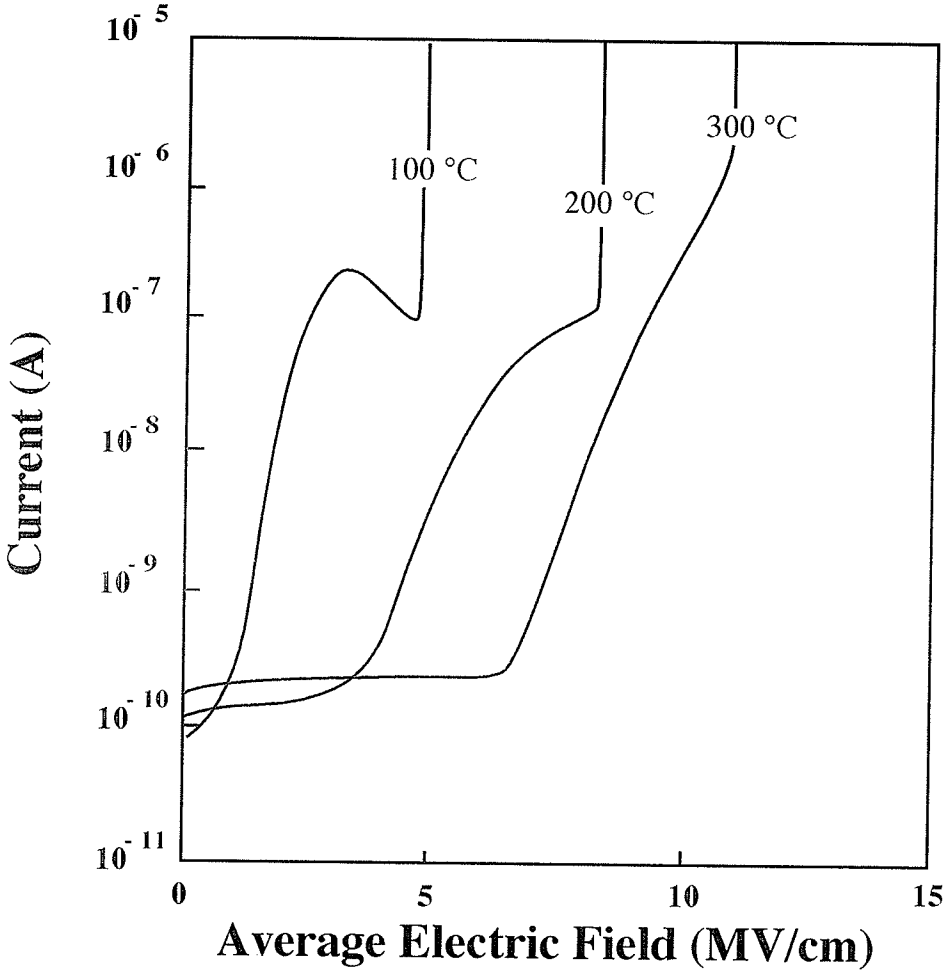

Figure 4.9. I-V characteristics for SiO_2 films fabricated at substrate temperature of 100, 200, and 300 °C.

Table 4.1. The stretching frequency (ν_m), full width at half maximum (FWHM), oxide charge (Q_{ot}),and interface trap density (D_{it}) for SiO_2 films deposited at four different temperatures.

Substrate Temp.(°C)	ν_m (cm^{-1})	FWHM (cm^{-1})	Qot (cm^{-2})	Dit ($cm^{-2}\,eV^{-1}$)
25	1067	77.0	1.4×10^{12}	----
100	1064	80.0	7.9×10^{11}	7.0×10^{11}
200	1061	87.4	4.2×10^{11}	6.2×10^{11}
300	1061	87.6	2.4×10^{10}	5.0×10^{10}

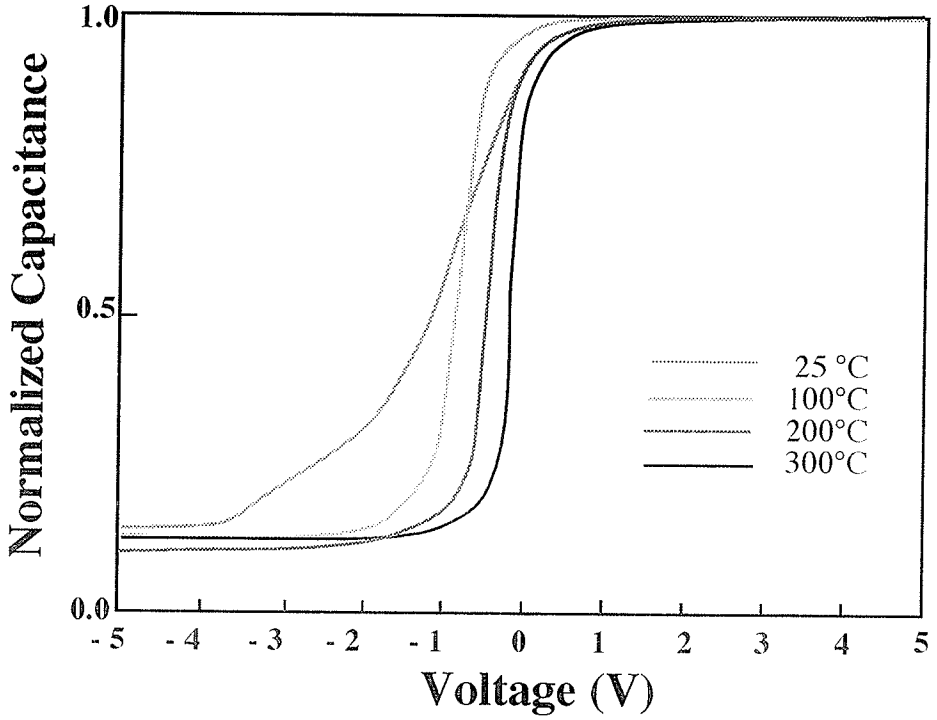

Figure 4.10. Typical high-frequency C-V characteristics for SiO_2 films deposited at substrate temperatures of 25, 100, 200, and 300 °C.

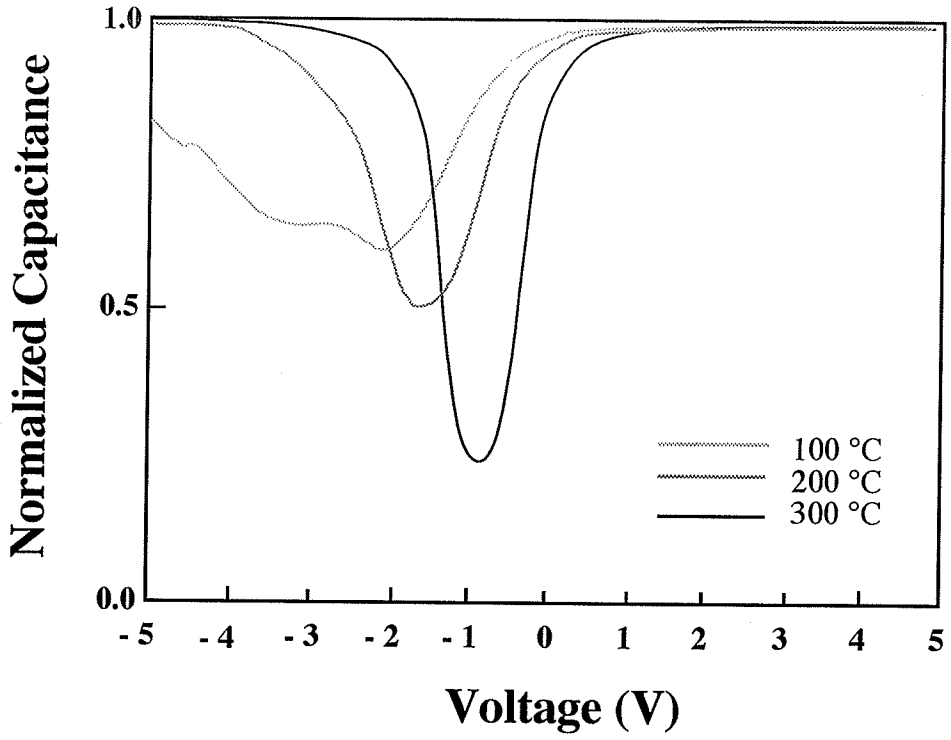

Figure 4.11. Typical quasi-static C-V characteristics for SiO_2 films deposited at three substrate temperatures of 100, 200, and 300 °C.

4.4. Thickness dependence of dielectric behavior of SiO_2 films

It has been shown that the quality of SiO_2 films deposited by the CPPP system at 300 °C is close to that of high quality thermal oxide with an average breakdown strength higher than 9 MV/cm and an interface trap density about 10^{10} eV^{-1} cm^{-2} for film thicknesses below 600 Å. In terms of electrical integrity these SiO_2 films are good enough for microelectronic devices. Unlike the thermal oxide that is grown at the interface between SiO_2 and Si, the PECVD SiO_2 film is deposited on the substrate surface layer by layer. Thus, It would be expected that the film growth mechanism for the latter would be much influenced by the deposition parameters, and that the composition and the structure should be uniform throughout the film and independent of film thickness if the deposition parameters are kept constant during deposition. By maintaining identical stable plasma and deposition parameters, a series of SiO_2 films with thicknesses ranging from 120 Å to 1000 Å were fabricated. It was first determined whether the composition and the structure of the fabricated films were thickness dependent. The film thicknesses were measured using the capacitance method and the measured values were consistent with those obtained from ellipsometric measurements. The refractive index measured by ellipsometry for a film of thickness of approximately 1425 Å corresponding to one half the ellipsometric cycle for the incident light with wavelength of 6328 Å is 1.458 which is about the same as that for the high quality thermal oxide. The etch rate of the PECVD films in HF solution is independent of the film thickness and is about 2 times faster than that of the high quality thermal oxide. The high etch rate for PECVD films may imply that these films have a low density and low compressive stress [4.18]. However, within the resolution of the analytical techniques used, no change

in composition and structure of the films with thickness could be found, at least for the thickness range form 120 Å to 1000 Å in this investigation. Figure 4.12 shows that the film thickness is linearly proportional to the deposition time, yielding a deposition rate of 8 Å per min, independent of film thickness. The FTIR results also show that there is no detectable difference in the Si-O stretching absorption band (at 1060 cm^{-1}) between films of different thicknesses, and that the absorbance at this band is linearly proportional to film thickness, following the Lambert-Bougmer's law as shown in Fig. 4.13. This law is given by [4.19]:

$$A = \log_{10}(I_o/I) = 0.434\ \alpha_{app}\ (d - x_s) \qquad (4.1)$$

where A is the absorbance, I_o and I are the incident and transmitted light intensities, respectively, α_{app} is the apparent absorption coefficient, x_s is the thickness of the native oxide layer on the silicon surface which is assumed to be zero, and d is the thickness of the SiO_2 film. The apparent absorption coefficient deduced from Fig. 4.13 is about $1.5x10^4$ cm^{-1} which is smaller than the value of $3.34x10^4$ cm^{-1} for thermal oxides [4.20]. The FTIR spectrum for samples after PMA has also been measured. No detectable difference in IR spectrum between the samples as deposited and those after PMA was found indicating that PMA at a temperature of 400 °C for 30 minutes may anneal out some defects at the SiO_2/Si interface, but does not cause any change in the composition and structure of the films.

At applied fields below the threshold field for the FN tunneling injection, the bulk SiO_2 can be considered approximately free of trapped charge. The general shape of the C-V characteristics (Plotted in C-F where F is the average applied field which is equal to the applied gate

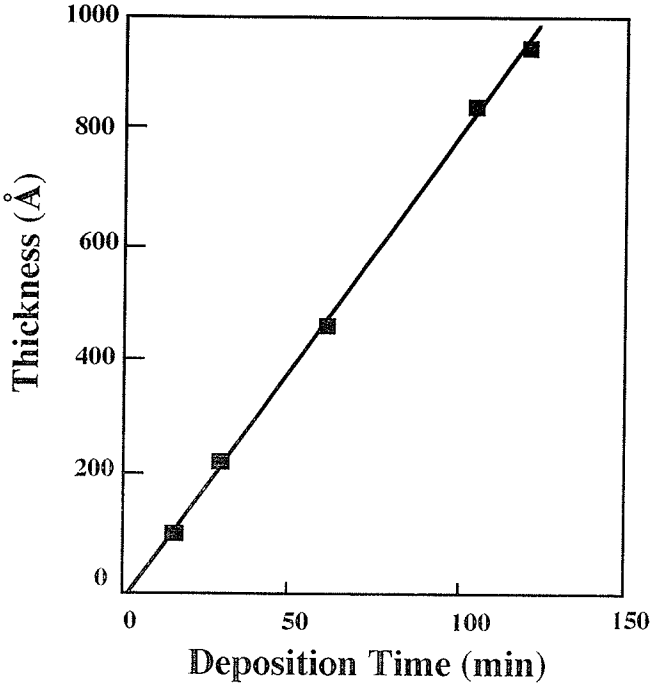

Figure 4.12. The deposited SiO_2 film thickness as a function of deposition time. The linear relationship yields a deposition rate of 8 Å/min.

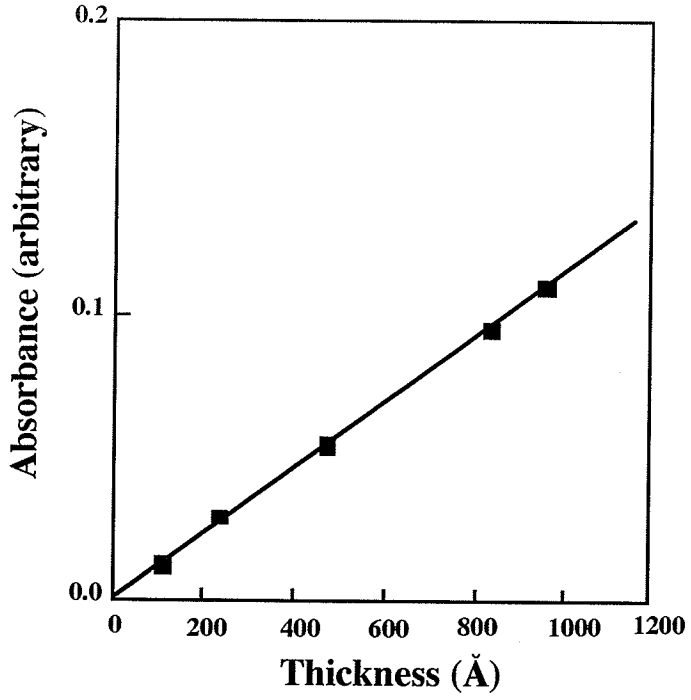

Figure 4.13. The absorbance at the Si-O stretching band as a function of SiO_2 film thickness.

voltage divided by the oxide thickness) are practically independent of film thickness as shown in Fig. 4.14. The curves were plotted in C-F rather than C-V mainly for the convenience of the comparison of films with different thicknesses. The difference in minimum capacitance is due to the difference in normalized SiO_2 capacitance which is inversely related to film thickness. The flat band voltage as measured from these high frequency C-V (HF C-V) curves shows a shift toward negative values. By assuming that this shift is caused mainly by the work function difference and the positive oxide fixed charge, it is estimated that the positive oxide fixed charge is about 10^{11} q cm^{-2}. The quasi-static C-V (QS C-V) characteristics were also measured. Typical results for two different film thicknesses are shown in Fig. 4.15. Again, they do not appear to be thickness dependent. The positive oxide fixed charges (Q_f) and the densities of interface traps (D_{it}) deduced from HF C-V and QS C-V results for different film thicknesses are given in Table 4.2. Within the limit of the accuracy in determining the values of these parameters, both Q_f and D_{it} can be considered to be practically independent of film thickness.

Figure 4.16 shows the I-V characteristics for various SiO_2 film thicknesses measured using a linear voltage ramp at the rate of 0.2 MV/cm/sec with the aluminum gate electrode biased at positive polarity. It can be seen that the Fowler-Norheim (FN) injection of electrons from the n-Si starts at an average field of 5.0 - 5.5 MV/cm and the I-V characteristics follow the FN tunneling relation [4.21] until the onset of the space charge limitation. The threshold field for the onset of this limitation increases with increasing film thickness. This phenomenon suggests that

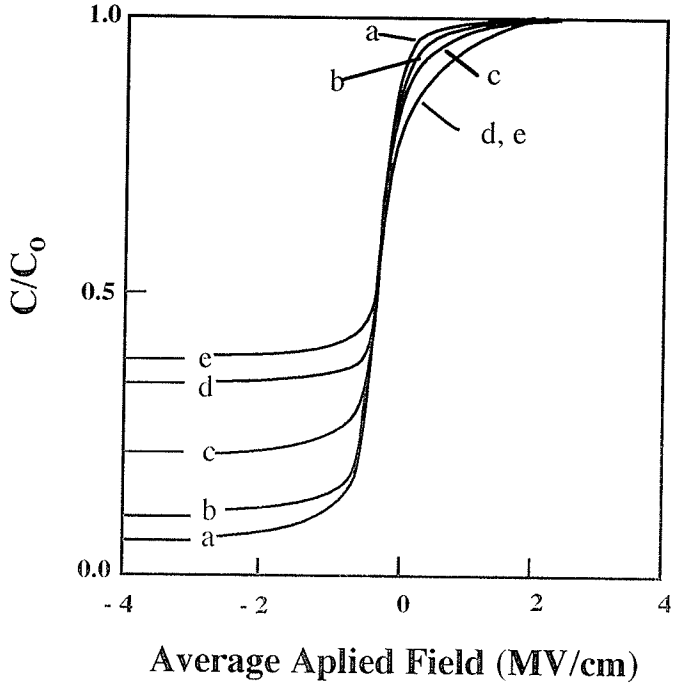

Figure 4.14. High frequency C-V characteristics (plotted in normalized capacitance as a function of average applied electric field) for SiO_2 film thickness. (a) 120 Å, (b) 238 Å, (c) 480 Å, (d) 845 Å and (e) 960 Å.

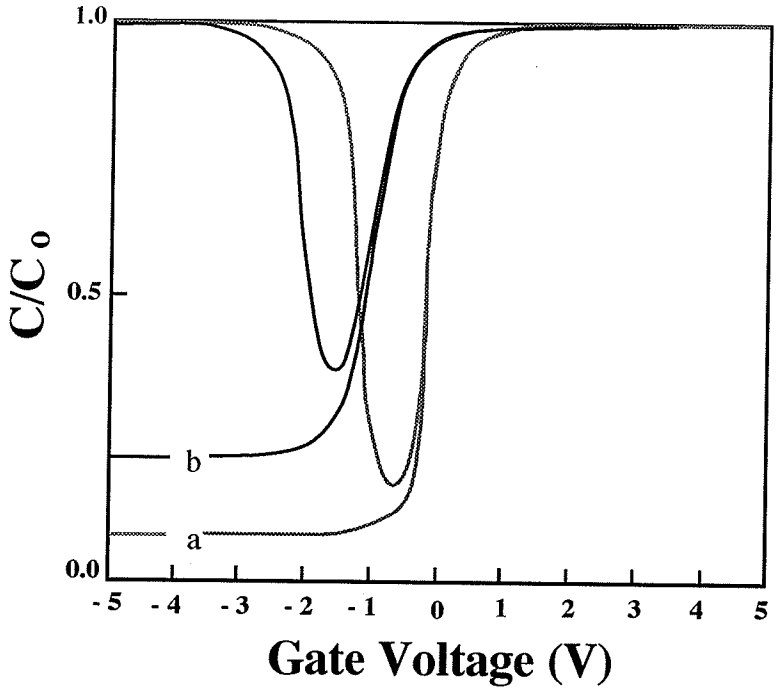

Figure 4.15. Typical high frequency and quasi-static C-V characteristics for SiO_2 film thickness (a) 120 Å, and (b) 480Å.

Table 4.2. Values of oxide fixed charge density, Q_f, and interface trap density, D_{it}, deduced from C-V characteristics for various SiO_2 film thicknesses, d.

Sample	d(Å)	Q_f (q cm^{-2})	D_{it} (cm^{-2} eV^{-1})
TD01	120	$1.42X10^{10}$	$1.5X10^{11}$
TD02	235	$1.12X10^{11}$	$5.0X10^{11}$
TD04	480	$6.20X10^{10}$	$2.4X10^{11}$
TD05	845	$4.16X10^{11}$	$6.0X10^{11}$
TD07	966	$4.80X10^{11}$	----------

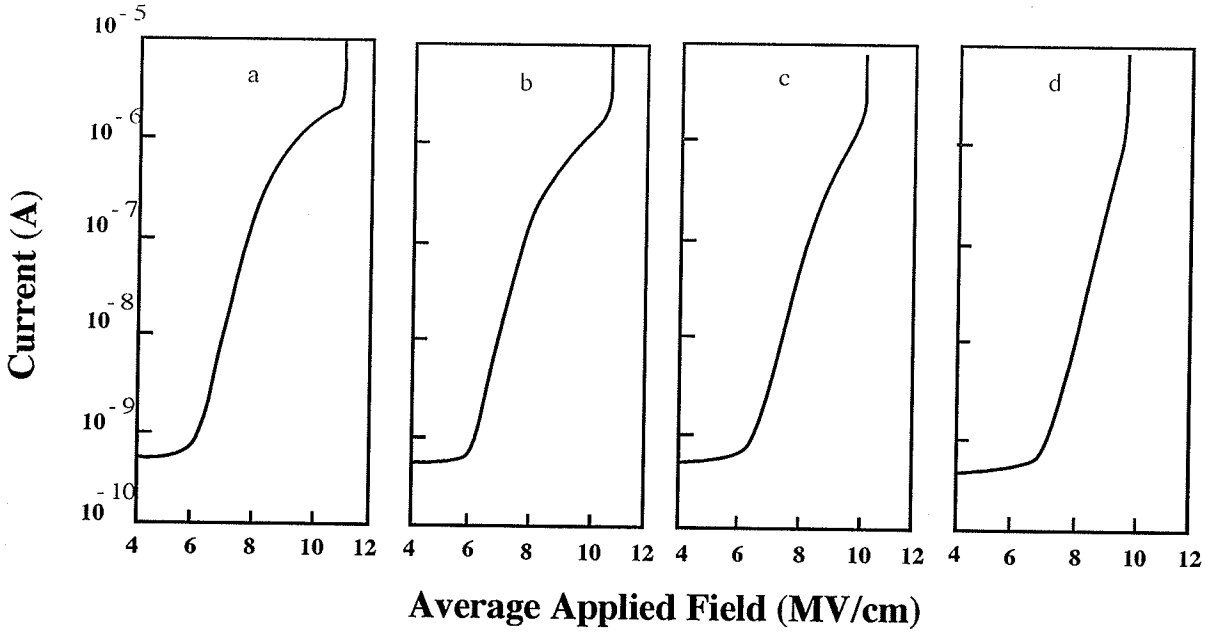

Figure 4.16. Current-Voltage characteristics (plotted in current as a function of average applied electric field) for SiO_2 film thickness: (a) 120 Å, (b) 240 Å, (c) 480 Å, and (d) 845 Å.

the motion of the injected electrons in the SiO_2 bulk is mainly controlled by their interaction with the lattice rather than with the traps in the forbidden gap of the SiO_2 bulk [4.22]. This also implies that the injected electrons may travel quite a distance before being effectively trapped. At any heterojunction between two different materials, there always exists an interface layer caused either by the mismatch between the two material surfaces, or by the fabrication process or the stress. While much attention has been devoted to the SiO_2/Si interface, the effect of the SiO_2/metal interface is hardly mentioned in the literature. In practice, water in the form of an hydroxyl group can be strongly bound to the Si atoms on the oxide surface and this hydroxyl group will react with Al producing hydrogen and forming aluminum oxides [4.23] and hence an interface layer. It is believed that in the SiO_2/Al interface layer there are deep electron traps. Some of the electrons moving toward the aluminum anode will be trapped there forming a negative trapped charge which then retards the on-coming electrons thus gradually increasing their interaction with bulk traps. In other words, the bulk traps in the SiO_2 film are gradually filled starting from the anode towards the cathode. As the current and hence the trapping rate increase, an internal field rapidly builds up which tends to suppress the field towards the cathode and to enhance the field toward the anode as shown in Fig. 4.17. When the trapped electron charge builds up to a certain level, it begins to significantly affect the current injection, and the I-V characteristics start to deviate from the FN relation. The trapped charge is more effective in suppressing the field, and hence the electron injection at the injecting contact, for a given trapped charge quantity located close to the contact.

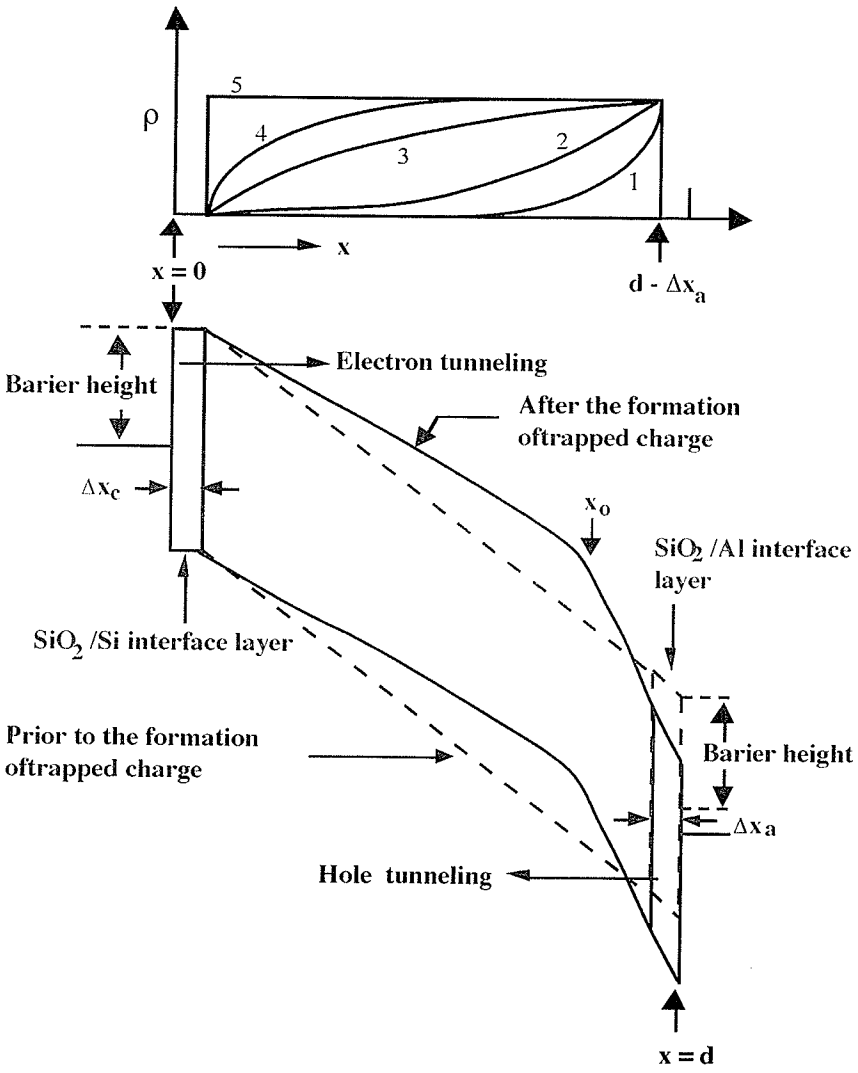

Figure 4.17. Schematic diagrams illustrating the build-up of negative space charge Q and its effect on potential distribution due to electron injection and filling of electron traps in the bulk of SiO_2. The numbers 1, 2, 3, 4, and 5 show the gradual change of the space charge distribution as the space charge builds up. Electron injection is at x=0 (cathode). Δx_C, and Δx_a are the widths of the interface layers at the Si and at the Al surfaces, respectively, which are supposed to be very small as compared with the oxide thickness.

By taking the location of the cathode surface (the electron-injecting contact) at x = 0 and that of the anode (Al gate electrode) at x = d, the centroid, x_o, of the trapped electron charge should be located at the same position as the first sheet of trapped electron charge near the anode. As the trapped electron charge builds up sheet by sheet toward the electron injecting contact, the centroid, x_o, also moves toward the electron injecting contact; i.e. x_o decreases because it is defined as:

$$x_o = \frac{\int_0^d \rho(x)\, x\, dx}{\int_0^d \rho(x)\, dx} = \frac{\int_0^d \rho(x)\, x\, dx}{Q} \qquad (4.2)$$

where $\rho(x)$ is the trapped charge density at x and Q is the total trapped space charge in the oxide. The internal field created by such a trapped charge is given by [4.24]:

$$F_{in} = \frac{Q}{\varepsilon_{ox}}\left(1 - \frac{x_o}{d}\right) \qquad (4.3)$$

where ε_{ox} is the permitivity of the SiO_2 film. For the same quantity of Q, the thinner is the sample the smaller the value of x_o/d and hence the higher the value of F_{in}. On the basis of the above argument about the build up of trapped space charge, the trapped space charge effect is greater for a thin sample than for a thick one. This is why the threshold field for the onset of the deviation from the FN tunneling relation (or the onset of the space charge limitation) increases with increasing film thickness as shown in Fig. 4.16. For thick samples such as 845 Å, the threshold field for the onset of the breakdown process may be lower than that for the onset of space charge limitation for that particular voltage ramp rate used. In this case

the I-V characteristics follow the FN tunneling relation right up to the breakdown field. For thin samples such as that of 120 Å the bulk traps may have been almost completely filled prior to the onset of the breakdown process during the first cycle of the ramp voltage stressing. In order to study the dielectric behavior in some detail, the following experimental procedure was used to reveal the effect of the applied high electric stress on the I-V and C-V characteristics. First, a high-frequency C-V curve for a virgin MOS capacitor device was taken and then the device was stressed with the first cycle of voltage ramp at 0.2 MV/cm/sec until it reached a predetermined level at about 8-9 MV/cm (close to the breakdown field) and then held there for 10 seconds. The stress was then released and the C-V curve was immediately measured, and followed by a second cycle of voltage ramp stressing. This procedure was repeated several times. The I-V and the corresponding C-V characteristics for the SiO_2 film of 120 Å are shown in Fig. 4.18, and those for the SiO_2 films of 845 Å are shown in Fig. 4.19. For thin samples such as 120 Å, there is a stretch-out in the C-V curve after the first cycle indicating that the interface trapped charge plays an important role in both the I-V and the C-V characteristics. There is no shift in either the I-V or the flat band of the C-V curves after the second stress cycle indicating that the bulk traps may have been almost completely filled during the first cycle of ramp voltage stressing, and that further stress does not increase the trapped charge even with the stress time increased from 10 sec to 1 min for each cycle as shown in Fig. 4.18. However, the situation for thicker samples such as 845 Å is quite different. In this case, the I-V curves shift toward higher voltage and C-V curves shift towards the positive gate voltage direction after each stress cycle

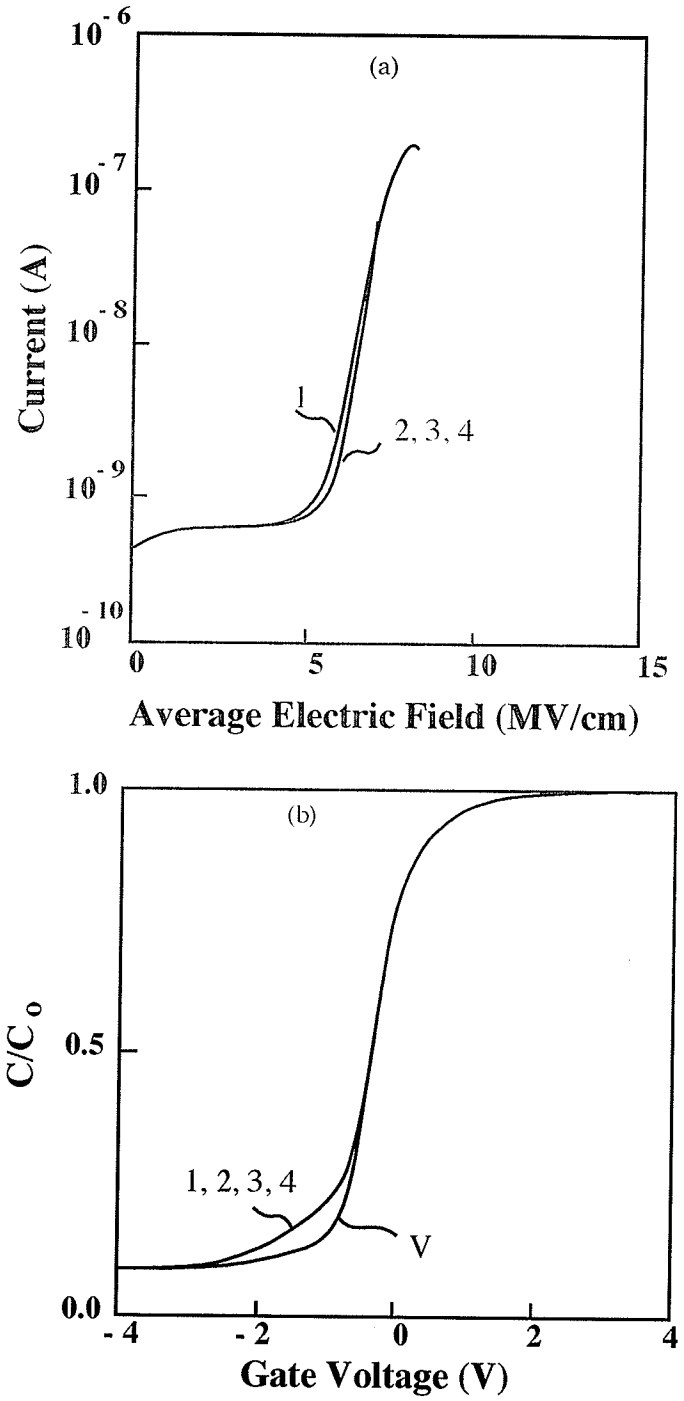

Figure 4.18. The effects of high electric stress on (a) the I-V and (b) the high frequency C-V characteristics for a typical SiO_2 film of 120 Å in thickness for the virgin sample, V, and after 1^{st}, 2^{nd}, and 3^{rd} cycle of stressing. After each cycle a stress of 8-9 MV/cm was applied to the device for 10 seconds prior to the measurements for the following cycle.

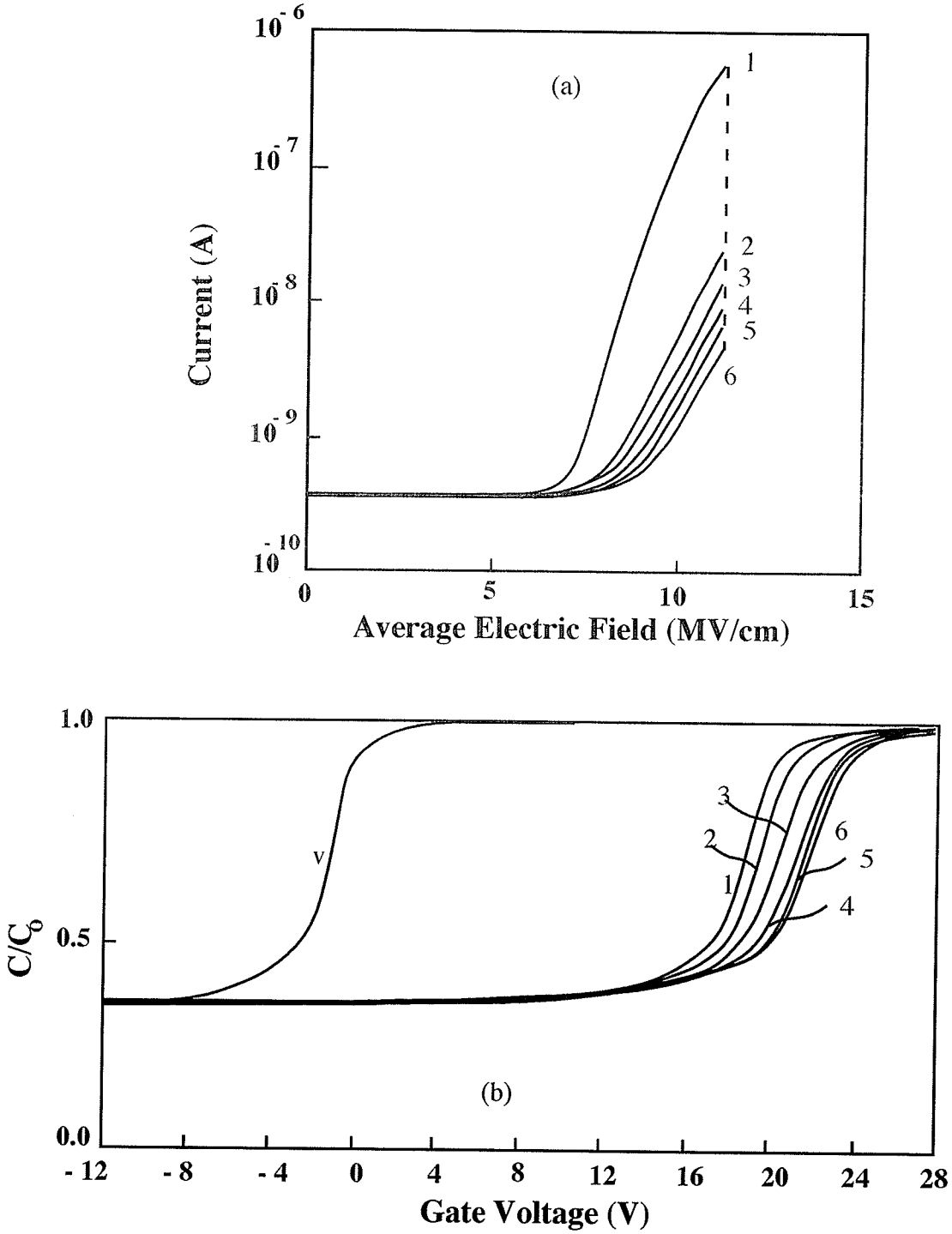

Figure 4.19. The effects of high electric stress on (a) the I-V and (b) the high frequency C-V characteristics for a typical SiO_2 film of 845 Å in thickness for the virgin sample, V, and after 1st, 2nd, 3rd, 4th, 5th, and 6th cycle of stressing. After each cycle a stress of 8-9 MV/cm was applied to the device for 10 seconds prior to the measurements for the following cycle.

indicating that the higher or the longer the application of the high electric stress, the more the negative space charge builds up in the bulk of the SiO_2 as shown in Fig. 4.19. The amount of the negative space charge that can build up in SiO_2 depends not only on the total time of applied electric stressing but also on the electric stress. For low electric stresses such as 6 MV/cm, the high frequency C-V curve shifts only after the first 10 seconds of electric stressing and then remains unchanged upon further stressing as shown in Fig. 4.20 (a). However, for higher electric stresses such as 8.5 MV/cm the C-V curve shifts further toward positive gate voltage as shown in Fig. 4.20(b). If the bulk trap concentration is distributed uniformly in space, the total number of traps is larger for a thick sample than for a thin one. It is likely that the bulk traps are not completely filled after the first cycle of the ramp voltage stressing. The function of the applied high electric stress is to increase the electron injection and the trap-filling. From these results it is difficult to know even under a long period of high electric stress whether all the bulk traps are filled or whether any new traps are created by the hot injected electrons. By assuming that for the 120 Å samples, all the traps are filled during the first cycle of the voltage ramp stressing, the current ledge shown in Fig. 4.18 gives the bulk trap concentration of $10^{14}\,cm^{-3}$ which is small. However, based on the flat band shift shown in Fig. 4.19 for the 845 Å samples the bulk trap concentration could be $10^{16}\,cm^{-3}$. Comparison of these two values, suggests that further stress may not only enhance electron injection and trap filling but may also create new traps [4.25]. The present experimental work does not provide enough evidence about new trap creation by hot electrons. However, it may be speculated that each electron-trapping event will evolve an energy of the order of 2-5 eV depending on the trap energy levels. This energy,

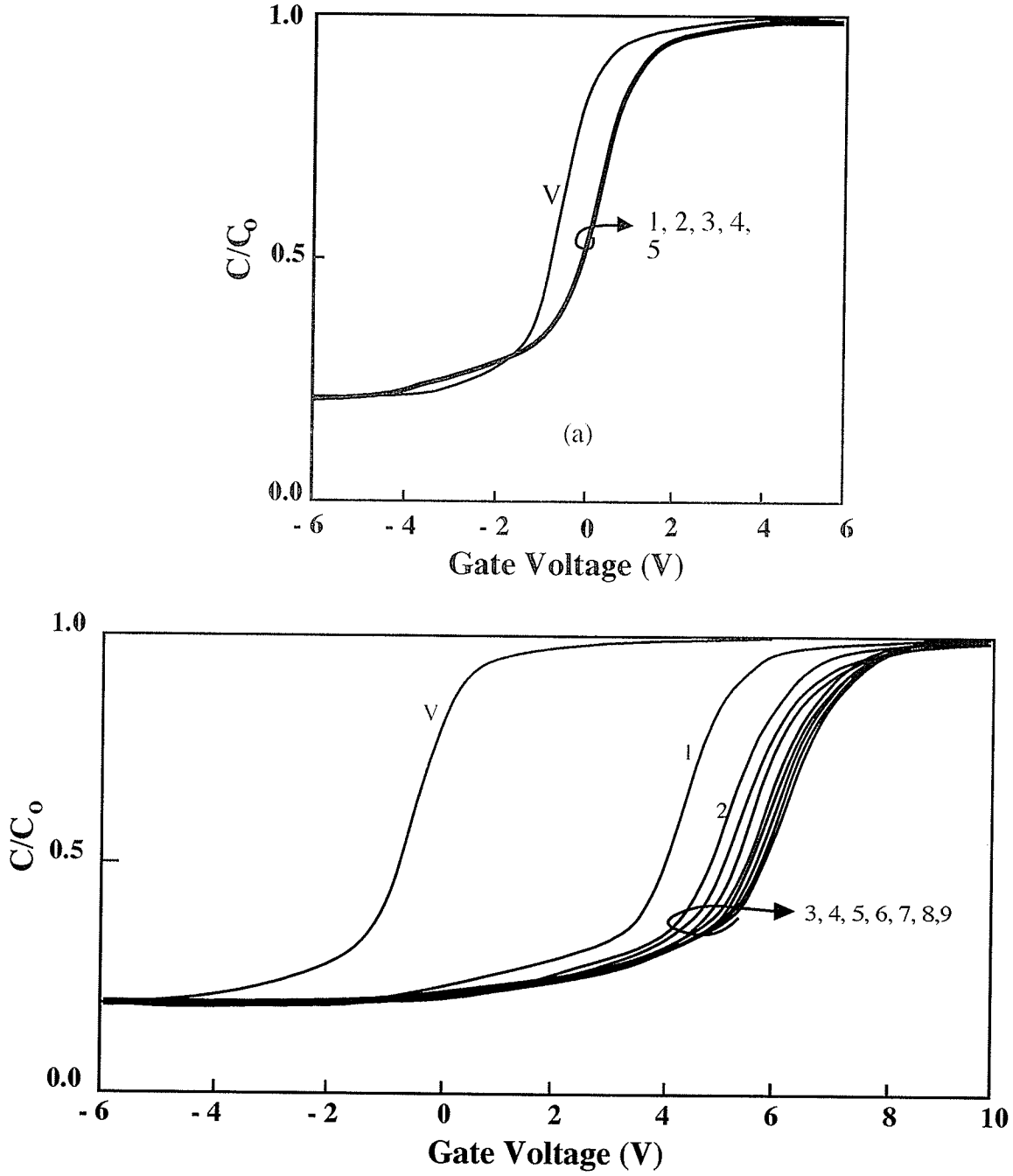

Figure 4.20. The effect of high electric stress on the high frequency C-V characteristics for a typical SiO_2 of 480 Å in thickness for the virgin sample, V, and after 1^{st}, 2^{nd}, 3^{rd}, 4^{th} .... cycles of stressing. After each cycle a stress of (a) 6 MV/cm and (b) 8.5 MV/cm was applied to the devices for 10 seconds.

if not converted to light emission, will be dissipated in the material by the breaking of bonds and hence the creation of defects or traps [4.26]. By observing the breakdown size on the SiO_2 surface at the gate after the removal of the aluminum electrode under a microscope of magnification X400, the average size of the breakdown channel has been estimated to be about 2-10 μm in diameter. It is most likely that for carrier injection from the electrodes at fields higher than the injection threshold field, the electric conduction is filamentary because the electrode surface is not microscopically identical in asperity and surface condition from domain to domain. Thus, there may be one or more micro-regions in which the potential barrier has a profile more favorable for carrier injection than in other regions [4.27, 4.28]. Furthermore, the material itself is never microscopically homogeneous. Thus, the current density is definitely not uniform. Supposing that the current filament which leads to final destructive breakdown is the filament carrying the majority of the total current, then the current density of this filament can be estimated. For the filament size of 10 μm in diameter, the current density may reach 10 A/cm^2 for the total current of 10^{-6} A. The energy stored in the filament at the current corresponding to an average field of 9 MV/cm is approximately equal to 90 MW/cm^3. This is an enormous energy far more than the energy required to cause thermal instability. It is believed that destructive breakdown is initiated by thermal destruction and followed by impact ionization leading to a sharp increase in current at the breakdown field. There is no evidence of impact ionization prior to the occurrence of thermal instability. Thermal destruction is the way to open up some local micro-regions to provide large mean free paths for the electrons to accelerate to energies greater than the band gap (9.0 - 9.5 eV) and to cause

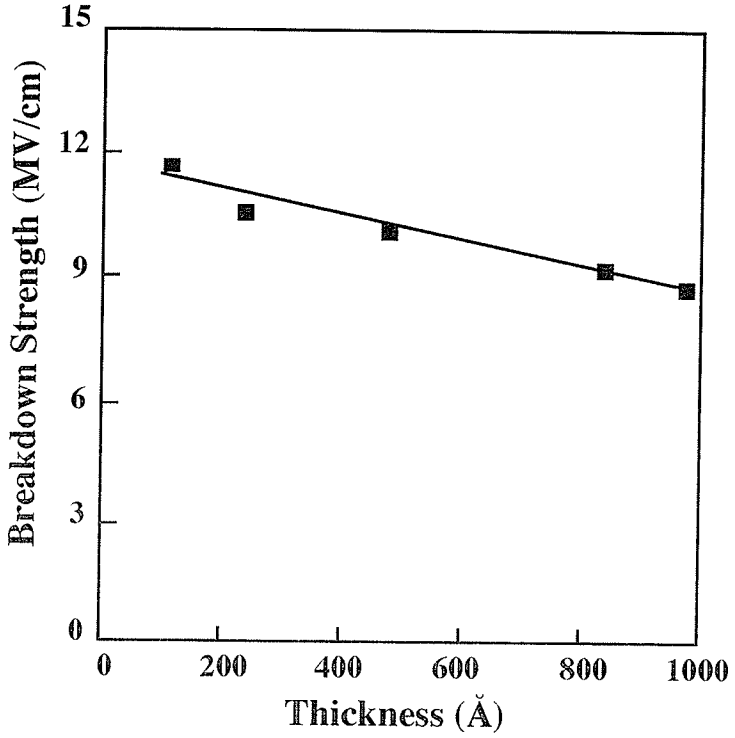

Figure 4.21. The breakdown strength as a function of SiO_2 film thickness.

impact ionization. Figure 4.21 shows that the average breakdown strength decreases with increasing film thickness. A similar phenomenon has been observed in thermal oxides [429] and other dielectric materials [4.30]. Heat transfer is easier for thin samples than thick ones. This can be considered as one of the factors responsible for the decrease of breakdown strength as the film thickness increases [4.31]. The I-V curve is dependent on the voltage ramp rate as shown in Fig. 4.21. The lower is the voltage ramp rate the lower the breakdown field. Since the thermal run away effect is proportional to $\int I^2(t)\ R(t)\ dt$, where R(t) is the conduction filament resistance, and both R(t) and I(t) are time dependent, the critical field or the critical current density for the onset of thermal instability is lower for the lower ramp rate as expected. For a fixed ramp rate, the effect of the oxide trapped space charge, which creates an internal field opposite against the applied field, is greater for the thin samples than for the thick ones at a

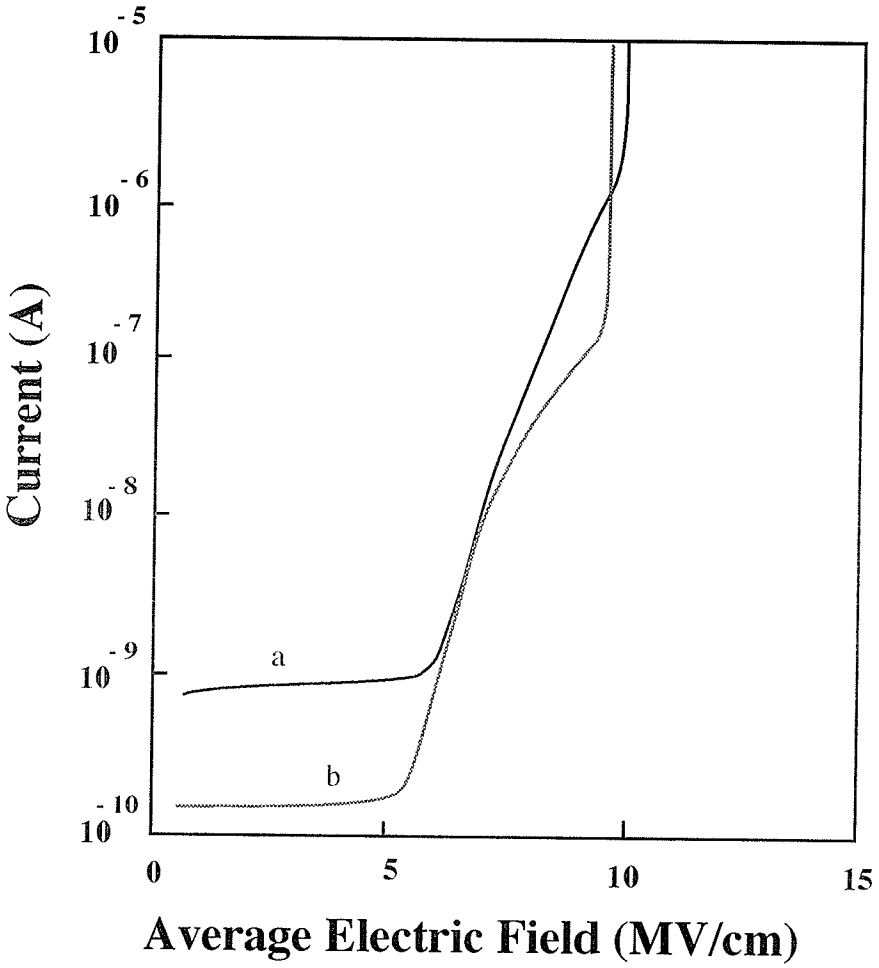

Figure 4.22. The effects of the ramp rate on the ramp Current-Field characteristics for the SiO_2 film thickness of 845 Å (a) for the ramp rate of 0.8 MV/cm/sec and (b) for the ramp rate of 0.1 MV/cm/sec.

given applied field as discussed above. This can be considered as another factor responsible for the decrease in the average breakdown strength with increasing film thickness. It should be noted that when the volume of the negative trapped space charge for thick samples reaches a value high enough to increase the field at the anode to such a level that the potential barrier becomes sufficiently narrow for effective tunneling of holes from the anode, then double injection ensues [4.32]. Although the mobility of holes in SiO_2 is very small, hole injection provides a channel for

recombination. Several investigators have observed that after the application of high electric stress, the I-V curve may show a negative differential conductance and the C-V curve tends to shift to negative voltage [4.33] and that under high field stress there is light emission [4.34]. Double injection provides an alternative, though speculative, explanation for these phenomena.

4.5. The effects of dc biasing to the SSEC

In chapter 3, it was shown that the SSEC can effectively suppress charged particles progressing towards the processing chamber if the SSEC is properly biased with a dc voltage. The schematic diagram of the SSEC is shown in Fig. 3.3(b) of chapter 3. Without a dc bias, the potential created by the plasma volume at the front wall of the SSEC at a constant gas flow of 10 sccm of N_2O is negative with respect to the screening mesh ground as shown in Fig. 4.23. The negative potential at the front wall causes positive ions to move from the plasma volume towards the SSEC. The potential at the back wall under the same non-biasing condition is positive with respect to the screen mesh ground. Thus, the total internal potential between the front wall and the back wall is about 4 V at the gas pressure of 10^{-3} torr. The internal potential drives the positive ions through the SSEC and guides them along the central line toward the substrates. This potential decreases with increasing gas pressure because the mean free path of the charged particles in the plasma decreases, thus decreasing the probability of impact ionization and hence decreases the number of charged particles. However, for most ECR microwave PECVD operations the gas pressure used is about 10 - 20 x 10^{-3} torr. Within this pressure range, the internal potential between the front wall and the back

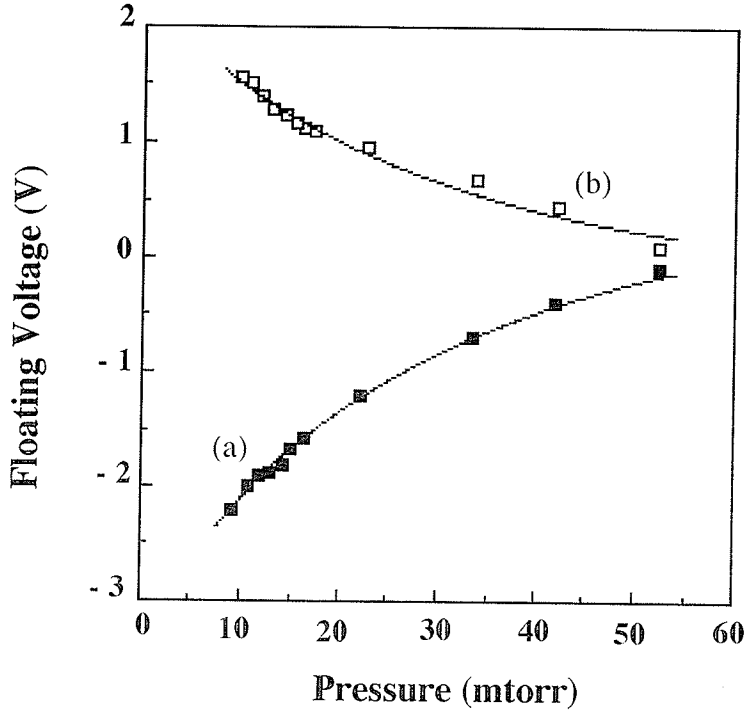

Figure 4.23. (a) the floating potential at the front wall of the SSEC and (b) the floating potential at the back wall of the SSEC under non-biasing condition.

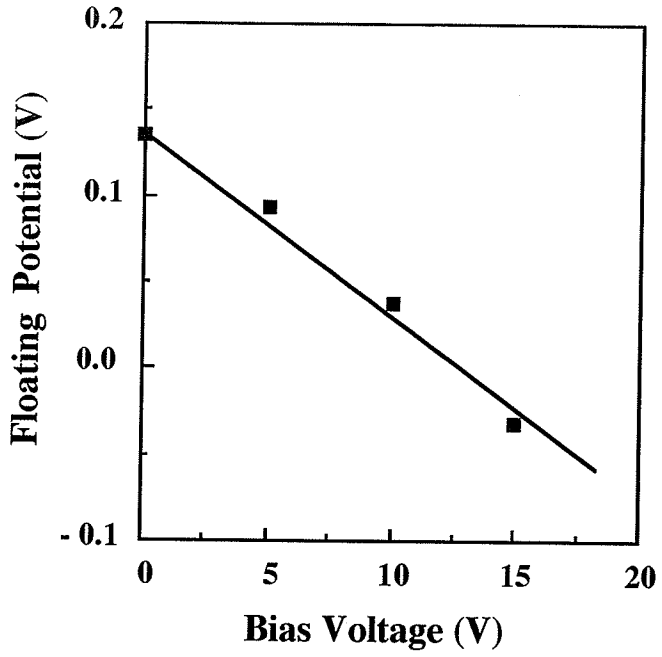

Figure 4.24. The floating potential measured at distance of 5 cm from the back wall as a function of negative voltage applied equally to both the front and the back walls.

wall is about 2.5 - 4.0 V.

The floating potential has been measured using a tungsten probe at a point 5 cm from the back wall. At zero bias the floating potential is 0.135 V and positive with respect to ground indicating that there is a certain number of positive ions entering the processing chamber and possibly bombarding the substrates and the on-growing films during PECVD. In order to reduce the positive ions passing through the SSEC and flowing toward the substrates, dc bias was applied to the front wall and the back wall. The negatively biased front wall tends to attract positive ions toward it, but when the ions enter the SSEC, the field in the region between the front wall and the central screening mesh tends to block them from passing through the screening mesh. However, some ions may leak through to reach the back wall. Because the back wall was also negatively biased, it was difficult for the positive ions passing through the SSEC to travel far away from the back wall. This is why, with the front wall and the back wall negatively biased with respect to ground, the floating positive potential with respect to ground decreases with increasing magnitude of the negative bias as shown in Fig. 4.24. This indicates that the number of positive ions reaching the probe decreases under such a biasing condition. Furthermore, the negatively biased back wall also tends to reduce the kinetic energy of the impinging positive ions toward the substrates. Without bias, the floating potential is about + 0.135 V with respect to ground. Although this internal potential seems very small, it may create a field as high as 10 MV/cm inside the on-growing SiO_2 film when the thickness of the film is still thin, say 15 Å. Such a high field occuring during the initial stage of the film growth may cause electrical breakdown, leading to damage of the

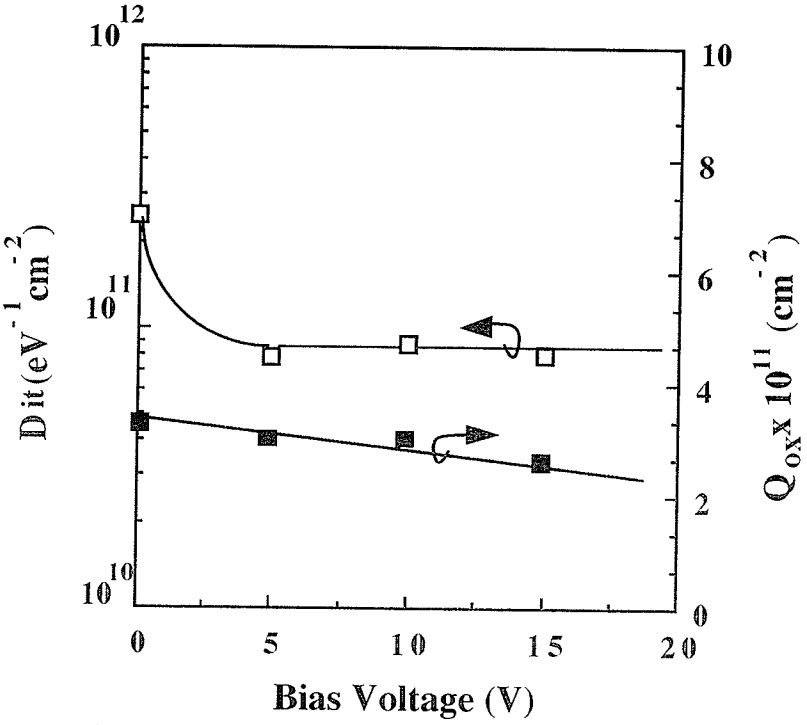

Figure 4.25. The interfacial trap density and the oxide bulk traps concentration as functions of negative bias voltage.

SiO_2/Si interface.

The SiO_2/Si systems with SiO_2 films grown at 20 x 10^{-3} torr under various bias voltages have been studied. It can be seen from Fig. 4.25 that the D_{it} and Q_{ox} decrease with increasing negative bias voltage. It should be noted that various biasing conditions have been tested, such as positive bias for the front wall and negative bias for the back wall, positive bias for the front wall as well as for the back wall etc. However, none would improve the behavior of the SiO_2/Si system. Only the bias condition with both the front and the back walls negatively biased with respect to ground tends to improve D_{it} and Q_{ox} levels. Although the effect of biasing is not very significant, the experiment shows that positive ion bombardment on the substrates and the on-growing films cause damages. It should also be noted

that the SSEC itself without bias reduces significantly the number and the energy of impinging energetic particles from bombarding the substrates and the on-growing SiO_2 films, and hence improves the behavior of the SiO_2/Si systems.

References for chapter 4

[4.1] J. Batey, E. Tierney, and T. N. Nguyen, "*Electrical Characteristics of Very Thin SiO_2 Deposited at Low Substrate Temperatures*," IEEE Electron Device Lett., **EDL-8**, 148(1987)

[4.2] G. G. Foutain, R. A. Rudder, S. V. Hattangady, R. J. Markunas, and P. S. Lindorme, "*Low Interface Density SiO_2 Deposited at 300 °C by Remote Plasma Enhanced CVD on Reconstructed Si Surface*," J. Appl. Phys., **63**, 4744(1988).

[4.3] G. Lucovsky, D. V. Tsu, and G. N. Parsons. In "Deposition and Growth Limits for Microelectronics". Edited by G. W. Rubloff, American Institute of Physiscs serries 4, CA 1987, pp 156-172

[4.4] D. J. DiMaria, R. Ghez, and D. Wong, "*Charge Trapping Studies in SiO_2 Using High Current Injection from Silicon Rich SiO_2 Films,*" J. Appl. Phys., **51**, 4830(1980).

[4.5] W. A. Pliskin, "*Comparison of Properties of Dielectric Films deposited by various methods*," J. Vac. Sci. Technol., **14**, 1064(1977).

[4.6] E. A. Taft, "*Films From Low Temperature Oxidation of Silane*," J. Electrochem. Soc., **126**, 1728(1979).

[4.7] K. H. Beckmann, "*Investigation of the Chemical Properties of Stain Films on Silicon by Mean of Infrared Spectroscopy*," Surf. Sci., **3**, 314(1965).

[4.8] V. S. Nguyen, W. A. Lanford, A. L. Rieger, "*Variation of Hydrogen Bonding, Depth Profiles, and Spin Density in Plasma Deposited Silicon-Nitride and Oxynitride Films with Deposition Mechanism*," J. Electrochem. Soc., **133**, 970(1986).

[4.9] W. A. Pliskin and H. S. Lehman, "*Structural Evaluation Of Silicon Oxide Films*," J. Electrochem. Soc., **112**, 1013(1965).

[4.10] G. Lucovsky, S. Y Lin, P. D. Richard, S. S. Chao, Y. Takagi, J. E. Keem, and J. E. Tyler, "*Local Atomic Structure Of Silicon Sub-Oxide (SiO_x, $x<2$)*," J. Non-Cryst. Solids, **75**, 429(1985).

[4.11] N. Nagasima, "*Structure Analysis Of SiO_2 Films Formed By Oxidation Of Silane*," J. Appl. Phys., **43**, 3378 (1972).

[4.12] A. C. Adam, F. B. Alexander, C. D. Capio, and T. E. Smith, "*Characterization of Plasma-Deposited Silicon Dioxide*," J. Electrochem. Soc., **128**, 1545(1981).

[4.13] M Nakamura, Y. Mochisuki, and K. Usami, "*Infrared Absorption Spectra and Compositions of Evaporated Silicon Oxides (SiO_x)*," Solid State Commun., **50**, 1079(1984).

[4.14] M. Hamasaki, T. Adachi, S. Wakayama, and Kikuchi, "*Crystallographic Study of Semi-Insulating Polycrystalline Silicon (SiPo) Doped with Oxygen Atoms*," J. Appl. Phys., **49**, 3987(1978).

[4.15] P. G. Pai, S. S. Chao, Y. Takagi, and G. Lucovsky, "*Infared Spectroscopic Study of SiO_x Films Produced by Plasma Enhanced Chemical Vapor Deposition*," J. Vac. Sci., Technol., **A4**, 689(1986).

[4.16] M. Nakamura, R. Kanzawa, and K. Sakai, "*Stress and Density Effects on Infrared Absorption Spectra of Silicate Glass Films*," J. Electrochem. Soc., **133**, 1167(1986).

[4.17] M. Stadtmuler, "*Mechanical Stress of CVD-Dielectrics*," J. Electrochem. Soc., **139**, 3669(1992).

[4.18] G. Lucovsky, J. T. Fitch, D. V. Tsu, and S. S. Kim, "*Atomic Structure in SiO_2 Thin Films Deposited by Remote Plasma-Enhanced Chemical Vapor Deposition*," J. Vac. Sci. Technol., **A7**, 1136(1989).

[4.19] J. E. Dial, R. E. Gong, and J. N. Fordemwalt, "*Thickness Measurements of Silicon Dioxide Films on Silicon by Infrared Absorption Techniques*," J. Electrochem. Soc., **115**, 326(1968).

[4.20] I. W. Bold and J. I. B. Wilson, "*Silicon-Silicon Dioxide Interface: An Infrared Study*," J. Appl. Phys., **53**, 4166(1974).

[4.21] M. Lenzlinger and E. H. Snow,"*Fowler-Nordheim Tunnelling into Thermally Grown SiO_2*," J. Appl. Phys., **40**, 278(1969).

[4.22] D. J. DiMaria and M. V. Fischetti, in "*The Physics and Chemistry of SiO_2 and the Si-SiO_2 Interface*," edited by C. R. Helms and B. E. Deal, Plenum Press, New York, 1988, p. 509.

[4.23] P. Balk, in "*Proceeding of Electrochemical Society*", Fall meeting (Electrochemical Society, Buffalo, New York, 1965), p. 29.

[4.24] D. J. DiMaria, "*Determination of Insulator Bulk-Trapped Charge Densities and Centroids from Photo Current-Voltage*

Characteristics of MOS Structures," J. Appl. Phys., **47**, 4073(1976).

[4.25] D. J. DiMaria, "*Correlation of Trap Creation With Electron Heating in Silicon Dioxide*," Appl. Phys. Lett., **51**, 655(1987).

[4.26] K. C. Kao, "*New Theory of Electrical Discharge and Breakdown in Low Mobility Condensed Insulator*," J. Appl. Phys., **55**, 752(1984).

[4.27] K. C. Kao, "*Theory of High-Field Electric Conduction and Breakdown in Dielectric Liquids*," IEEE Trans. on Electrical Insulation, **EI-11**, 121(1976).

[4.28] K. Nakashima and K. C. Kao, "*Conducting Filaments and Switching Phernomena in Chalcogenide Semiconductor*," J. Non-Cryst. Solids, **33**, 189(1977).

[4.29] E. Harari, "*Dielectric Breakdown in Electrically Stressed Thin Films of Thermal SiO_2*," J. Appl. Phys., **49**, 2478(1978).

[4.30] V. K. Agarwal, "*Breakdown Conduction in Langmuir Films of Low Thicknesses*," Thin Solid Films, **23**, s3(1974).

[4.31] D. M. Kroll, "*Theory of Electrical Instabilities of Mixed Electronic and Thermal Origin*," Phys. Rev., **B9**, 1669(1974).

[4.32] K. C. Kao, "*Double Injection in Solids with Non-Ohmic Contact: II Solid with Defects*," J. Phys. D. Appl. Phys., **17**, 1449(1984).

[4.33] G. G. Shirley, "*High Field Phernomena in Thermal SiO_2*," J. Electrochem. Soc., **132**, 488(1985).

[4.34] C. Falcony-Guajardo, F. J. Feigl, and S. R Butler, in "*Physiscs of MOS Insulators*", Edited by G. Lucovsky, S. T. Pantelides and F. L. Galeener, Pergamon, New York, 1980, p. 127.

5

The Effects of ECR microwave Plasma Radiation on the Charges and Defects in SiO_2-Si Systems

The effects of radiation due to gamma rays [5.1], X-rays [5.2], energetic electrons [5.3] and ion beams [5.4], on the behavior of MOS systems have been extensively studied although most of the studies are related to the MOS devices used in space or nuclear reactor environments. However, the effects of radiation due to these sources are similar, which cause mainly an increase in both the bulk trapped charges and the SiO_2/Si interface trapped charges. It is anticipated that the electron-hole pairs generated in the SiO_2 bulk during radiation are the main particles to cause the increase of such charges [5.5]. In the case of MOS systems, which are biased positively at the gate electrodes during radiation due to the floating potential, the electrons generated in the SiO_2 bulk can easily drift through the oxide toward the positive gate electrode, while the holes, because of their low mobility, may react with the vacant oxygen sites in the Si-Si bonds, creating E' centers and hence positively trapped charges in the SiO_2 bulk [5.6-5.8]. The creation of E' center and positively trapped charge is a reversible reaction process [5.9]; for example, electrons approaching E' centers may react with them neutralizing the positively trapped charges. Regarding the interface traps created by radiation, there are several schools of thought. One is the trapped hole model [5.10]. With this model, the radiation-generated holes are simply trapped at the SiO_2/Si interface

forming interface traps. One model is based on the assumption that the radiation-generated holes react with Si-OH bonds in the SiO_2 bulk releasing hydrogen ions(H^+), which then drift towards the interface [5.11]. These H^+ ions will then react with Si-H bonds and electrons from Si to form Si-dangling bonds (interface traps), and neutral atomic or molecular hydrogen. Another model is the bond strain gradient (BSG) model. Based on this model the oxygen dangling bond tends to propagate in the direction of increasing strain. Once this bond arrives at the interface, it encounters Si centers and becomes trapped there forming an interface trap.

The recent trend of using microwave plasma processing for the fabrication of MOS devices has raised a new concerns about the plasma radiation effects on the devices. Several investigators [5.12-5.13] have reported that MOS devices undergo degradation during the plasma etching process, particularly for devices with oxide thicknesses below 200 Å. However, the plasma radiation effects on the SiO_2 films and the SiO_2/Si interfaces during plasma-enhanced chemical vapor deposition (PECVD) have not yet been studied. It is known on the basis of several years' experience on microwave plasma processing that plasma radiation causes deterioration in the PECVD SiO_2 films and SiO_2/Si interfaces [5.14]. In-situ study of such effects in on-growing SiO_2 films is impossible. The viable way of studying such radiation effects is to simulate the radiation effects due to microwave plasmas during PECVD by using thermally grown SiO_2 films on Si substrates to form SiO_2/Si systems and to study the changes of the behavior of such systems after being exposed to microwave plasmas. It is hoped that this simulation study may shed some light on the radiation damage in MOS systems.

5.1. Experimental

The MOS capacitors used in this study were fabricated using the thermal oxidation process. Prior to loading, a drop of HCl was dropped on the empty boat which would be used later for holding the Si wafers. This boat was then placed immediately inside the hot zone of the quartz tube which had been heated to a temperature of 1100°C. After that, the quartz tube was flushed with O_2 gas for about 30 minutes. This is an important step based on experience because with this purging the concentrations of charges and defects are significantly reduced. In fact, a similar result about the effect of HCl has been reported by Hashimoto et al [5.15]. The substrates were n-type, <100> oriented, 2-4 ohm-cm silicon wafers. After the wafers were cleaned by the RCA method [5.16] with 17.5 x 10^6 ohm-cm de-ionized water, they were then dipped into a reduced HF:H_2O solution (1:100) to remove the native oxide before being placed in the boat. The boat was then placed in the hot zone of the quartz tube which was at 1100°C and the SiO_2 films were thermally grown on the Si wafer surfaces in dry oxygen to the desired thicknesses, the film growth rate being 25 Å min^{-1}. After the film growth, the quartz tube was pulled out of the hot zone and allowed to cool slowly outside the furnace. The time required for the sample to cool down to room temperature was about 30 minutes. No further post annealing was performed. After the SiO_2 films on the back side of the wafers were removed by HF etch, an aluminum electrode was blanket-deposited on the surface of the silicon side for each wafer by thermal evaporation. The samples were then divided into two groups. One group was named the "OS" group which remained unaltered with only Al back electrodes, while the other group was named the "MOS" group in which Al electrodes of $5x10^{-2}$ cm^2 in area each were vacuum deposited on

top of the SiO_2 surfaces through a shadow mask to form MOS capacitors by thermal evaporation. The MOS group was further divided into three sub-groups, namely; (a) MOS capacitors as fabricated without any further treatment, (b) MOS capacitors subjected to post-metalization annealing (PMA) at 400 °C in forming gas (10 % of H_2 in N_2) for 30 min, and (c) MOS capacitors covered with a shadow Cu mask of 0.5 mm in thickness having the opening windows for Al gate electrodes to protect the SiO_2 region. These three sub-groups were named "MOS", "PMAMOS", and "MASKMOS" for (a), (b), (c), respectively as shown in Fig. 5.1. For each run a set of samples including OS, MOS, PMAMOS, and MASKMOS was subjected to radiation produced by a microwave plasma of N_2O in the plasma chamber. The microwave ECR plasma system used to produce plasmas has been described elsewhere [5.14]. All experiments were performed at the same plasma parameters which were: microwave frequency: 2.45 GHz, microwave power absorption: 6 W, N_2O gas flow rate: 10 sccm, gas pressure: $2x10^{-2}$ torr, and total exposure time: 30 minutes. Four temperatures for samples during plasma radiation were used, namely, 30°C, 100°C, 200°C, and 300°C. Plasma of N_2O gas was chosen for this study because it was the gas that was used in the fabrication of microwave ECR PECVD SiO_2 films [5.14]. To characterize the samples before and after radiation, high frequency (1 MHz) and quasi-static capacitance-voltage (C-V) measurements were used. The overall flow chart of the experimental set up and measurement steps is shown in Fig. 5.2. All measurements were performed at room temperature (22 °C). For the determination of the oxide trapped charge, the charge centroid is assumed to be located near the SiO_2/Si interface for the case prior to the plasma radiation, and located near the middle of the SiO_2 film for the case

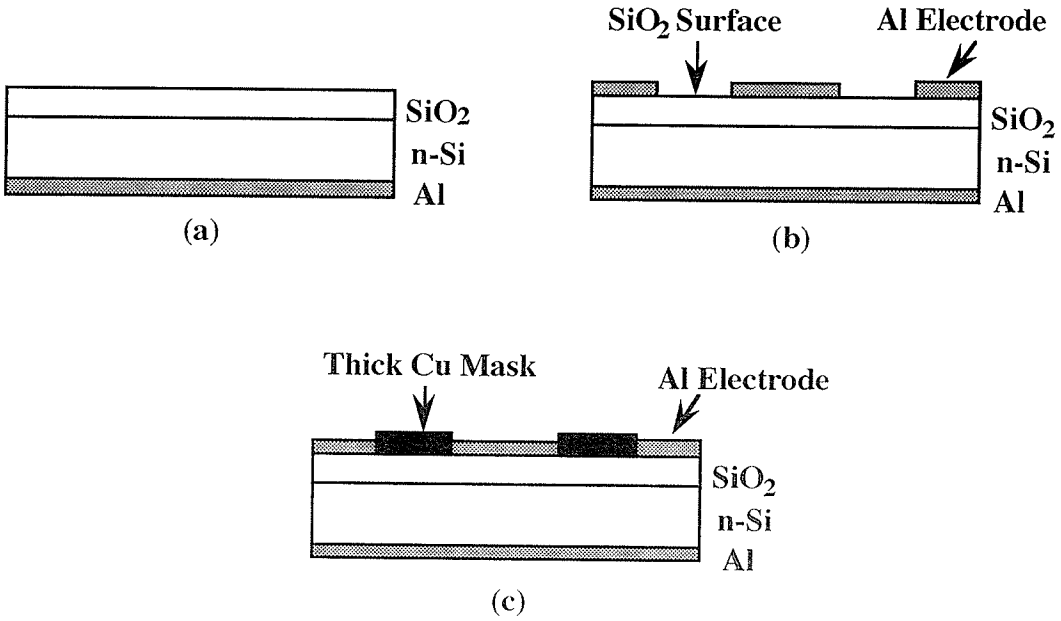

Figure 5.1. Device configurations for plasma radiation experiments. (a) OS sample with only Al electrode on the Si surface, (b) MOS or PMAMOS sample with Al electrodes on both the Si and SiO_2 surfaces, and (c) MASKMOS sample-same as (b) but with a thick Cu mask to prevent the radiation from penetrating into the SiO_2 regions.

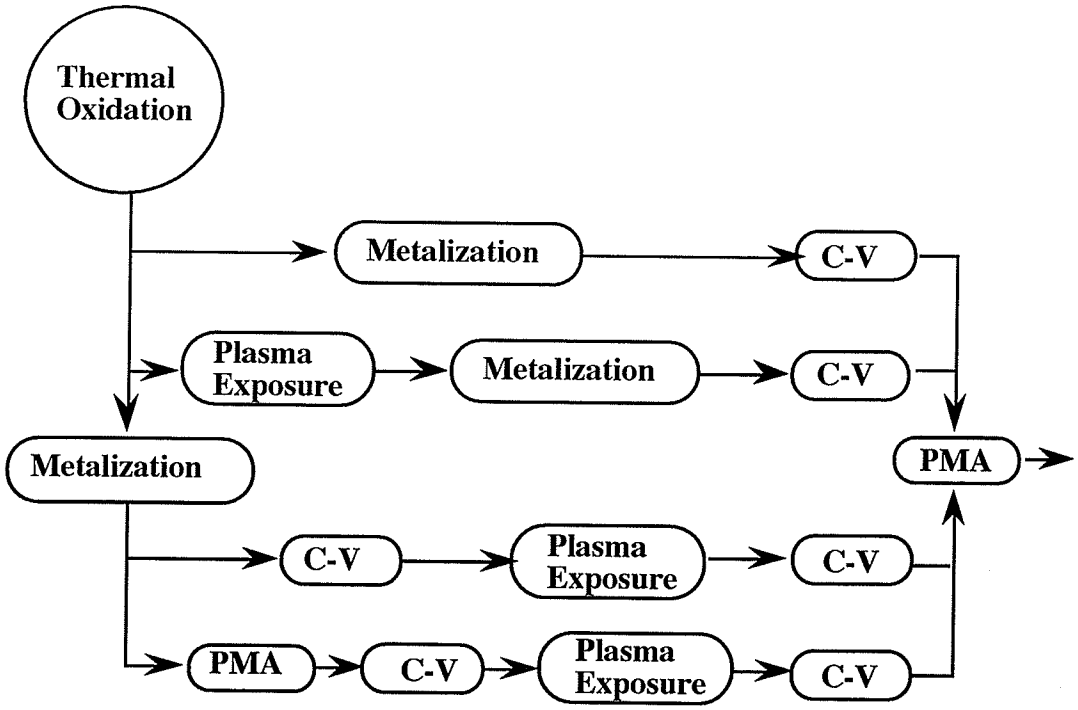

Figure 5.2. Flow chart of the experimental set-up and measurement steps.

after plasma radiation. The work function difference between the aluminum electrode and silicon is assumed to be -0.28 eV.

5.2. Model of plasma radiation effects on the MOS systems

When MOS system is subjected to plasma radiation, particles such as electrons, ions and photons created in the plasma will react with the system. For the MOS system with the SiO_2 film fabricated by PECVD, the on-growing SiO_2 film as well the SiO_2/Si interface may continue being subjected to plasma radiation during the film growth process. In this model, an ideal oxide-silicon unit prior to the plasma radiation has been used and is shown in Fig. 5.3(A). It is assumed that this unit has no oxide fixed charge and interface trapped charge. When such an ideal OS unit is exposed to plasma radiation, electrons, because of their high mobility, will first arrive at the SiO_2 surface and rest there creating a floating potential across the SiO_2 film, which may reach 17 - 20 V although the average kinetic energy of the electron is about 3.8 eV [5.17]. These electrons resting on the SiO_2 surface will create a depletion region in the n-type Si as shown in Fig. 5.3(B). The width of the depletion region W_b depends on the number of electrons on the SiO_2 surface. As time goes on, high energy electrons and photons from the plasma will penetrate into the SiO_2. Some of the penetrated electrons are trapped in the SiO_2 bulk creating negative oxide trapped charge and some may reach the SiO_2-Si interface creating traps and being trapped there. The UV photons are generally absorbed near the SiO_2 surface [5.18-5.19] and they will produce electron-hole pairs as well as break the strained Si-O bonds. The broken strained bond may then trap an electron by the silicon dangling bond, or capture a hole by the oxygen dangling bond. According to the bond-strain gradient model [5.19,

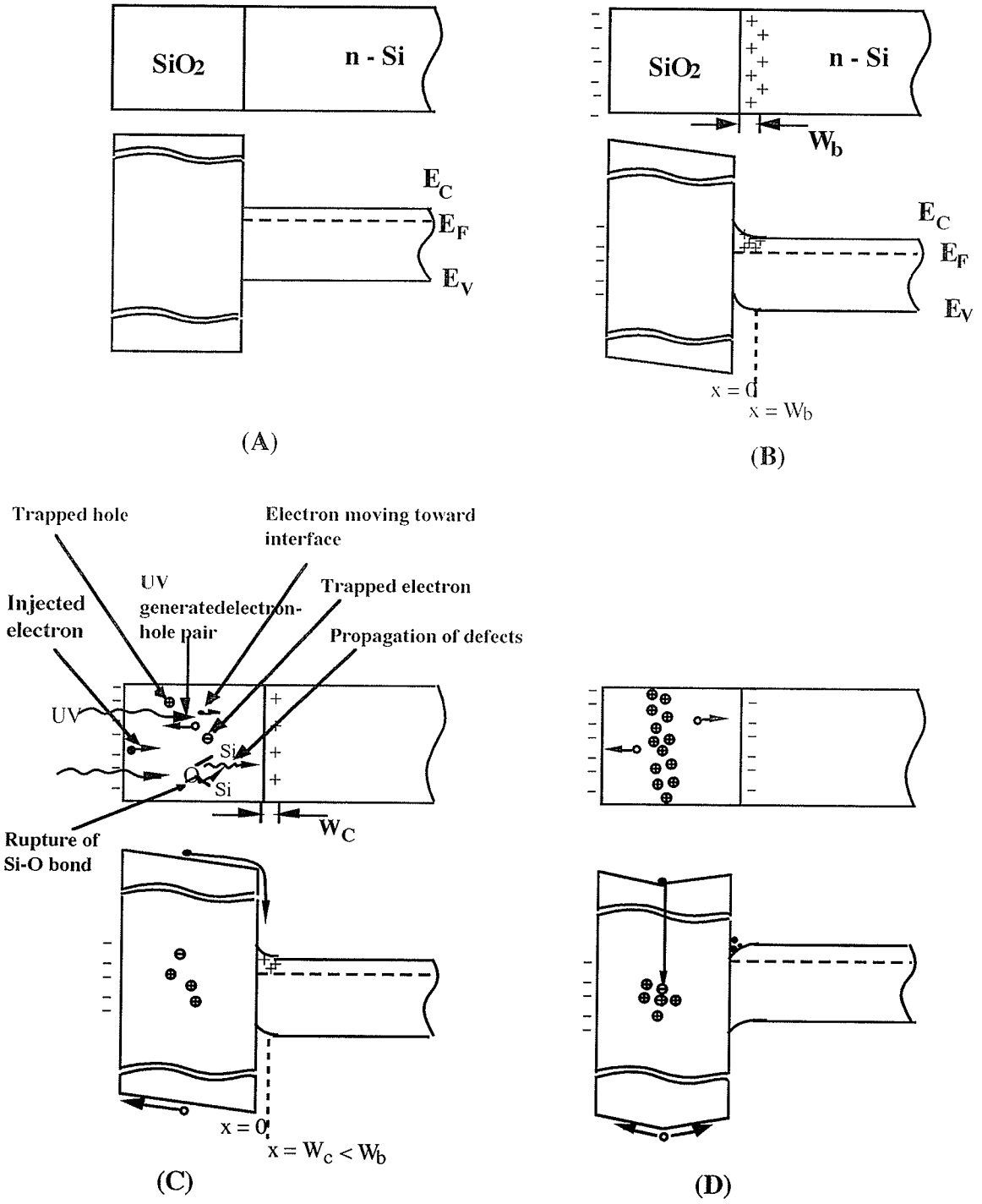

Figure 5.3. An ideal OS unit and its simplified energy diagram for (A) prior to radiation (B) initial period of the radiation effects, (C) during radiation period, and (D) after prolonged radiation.

5.20] the silicon dangling bond stays at its original site, while the oxygen dangling bond tends to propagate in the direction of increasing strain. Since the strain is highest at the SiO_2-Si interface, this implies that the oxygen dangling bond tends to propagate toward the interface to interact with Si there to form an interface trap. At the same time, under the influence of the internal electric field, electrons generated by the radiation will move toward the anode (n-Si) while holes tend to move toward the cathode (SiO_2 surface). Because of their low mobility, some holes will be trapped inside the SiO_2 bulk to form positive trapped charges. These positive trapped charges then screen out the effects of the electrons on the SiO_2 surface, thus reducing the field toward the SiO_2-Si interface. This causes the depletion region width to decrease as shown in Fig. 5.3(C).

When the number of positive trapped charge in the SiO_2 bulk becomes sufficiently high, they could drive the OS unit from its depletion mode to an accumulation mode as shown in Fig. 5.3(D). Under this accumulation mode condition, holes generated by the radiation may move towards the SiO_2/Si interface and be trapped there to form interface trapped charges. Based on this model, it is expected that the thicker the SiO_2 film, the more will be the positive trapped charge in the SiO_2 bulk and the higher will be the interface trap density. In the following, some experimental results which are in good agreement with this model are presented.

5.3. Results and discussion

Prior to plasma radiation exposure, the MOS devices were first characterized by capacitance-voltage (C-V)measurements. The average value of the interface trap density (D_{it}) for MOS devices after an initial PMA treatment varied from $5x10^9$ to $2x10^{10}$ eV^{-1} cm^{-2} as the oxide

thickness increased from 228 Å to 941 Å. A similar thickness dependence has been reported by Nicollian and Brews [5.21]. The average value of the oxide trapped charge (Q_{ot}) for MOS devices after an initial PMA treatment varies from $1.5x10^{11}$ qcm^{-2} (negative) to $1.5x10^{10}$ q cm^{-2} (negative) as the oxide thickness increases from 228 Å to 941 Å. These negative charges are introduced by metalization and initial PMA treatment. During the PMA treatment at 400 °C, electrons from the n-Si substrate are introduced into the oxide bulk [5.22]. Thus, not only are the positive charges originally present in the oxide bulk due to excess oxygen species near the interface during the oxidation process [5.23] neutralized by the negative electron charges, but an excessive amount of negative charges is also accumulated. Prior to plasma radiation exposure, MOS devices were heated at temperatures up to 300 °C (below the PMA temperature which is 400 °C) for about 30 min, and then the C-V measurements were carried out at room temperature in order to check whether such low temperatures (≤300 °C) would affect the values of D_{it} and Q_{ot}. The results show that D_{it} and Q_{ot} are practically unaffected by the heat treatment at temperatures below 300 °C. In the following, the effects of device temperature during plasma radiation exposure on the radiation-induced defects and charges in annealed MOS devices (PMAMOS) will be reported. In this case, although the device temperatures used for the experiment are below 300 °C, it was found that the radiation effects are strongly dependent on device temperature during radiation. It is therefore important to ensure that prior to the radiation exposure, the values of D_{it} and Q_{ot} are consistent for all MOS devices, and these values will be called the Pre-irradiation values as the references for comparison purposes. Table 5.1 gives the values of D_{it}

Table 5.1. The pre-irradiation values of D_{it} and Q_{ot} prior to plasma radiation exposure.

	Before PMA		After initial PMA	
Oxide Thickness (A)	288	941	228	941
D_{it} eV^{-1} cm^{-2}	3.5×10^{11}	2.0×10^{11}	5.0×10^{9}	2.0×10^{10}
Q_{ot} (qcm^{-2})	$+.18 \times 10^{11}$	$+ 6.0 \times 10^{10}$	$- 1.5 \times 10^{11}$	$- 1.5 \times 10^{11}$

and Q_{ot} which are consistent for all devices in this investigation.

5.3.1. Radiation effects on the interface trap density

The effects of plasma radiation on the value of D_{it} for the four device configurations with various SiO_2 film thicknesses and also the effects of Post-irradiation final PMA (Annealing after radiation treatment) have been studied. The results are shown in Fig. 5.4. It can be seen that D_{it} always increases with increasing oxide thickness (d_{ox}) for all four device configurations. The D_{it}-d_{ox} curves for devices after radiation follow a simple power law (D_{it} a d_{ox}^{n}) with n varying from 0.3 to 0.6. A similar power law dependence but with n of 0.5-2 has been reported for high energy radiation such as Co^{60} and gamma rays [5.24, 5.26] with energies extending to the MeV range. The lower value of n for microwave plasma radiation may be due to its low energies (<50 eV). By comparing the results with the pre-irradiation values of D_{it}, it can be seen that the plasma radiation has created a large quantity of defects at the interface. These results are consistent with those for the MOS devices with the oxide

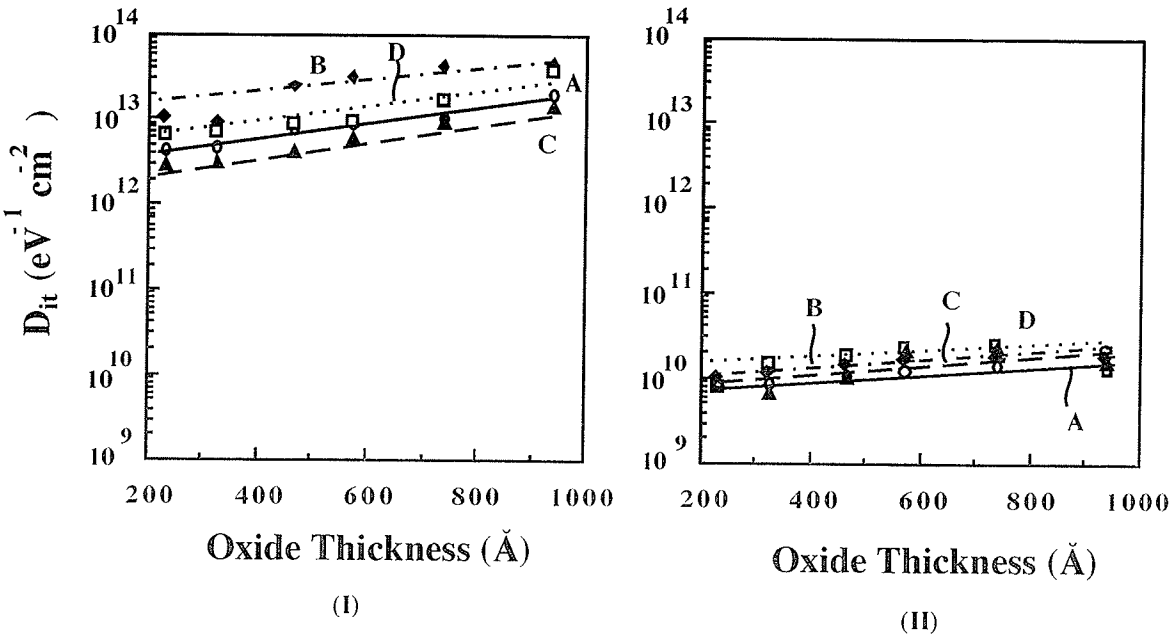

Figure 5.4. Mid gap D_{it} as a function of oxide thickness for device temperature of 22°C during radiation (I) after exposure to plasma radiation and (II) after post-irradiation final PMA treatment for (A) OS samples, (B) MOS samples, (C) PMAMOS samples, and (D) MASKMOS samples.

fabricated by PECVD, which always have a large value of D_{it} because such MOS devices have already been subjected to N_2O plasma radiation during the deposition of SiO_2 films.

As has been mentioned in the last section, the radiation effects are mainly due to UV penetration into the SiO_2 bulk and the interface, which generates electron-hole pairs and breaks strained Si-O bonds. The thicker the oxide, the greater the number of electron-hole pairs and broken strained bonds generated. Furthermore, a thicker oxide has a relatively larger strain gradient toward the interface [5.3, 5.20, 5.27, 5.28]. This leads to the experimental fact that MOS devices with a thicker oxide have more radiation induced interface traps. Of the four device configurations,

the PMAMOS sample has been subjected to an initial PMA treatment. Therefore, this sample has fewer strained bonds and hence a fewer number of bonds susceptible to breakage upon ionizing radiation, and therefore fewer defects migrating to the interface to form interface traps. This is why the PMAMOS sample has the lowest D_{it} after radiation. The OS, MOS, and MASKMOS samples were not subjected to an initial PMA treatment, and these samples are expected to have a higher concentration of strained bonds. The OS sample has a slightly higher D_{it} than the PMAMOS sample. It is likely that without the top electrodes on the SiO_2 surface, energetic particles, such as electrons with energy $E_e > 7$ eV, would easily penetrate into the SiO_2 bulk. These penetrated electrons could be trapped to form a negative trapped charge tending to act as a screen to suppress further electron penetration. The penetrated electrons may react with E' centers converting them to neutral species. This may be the reason why the OS samples have a D_{it} lower than the MOS and the MASKMOS samples. The MASKMOS samples have not only the Al electrodes covering part of the SiO_2 surfaces but also have a thick Cu mask covering the remaining of the SiO_2 surface to eliminate the penetration of energetic particles. It can be expected, therefore, that the MOS samples have the highest and the PMAMOS samples the least radiation-created D_{it}.

For all device configurations shown in Fig. 5.1, the value of D_{it} created by plasma radiation always decreases with increasing device temperature during radiation for temperatures up to about 200 °C regardless of the oxide thickness as shown in Figs. 5.5 and 5.6. This phenomenon implies that the radiation effects involve two competing processes, one is the defect generation process and the other is the

annihilation process. The main cause for the damage is the plasma-generated vacuum UV light as has been discussed in the previous section. The UV light can penetrate through the aluminum electrode into the SiO_2 bulk and the SiO_2-Si interface, thus creating interface traps. As the device temperature increases, the thermal annealing process becomes important. It tends to annihilate the defects generated by the radiation. According to the recombination enhanced defect reaction (REDR) model [5.29], the recombination of excess electrons and excess holes via defect centers releases a substantial amount of energy which can cause excitation of the vibrational states of the defects. This would in turn enhance the defect reactions such as diffusion, dissociation and annihilation of defects. The higher the device temperature during radiation, the more effective are the reactions causing the annihilation to override the generation of defects. This is why D_{it} decreases with increasing device temperature during radiation for device temperatures up to 200 °C.

As the device temperature increases beyond 200 °C, D_{it} starts to increase with increasing device temperature as shown in Figs. 5.5 and 5.6. This reverse trend may be attributed to the possibility that for temperatures larger than 200 °C, the defect generation process becomes more dominant than the defect annihilation process. It is likely that the higher the temperature the easier is the breaking of the Si-O bonds and the movement of radiation-generated electrons and holes. This tends to enhance defect generation and to nullify the defect annihilation process, and possibly the traps created are deeper traps at higher device temperatures.

For the four device configurations there is no significant difference in the rate of the decrease in the value of D_{it} with respect to the change of the

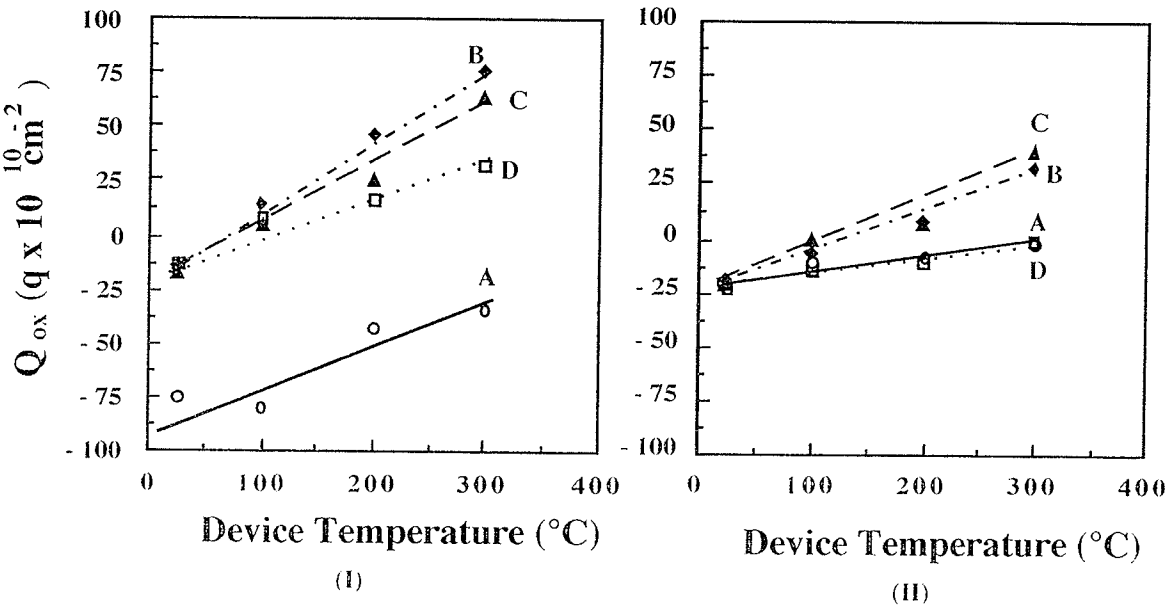

Figure 5.5. Midgap D_{it} as a function of device temperature during radiation (I) after exposure to plasma radiation and (II) after post-irradiation final PMA treatment for (A) OS samples, (B) MOS samples, (C) PMAMOS samples, and (D) MASKMOS samples for oxide thickness of 228 Å.

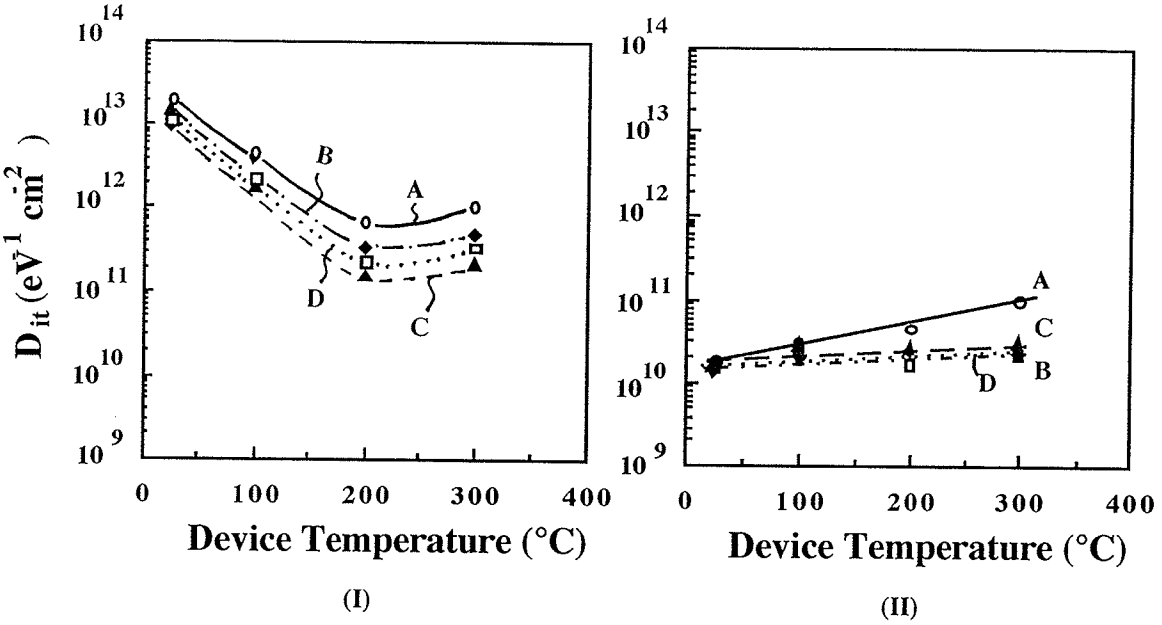

Figure 5.6. Midgap D_{it} as a function of device temperature during radiation (I) after exposure to plasma radiation and (II) after post-irradiation final PMA treatment for (A) OS samples, (B) MOS samples, (C) PMAMOS samples, and (D) MASKMOS samples for oxide thickness of 941 Å.

device temperature during radiation in the temperature range of 20-200 °C, but this rate becomes more drastic for devices with a thicker oxide as shown in Fig. 5.6. This can be attributed mainly to a larger strain gradient for the devices with a thicker oxide. It should be noted that mobile hydrogen species present in the oxide would be enhanced by the thermal activation and become more effective in passivating the broken bond defects to form SiH or SiOH bonds. This will reduce the potential trap sites to form the interface trapped charge at the interface. Furthermore, the large strain gradient is also responsible for hydrogen transport by accelerating the hydrogenation process. This may explain also why D_{it} decreases so drastically with increasing device temperatures for samples with a thick oxide.

From Figs. 5.5 and 5.6 it can be seen that the post-irradiation final PMA treatment can anneal out most of the radiation-induced interface traps. The value of D_{it} is still slightly higher than its pre-irradiation value (prior to radiation), particularly for the OS samples. The difference between the value of D_{it} after post-irradiation PMA treatment and that prior to radiation increases as the device temperature during radiation is increased, indicating that more deep traps are produced at elevated temperatures, particularly at temperatures higher than 200 °C.

5.3.2. Radiation Effects on the Oxide Trapped Charge

The effects of plasma radiation on the value of Q_{ot} for the four device configurations with various SiO_2 film thicknesses and also the effects of post-irradiation final PMA treatment have been studied. The results are shown in Fig. 5.7. Of the four device configurations, the value of Q_{ot} after radiation changes its polarity from a net negative charge to a net positive

charge as the oxide thickness is increased for MOS and MASKMOS samples, while Q_{ot} is negative and the net negative charge decreases with increasing oxide thickness for OS and PMAMOS samples. In fact, the trend for all the four device configurations is consistent, that is, the net radiation-induced positive oxide charge increases with increasing oxide thickness. The internal field inside the oxide due to the plasma floating potential which can be considered to be practically independent of oxide thickness, increases with decreasing oxide thickness. For devices with a thin oxide (e.g. 228 Å), the electrical field inside the oxide under radiation can reach a value as high as 7-10 $MVcm^{-1}$, which can cause electron injection from the Al gate electrode to the oxide and subsequently trapped by silicon dangling bonds created by bond rupture during radiation in the oxide. This is why Q_{ot} is negative when the oxide is thin. Furthermore, devices with a thin oxide have a small strain gradient and hence the broken bonds have more chance to stay in the oxide bulk rather than to migrate to the SiO_2-Si interface leading to a high concentration of electron traps in the SiO_2 bulk.

As the oxide thickness increases, the internal electric field during radiation decreases. Thus, electron injection from the Al electrode may drop significantly, but the radiation-generated electron-hole pairs increases. In this case the number of holes trapped may become more dominant and hence the net charge Q_t becomes positive for PMAMOS samples. Initial PMA treatment has removed most of positive net trapped charge, so that during radiation, electrons injected from the Al electrode under high internal fields become dominant. This is why Q_t is large and negative. For OS samples the high-energy electrons from the plasma can

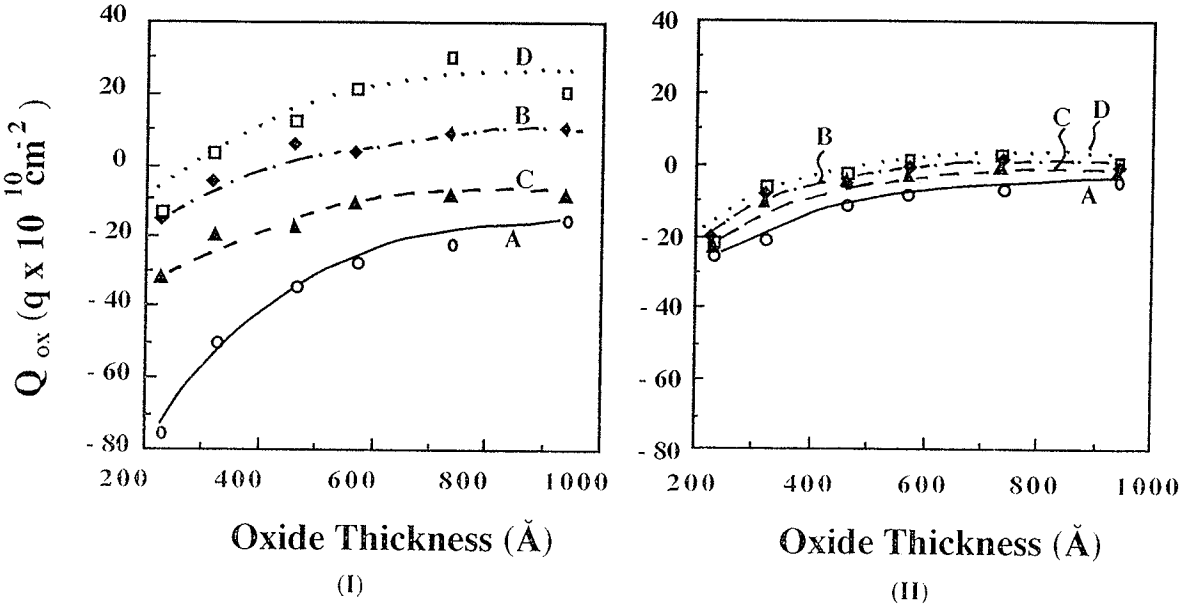

Figure 5.7. Q_{ot} as a function of oxide thickness for device temperature of 22 °C during radiation (I) after exposure to plasma radiation and (II) after post-irradiation final PMA treatment for (A) OS samples, (B) MOS samples, (C) PMAMOS samples, and (D) MASKMOS samples.

directly penetrate into the SiO_2 bulk and then be trapped there. This is why for OS samples, Q_{ot} is large and negative. Both the MOS and the MASKMOS samples, which have not been subjected to the initial PMA treatment, have a net positive trapped charge after radiation. However, the value of Q_{ot} can be annealed out after a post irradiation final PMA treatment as shown in Fig. 5.7(II).

Figures 5.8 and 5.9 show that for the MOS, PMAMOS and MASKMOS samples, the positive oxide trapped charge Q_{ot} increases with increasing device temperature during radiation, regardless of the oxide thickness. According to Hughes [5.30, 5.31] both the electron and hole mobilities are temperature dependent, and the hole mobility deceases much faster than the electron mobility with increasing temperature. Thus as the device temperature increases, the radiation-generated holes will be more

readily be trapped in the SiO_2 bulk after the mobile electrons are driven out, resulting in an increase of positive Q_{ot}. For the OS sample, the net negative oxide trapped charge Q_{ot} is high because hot electrons from the plasma can easily penetrate into the SiO_2 bulk and be trapped there. As the device temperature increases, the radiation-generated electrons may be easily driven out of the oxide and the holes left behind may be trapped to form a positive trapped charge, but the number of such trapped holes may not be large enough to override the number of electrons already trapped there. This is why the net negative oxide trapped charge decreases with increasing device temperature but the change is still not large enough to convert the net oxide trapped charge from negative to positive.

Post-irradiation final PMA treatment can anneal out most of radiation-generated oxide-trapped charge as shown in Figs 5.8 and 5.9. Again, the value of Q_{ot} after the post irradiation final PMA is still higher than the pre-irradiation value (prior to radiation), and the difference between these two values increases as the device temperature is increased implying that the PMA treatment can not remove the deeply oxide trapped charge.

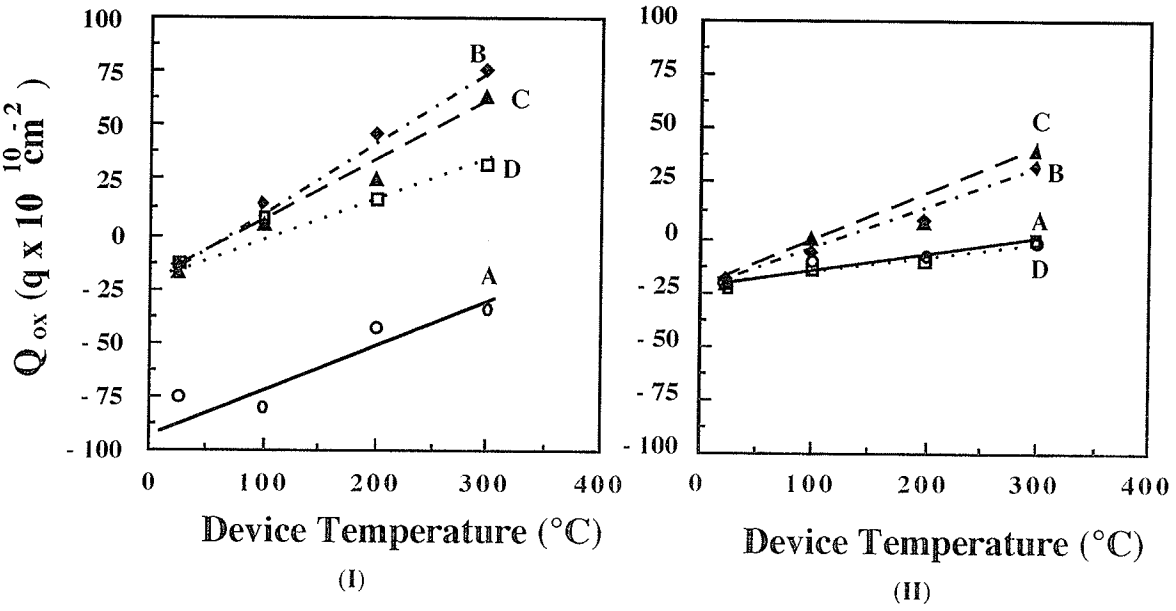

Figure 5.8. Q_{ot} as a function of device temperature during radiation (I) after exposure to plasma radiation and (II) after post-irradiation final PMA treatment for (A) OS samples, (B) MOS samples, (C) PMAMOS samples, and (D) MASKMOS samples for oxide thickness of 228 Å.

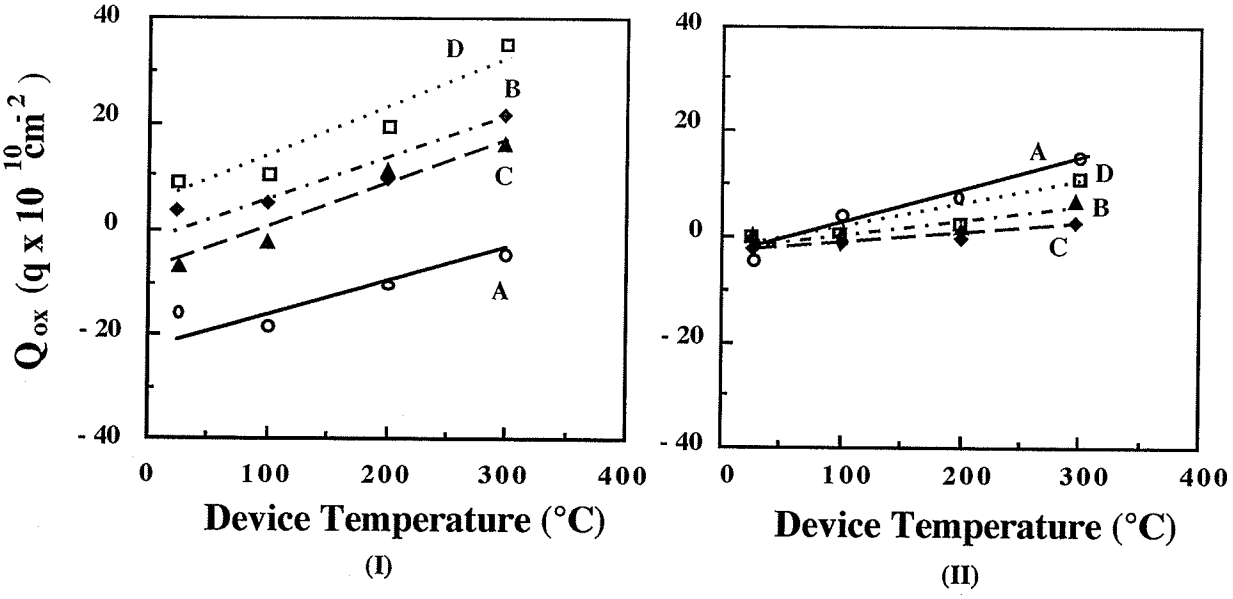

Figure 5.9. Q_{ot} as a function of device temperature during radiation (I) after exposure to plasma radiation and (II) after post-irradiation final PMA treatment for (A) OS samples, (B) MOS samples, (C) PMAMOS samples, and (D) MASKMOS samples for oxide thickness of 941 Å.

References for chapter 5

[5.1] J. E. Shelby, "*Radiation Effects in Hydrogen Impregnated Vitreous Silica*," J. Appl. Phys., **50**, 3702(1979).

[5.2] T. R. Oldham and J. M. Mc Garrity, "*Comparison of $^{60}C_o$ Response and 10 KeV X-Ray Response in MOS Capacitors*," IEEE Trans. Nucl. Sci., **30**, 4377(1983).

[5.3] F. J. Grunthaner, B. F. Lewis, N. Zamini, and J. Maserjian, "*XPS Studies of Structure Induced Radiaton Effects at the Si/SiO_2 Interface*," IEEE Trans. Nucl. Sci., **27**, 1640(1980).

[5.4] K. Yokogawa, Y. Yajima, T. Mizutani, S. Nishimatsu, and K. Ninomiya, "*Mechanism of E' Center Generation in SiO_2 Film by Ion and Neutral Beam Bombardment*," Jpn. J. Appl. Phys., **30**, 3199(1991).

[5.5] R. A. B. Devine, "*Comparative Radiation Sensitivity Study of Bulk, Wet and Dry Aporphous SiO_2*," J. Non-Cryst. Solids, **107**, 41(1988).

[5.6] D. L. Griscom, "*E' Center in Glassy SiO_2 ^{17}O, ^{1}H and Very Weak ^{29}Si Superhyperfine Structure*," Phys. Rev., **22B**, 4190(1980).

[5.7] R. H. Silsbee, "*Electron Spin Resonance in Neutron-Irradiated Quartz*," J. Appl. Phys., **32**, 1459(1961).

[5.8] P. M. Lenahan and P. V. Dressendorfer, "*Paramagnetic Trivalent Silicon Centers in Gamma Irradiated Metal-Oxide-Silicon Structures*," Appl. Phys. Lett., **44**, 96(1984).

[5.9] H. S. Witham and P. M. Lenahan, "*The Nature of the Deep Hole Trap in MOS Devices*," IEEE trans. Nucl. Sci., **34**, 1147(1987).

[5.10] P. S. Winokur, H. E. Boesch, Jr., J. M. McGarrity, and F. B. Mclean, "*Two-Stage Process for Buildup of Radiation-Induced Interface States*," J. Appl. Phys., **50**, 3492(1979).

[5.11] G. J. Hu and W. C. Johnson, "*Relationship between X-Ray-Produced Holes and Interface States in Metal-Oxide-Semiconductor Capacitors*," J. Appl. Phys., **54**, 1441(1983).

[5.12] C. T. Gabriel and J. P. McVittie, "*How Plasma Etching Damages Thin Gate Oxides*," Solid State Technol., **35(6)**, 81(1992).

[5.13] S. Samukawa, "*Dependence of Gate Oxide Breakdown Frequency on Ion Current Density Distribution During ECR Plasma Etching*," Jpn. J. Appl. Phys., **30**, L1902(1991).

[5.14] T. T. Chau, S. R. Mejia, and K. C. Kao., "*New Approach to Low Temperature Deposition of High Quality Thin Films by Electron Cyclotron Resonance Microwave Plasmas*," J. Vac. Sci. Technol., **B10**, 2170(1992).

[5.15] C. Hashimoto, S. Muramoto, N. Shiono, and O. Nakajima, "*Method of Forming Thin Gate and Highly Reliable Gate Oxide*," J. Chem. Soc., **127**, 129(1980).

[5.16] W. Kern and D. A. Puotinen, "*Cleaning Solutions Based on Hydrogen Peroxide for Use in Silicon Semiconductor Technology*," RCA Rev., **31**, 187 (1970).

[5.17] T. Sugano, "*Application of Plasma Process to VLSI Technology*," John Willey & Sons Inc, 1985, Chapter 2, p 148.

[5.18] K. Yokogawa, Y. Yajima, T. Mizutani, S. Nishimatsu, and K. Suzuki, "*Positive Charge and E' Centers Formed by Vacuum Ultraviolet Radiation in SiO_2 Grown on Si*," Jpn. J. Appl. Phys., **29**, 2265(1990).

[5.19] R.J. Powell and G. F. Derbenwick, "*Vacuum Ultrviolet Radiation Effects in SiO_2*," IEEE Trans Nucl. Sci., **18(6)**, 99(1971).

[5.20] F. J. Grunthaner, P. J. Grunthaner, and J. Maserjian, "*Radiation Induce Defects in SiO_2 at Determined with XPS*," IEEE Trans. Nucl. Sci., **29**, 1462(1982).

[5.21] E. H. Nicollian and J. R. Brews, "*MOS Physics and Technology*", John Willey and Sons, New York, (1982).

[5.22] E. H. Snow, A. S. Grove, "*Effects of Ionizing Radiation on Oxidized Silcon Surfaces and Planar Devices*," Proc. IEEE, **55**, 1168(1967)

[5.23] B. E. Deal and A. S. grove, "*General Relationship for the Thermal Oxidation of Silicon*," J. Appl. Phys., **36**, 3770 (1965).

[5.24] C. R. Viswanathan and J. Maserjian, "*Model for Thickness Dependence of Radiation Charging in MOS structures*," IEEE Trans. Nucl. Sci., **23**, 1540(1976).

[5.25] P. S. Winokur, in "*Radiation-Induced Interface Traps in Ionizing radiation Effects in MOS Devices and Circuits,*" Edited by T. P. Ma and P. V. Dressendorfer, John Willey & Sons, New York, 1989, Chapter 3.

[5.26] A. G. Sabnis, "*Characterization of Annealing of Co^{60} Gamma-Ray Damage at the Si/SiO_2 Interface*," IEEE Trans. Nucl. Sci. , **30**, 4094(1983).

[5.27] A. B. Joshiand and D. L. Kwong, "*Dependence of Radiation Induced Damage on Gate Oxide Thickness in MOS Capacitors with Ultra Thin ate Oxide*," Electron. Lett., **28**, 744(1992).

[5.28] T. P. Ma, in "*Process-Induced Radiation Effects in Ionizing Radiation Effects in Mos Devices and Circuits*", Edited by T. P.

Ma and P. V. Dressendorfer, John Willey & Sons, New York, 1989, Chapter 7.

[5.29] L. C. Kimerling, "*Recombination Enhanced Defect Reactions*," Solid State Electro., **21**, 1391(1978).

[5.30] R. C. Hughes, "*Carrier Tansport Phernomena in Amorphous* SiO_2," Phy. Rev. Let., **30**, 1333(1973).

[5.31] R. C. Hughes, "*Hole Mobility and Transport in Thin* SiO_2 *Films*," Phys. Lett., **26**, 436(1975)

6

Conclusions

On the basis of the work described above, the following conclusions are drawn:

(A) The ECR microwave CPPP system used in conjunction with the SSEC for deposition of thin films at low temperatures has the following features::

(1) It suppresses effectively the damaging effects on the substrates and the on-growing films due to the bombardment of energetic particles produced in the plasma during film deposition.

(2) It suppresses effectively the upstream diffusion of the reactant gas injected into the processing chamber to the plasma chamber, thus avoiding the heterogeneous gas phase reaction in the plasma which may produce micro-dust particles.

(3) It allows sufficient neutral activated species to diffuse in downstream into the processing chamber for chemical reaction with the reactant gas at the substrate surface, because with the SSEC the substrate can be placed very close to the plasma region.

(4) Experimental results have shown clearly that the SiO_2 films deposited using the ECR microwave plasma in conjunction with the SSEC exhibit the physical and electronic properties approaching those of high-quality thermal grown silicon dioxide.

(B) The effects of deposition parameters on the properties of MOS systems are as follows:

(1) The deposition rate is more sensitive to the increase in gas pressure than to the increase in gas-flow ratio. A high deposition rate is always accompanied by a high electron trap concentration and poor stoichiometry of the SiO_2 films.

(2) Good quality SiO_2 films can be deposited at a relative high deposition rate by keeping the gas-flow ratio of 10 (N_2O:SiH_4) and the gas pressure within 20-50 mtorr.

(3) The reactions in the ECR microwave PECVD process are heterogeneous and chemical reaction rate limited at the substrate surface with an activation energy of 0.035 eV.

(4) For deposition temperatures lower than 200 °C, the films are silicon rich and all other properties are further deteriorated as the deposition temperature is further decreased.

(5) At deposition temperatures higher than 250 °C, the deposition rate become practically independent of the deposition temperature and the films are stoichiometric.

(6) The SiO_2 films fabricated at 300 °C are uniform in composition and structure throughout the films for at least the thickness range of 100-1000 Å.

(C) The dependence of the behavior of the SiO_2/Si system on the thickness of SiO_2 films are as follows:

(1) The threshold field for the onset of the Fowler-Norheim (FN) tunneling injection is about 5.0 - 5.5 MV/cm, independent of film thickness, while the threshold field for the onset of space charge

limitation (the onset of the deviation from the FN relation) increases with increasing film thickness.

(2) The average breakdown strength decreases with increasing film thickness, and also decreases with decreasing the applied voltage ramp rate. This phenomenon may be attributable to the thermal instability and the space charge effect which lead to final destructive breakdown.

(3) There is no impact ionization prior to breakdown. The breakdown process is initiated by thermal instability and followed by impact ionization leading to a sharp increase in current at the breakdown field.

(D) The effects of plasma radiation on the SiO_2 films are as follows:

(1) The plasma radiation damage in MOS devices depends on the thickness of the SiO_2 films. In general, the interface trap density, D_{it}, increases with increasing SiO_2 film thickness after plasma radiation following a power law ($D_{it} \alpha d_{ox}^n$) with n ranging from 0.3 to 0.6 for our MOS devices. The positive oxide trapped charge, Q_{ot}, also increases with increasing SiO_2 film thickness after plasma radiation.

(2) The value of D_{it} decreases with increasing device temperature during plasma radiation for temperatures up to 200 °C. Beyond 200 °C, the trend is reversed; that is, the value of D_{it} increases with increasing device temperature. The value of positive Q_{ot} also increases with increasing device temperature during radiation.

(3) The radiation effects are mainly due to the vacuum ultraviolet (UV) lights which penetrate into the SiO_2 bulk and the SiO_2-Si

interface creating electron-hole pairs and broken bonds in the SiO_2 bulk and at the interface. These effects as well as the bond-strain gradient toward the interface coupled with the floating potential across the SiO_2 film lead to the formation of charges and defects in the SiO_2 bulk and at the interface.

(4) The strong effect of device temperature during radiation on the radiation induced damage indicates that there are two processes taking place during radiation, one is the defect creation and the other is the defect annihilation. Thus, the degree of radiation damage can be reduced during the plasma processing for both PECVD or etching if it is conducted in a temperature range of 200-300 °C.

(5) Most of the radiation-induced defects and charges can be annealed out by a standard PMA treatment. However, some damage induced by plasma radiation at temperatures higher than 200 °C remains unaltered even after a standard PMA treatment.